2018

Phase transformations and chemical interactions in materials exposed to high temperatures

BOSTON UNIVERSITY

COLLEGE OF ENGINEERING

Dissertation

PHASE TRANSFORMATIONS AND CHEMICAL INTERACTIONS IN MATERIALS EXPOSED TO HIGH TEMPERATURES

by

JICHENG GUO

B.S., East China University of Science and Technology, 2010
M.S., Université de Picardie Jules Verne, 2012

Submitted in partial fulfillment of the

requirements for the degree of

Doctor of Philosophy

2018

Approved by

First Reader

Soumendra N. Basu, Ph.D.
Professor of Mechanical Engineering
Professor and Associate Division Head of Materials Science and Engineering

Second Reader

Uday B. Pal, Ph.D.
Professor of Mechanical Engineering
Professor of Materials Science and Engineering

Third Reader

James C. Bird, Ph.D.
Assistant Professor of Mechanical Engineering
Assistant Professor of Materials Science and Engineering

Fourth Reader

Srikanth Gopalan, Ph.D.
Associate Professor of Mechanical Engineering
Associate Professor of Materials Science and Engineering

DEDICATION

I would like to dedicate this work to my grandfather, Jingchun Guo.

ACKNOWLEDGMENTS

I would like to express my sincere gratitude to my advisor, Prof. Soumendra, N. Basu, for accepting me as a student in his group. Without his continuous support and guidance throughout my Ph.D. research, this dissertation would not be possible. I would like to thank Prof. Uday B. Pal for his encouragement and advice during my research. I sincerely appreciate Prof. Bird for his guidance and help. I would like to thank Prof. Srikanth Gopalan for serving in my dissertation committee. I would also like to thank Prof. David Bishop for chairing my defense committee.

I would like to thank Mr. Bob Sjostrom, Mr. David Campbell, Ms. Kara Mogensen, Ms. Anlee Krupp for their technical assistance. I would also thank Dr. Alexey Nikiforov for his support in transmission electron microscopy studies. I appreciate Ms. Elizabeth Flagg and Ms. Ruth Mason for their administrative help.

I would like to thank my colleague and officemate, Dr. Mustafa Ordu, for his collaboration and help in the fiber fabrication project. I would like to thank Dr. Yang Yu for his assistance with transmission electron microscopy studies. I would also like to thank all my colleagues at Boston University, Dr. Xiaofei Guan, Dr. Deniz Cetin, Dr. Yiwen Gong, Dr. Thomas Villalon, Zhihao Sun, Yanchen Lu, Paul Gasper, Jane Banner, and Dr. Ran Zhang for their collaboration, help and friendship.

I would also like to express my gratitude to my supervisor at Argonne National Laboratory, Dr. Mark Williamson, for his support and help during my visit and research. I would also like to thank Dr. Augustus Merwin for his guidance and encouragement in the molten salt structure study. I would also like to thank Dr. Chris Benmore from the

Advanced Photon Source of Argonne National Laboratory for his help and support in synchrotron experiments. I would also like to thank all my colleagues at Argonne National Laboratory, Dr. William Ebert, Dr. Nathan Hoyt, Dr. Melissa Rose, Dr. Jeffrey Fortner and Dr. Shilei Li, for their collaboration and help. I appreciate Ms. Mary Nunez and Ms. René Blasier for their administrative support.

Most importantly, I would like to express my sincere thanks to my parents, Du Guo and Yafeng Wu, for their continuous support throughout my life. I would also like to thank my dear wife, Yangyang Li, for her patience and unconditional love. I would also like to thank my son, Maximilian Guo, for the joy he brings to my life.

This research has been funded in part by NSF grants CMMI-1301108 and PFI:AIR-TT-1601583.

PHASE TRANSFORMATIONS AND CHEMICAL INTERACTIONS

IN MATERIALS EXPOSED TO HIGH TEMPERATURES

JICHENG GUO

Boston University College of Engineering, 2018

Major Professor: Soumendra N. Basu, Ph.D., Professor of Mechanical Engineering, Professor and Associate Division Head of Materials Science and Engineering,

ABSTRACT

Phase transformations and chemical interactions occur in many materials systems exposed to elevated temperatures. In this study, materials exposed to high temperatures in three distinctive applications, have been examined.

The first application involves the fabrication of semiconductor-core optical fibers for mid-infrared transmission. Such fibers can be used for chemical sensing, threat detection, and bio-imaging. In this study, germanium-core borosilicate glass cladded fibers were fabricated using rod-in-tube drawing. An analytical model for the deformation and heat transfer in the fiber preform during the high temperature fabrication process was developed. The solidification of the germanium core was experimentally studied using a proxy system of melting ice in a tube. The relative roles of conductive and convective heat transfer in determining the melting mechanism was analyzed. The fabricated fibers were characterized by various electron microscopy based techniques to understand impurity diffusion from the cladding to the core, as well as to study the crystalline quality of the Ge core.

The second application involves solid oxide membrane (SOM) based electrolytic

production of silicon, where the interaction between the ceramic membrane and the molten salt is the key in determining the lifetime of the membrane. The yttria-stabilized zirconia (YSZ) membrane was found to degrade over time due to chemical interactions with the silica-containing molten oxy-fluoride flux. These interactions led to the formation of a yttria depletion layer in the YSZ in contact with the molten salt. A series of flux compositions were designed to systematically test the correlation between flux optical basicity, yttria activity and YSZ membrane degradation. The results provide a guideline for eliminating membrane degradation during the production of silicon using the SOM electrolysis process.

The third application involves molten mixtures of lithium chloride and metallic lithium for metal oxide reduction application. These mixtures exhibit anomalous physical properties that lack a comprehensive explanation. In this study, the structures of bulk molten LiCl and LiCl-Li mixtures were investigated using an *in-situ* high-energy x-ray diffraction (HEXRD) technique. The structure factors and the pair distribution functions (PDF) of LiCl-Li mixtures were compared with those of pure LiCl. The results suggest Li disperses in LiCl as nano-clusters.

TABLE OF CONTENTS

LIST OF TABLES

LIST OF FIGURES

LIST OF ABBREVIATIONS

BF ..... Bright Field

CTE ..... Coefficient of Thermal Expansion

EBSD ..... Electron Backscatter Diffraction

EDX ..... Energy Dispersive X-ray

FIB ..... Focus Ion Beam

FT-IR ..... Fourier Transform Infrared

HAADF ..... High Angle Annular Dark Field

HEXRD ..... High Energy X-Ray Diffraction

HP-CVD ..... High Pressure Chemical Vapor Deposition

HRTEM ..... High Resolution Transmission Electron Microscopy

IR ..... Infrared

PCM ..... Phase Change Material

PDF ..... Pair Distribution Function

PVC ..... Polyvinyl chloride

QCL ..... Quantum Cascade Laser

SAD ..... Selected Area Diffraction

SEM ..... Scanning Electron Microscopy

SOM ..... Solid Oxide Membrane

STEM ..... Scanning Transmission Electron Microscopy

TEM ..... Transmission Electron Microscopy

YDL ..... Yttria Depletion Layer

YSZ.....Yttria Stabilized Zirconia

1. Background and Overview

Chemical interactions and phase transformations in materials under high temperatures occur in many applications. If such interactions are desirable, high temperatures may provide advantages over room temperature interactions, such as higher reactivity rate, higher energy efficiency and absence of aqueous solutions. However, deleterious effects such as corrosion, and complexity of atmosphere control are also exacerbated at higher temperatures. Moreover, availability of physical and chemical properties of materials at high temperature is still limited, making predictive behavior of high temperature materials and systems more challenging. This research involves the study of the materials interactions and phase transformation at high temperatures in three diverse applications.

The first application is the fabrication of semiconductor-core optical fibers for mid-infrared transmission. In this study, the deformation, heat transfer and phase change in the fiber preform were modeled to optimize the high temperature fiber drawing process. The drawn fibers were also characterized using electron microscopy based techniques to identify the potential sources of transmission losses. The second application is the electrolytic production of solar grade silicon using a solid oxide membrane (SOM) based system in which silica is dissolved in a molten fluoride-based flux. In this study, the corrosion of the yttria stabilized zirconia (YSZ) SOM membrane when exposed to silica containing oxy-fluoride flux at high temperatures was exanimated as a function of flux composition. An optimal flux composition is proposed to optimize the process. The third application involves reduction of metal oxides using molten lithium chloride and lithium

mixtures. For this application, the molten LiCl-Li mixture was characterized using the synchrotron based High Energy X-Ray Diffraction (HEXRD) technique. The obtained paired distribution functions (PDF) was studied to understand the structure of molten lithium chloride and lithium mixtures.

In this document, the fabrication of semiconductor-core optical fibers is discussed in Chapter 2, the corrosion of SOM-based electrolytic production of Si is discussed in Chapter 3, and the structure of molten LiCl-Li mixtures is discussed in Chapter 4. Each chapter contains its own introduction, experimental details, and results and discussion sections. Chapter 5 is the conclusion section for the entire dissertation.

2. Semiconductor Core Optical Fibers for Mid-Infrared Transmission

2.1 Introduction

Optical fibers are widely used in modern communication applications. The 2009 Nobel Prize in Physics was awarded to Dr. Charles Kao for "groundbreaking achievements concerning the transmission of light in fiber for optical communication" [1]. A majority of optical fibers used for optical communications are made by subjecting silica glass preforms through the fiber drawing process [2]. The optimum wavelength of light guided in silica glass fiber is 1.55 μm since it sits at the cusp of Rayleigh scattering at lower wavelengths and infrared absorption at higher wavelengths, as shown in Figure 1. Light with wavelengths in the mid-infrared range (λ=2-10μm) suffers high transmission losses in silica fibers.

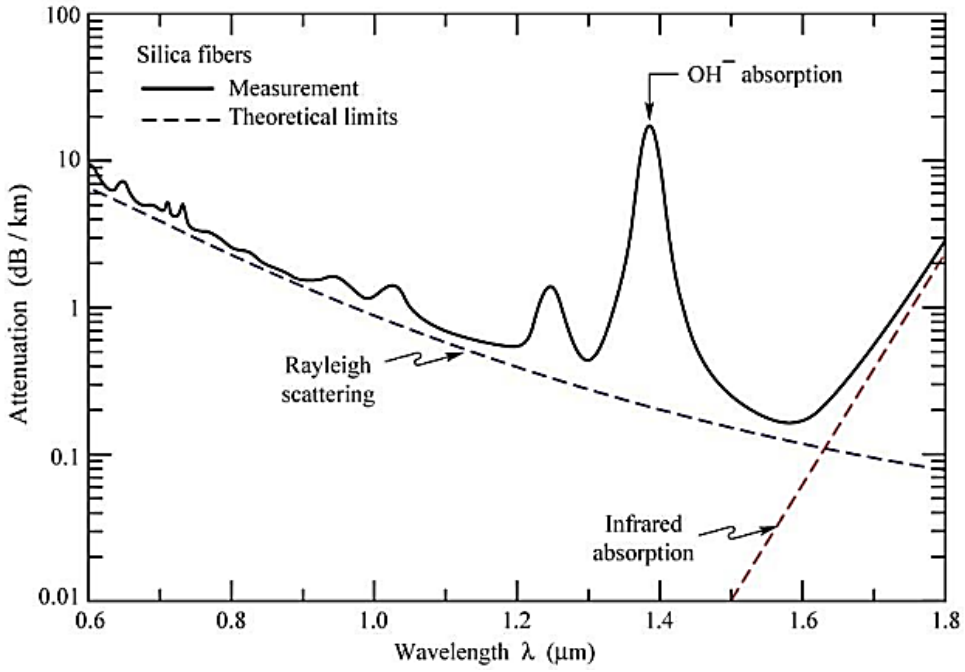

Figure 1. *Transmission of silica fibers and theoretical limitations [3].*

Optical fibers that transmit in the mid-infrared (IR) region are receiving increasing attention because they have a variety of potential applications, including chemical sensing [4], biomedical surgery [5], and aircraft threat detection, among others. Several mid-IR transmitting materials have been used to fabricate optical fibers over the years, including heavy metal oxides [6], crystalline halides [7 8], fluoride glasses [9] and chalcogenide glasses [10 11]. These as-fabricated fibers have acceptable mid-IR transmission losses, but suffer from room temperature devitrification, which limit their applications due to property degradation over time. In the last decade, semiconductor materials have become an emerging candidate for mid-IR fiber cores [12]. Fabrication methods such as high-pressure vapor chemical deposition (HP-CVD) [13-15] and 'rod-in-tube' drawing [16 17] have been explored for these materials. The HP-CVD method has limitations on the fiber length into which the core can be deposited. The 'rod-in-tube' method has been used to fabricate germanium core fibers with silica [16] and borosilicate glass [17] claddings. Silica has a large coefficient of thermal expansion (CTE) mismatch with germanium, leading to crack formation in the fibers. Borosilicate glass has a much better CTE match with germanium, and it features lower working temperatures. However, previous attempts to fabricate mid-IR transmitting Ge-core/borosilicate glass cladded fibers have large transmission losses, presumably due to impurity diffusion from the cladding to the core [17].

In the present work, Ge-core/borosilicate glass cladded fibers, which exhibit mid-IR transmission, were fabricated[1] by the 'rod-in-tube' method as shown in Figure 2. The

[1] Fiber fabrication by Dr. Mustafa Ordu.

fiber deformation and heat transfer at high temperatures were studied to build models to guide the fiber fabrication process. The microstructures of the fabricated fibers were examined, and strategies to further reduce transmission losses were explored in this study.

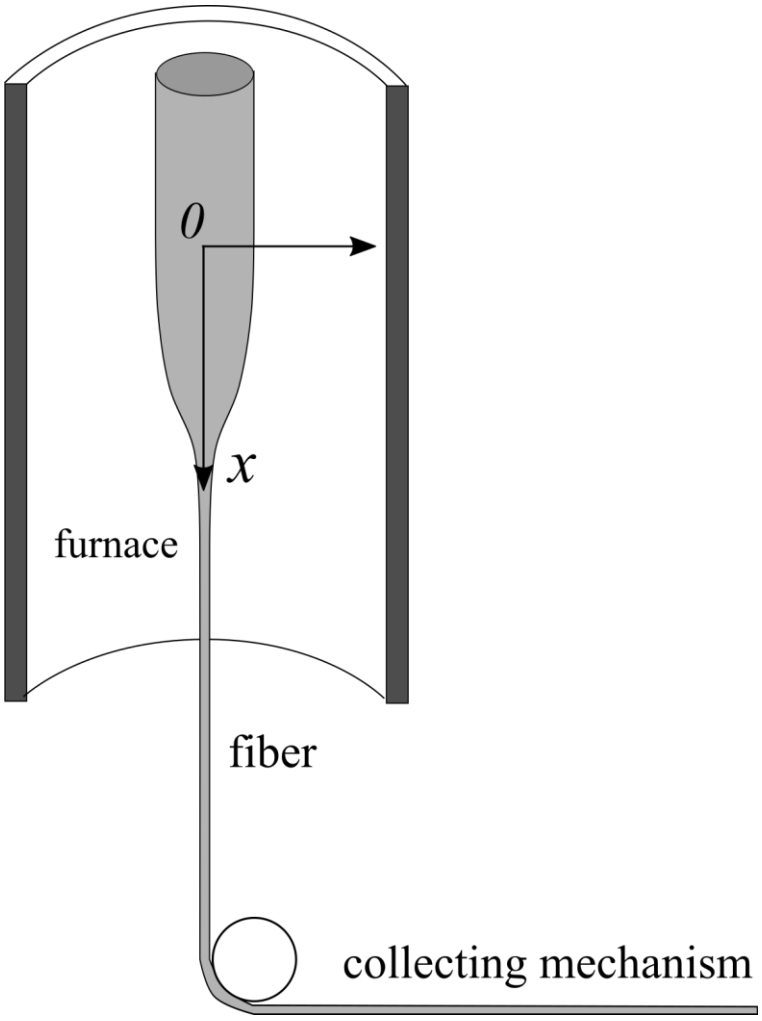

Figure 2. *Schematic of the fiber drawing process.*

2.1.1 Neck formation

In a typical fiber drawing process, the glass preform with the germanium core is heated in the tube furnace to a temperature that germanium core melts and the glass cladding softens, and then is pulled downwards by its own weight. During deformation, a

‘neck’ forms on the preform, as shown in Figure 2, where the rate of reduction of the cross-sectional area is the fastest. As a result, a stable cross-section that is significantly smaller than the diameter of the original preform, is reached.

The location where this neck forms is crucial to determine optimal position of the germanium core in the preform. The germanium core needs to be placed right above the neck (e.g. 1-3 cm above) to ensure the successful fabrication of germanium core fiber. If the rod is below the neck, the drawn fiber will not have a semiconductor core. If it is well above the neck, the molten Ge will remain in contact with the cladding at elevated temperatures for long periods, increasing the extent of impurity diffusion.

The neck formation is a result of the balance between forces (e.g. gravity and viscosity) and the conservation of mass [18]. Since the viscosity of fiber preform is a function of temperature, it is important to understand the heat transfer process in the preform. Previous studies have focused on the shape of the neck when the fiber is pulled at a constant speed [18 19]. In this study, the neck location is estimated numerically for a static perform located in the furnace at working temperature.

2.1.2 Heat transfer with phase change

During the fiber fabrication process, the germanium core undergoes a solidification process after leaving furnace hot zone. The solidification of Ge core in the borosilicate glass cladding is a heat transfer process that involves phase changes. Since the fiber core diameter is of the order of tens of microns, the solidification times are of the order of

milliseconds. Thus, it is difficult to capture the solidification process through experimental methods. Instead, the melting of ice inside cylindrical containers is experimentally studied, and modelled, which is qualitatively similar to the reverse process of Ge core solidification, i.e., the melting of the germanium core inside the glass cladding.

Melting of phase change materials (such as ice/water) inside horizontal cylindrical containers under constrained (fixed in the center) [20 21] and unconstrained (free to float/sink) [22-24] configurations have been investigated previously. In the unconstrained configuration, due to the density difference of solid phase and liquid phase, gravity brings the solid phase change material (PCM) in closed contact with container inner surface and is separated by a thin continuously forming liquid layer. In this study, the detailed melting mechanisms of ice melting in an unconstrained fashion in copper and plastic (polyvinyl chloride (PCV)) tubes have been experimentally investigated. The experimental results are explained using an analytical model. The obtained model can be applied to fiber fabrication and to PCM energy storage applications [25-28].

2.2 Experiments and Results

2.2.1 Modeling of Neck Formation

2.2.1.1 Geometry and Governing Equations

The geometry and initial position of fiber preform are shown as schematics in Figure 3 and Figure 4. The fiber preform is placed in a vertical tube furnace with its lower end slightly above the bottom of the furnace tube. In the figures, *L* is the initial length of the fiber preform inside the furnace, and *L'* is the length of heating zone of the furnace. The *x*-axis points along the axial direction of the fiber preform with the origin at the top of the furnace heating zone with a downward positive direction. The *r*-axis points along the radical direction of the fiber preform with the origin at the center of the preform cross-section with an outward positive direction. *R* is the radius of the fiber preform and *R'* is the radius of the furnace inner wall as shown in Figure 4

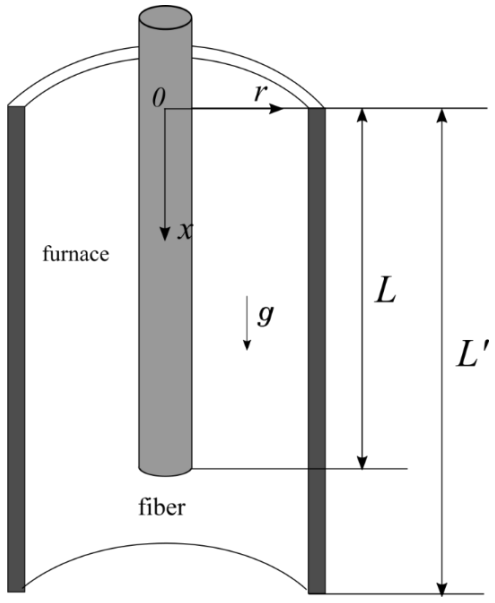

***Figure 3**. The geometry and position of the fiber drawing setup.*

To predict the time dependent deformation of the preform, the 'Trouton' model [29] was applied. Since the glass preform is a highly viscous and slender cylinder object, its deformation can be described using Stoke's equations. The kinematic and zero-stress boundary conditions are applied at the free surface. The solution to the Stoke's equation for an axisymmetric fiber in leading order of asymptotic expansions according to the 'Trouton' model can be written as:

conservation of mass, given as:

$$\frac{\partial A}{\partial t} + \frac{\partial}{\partial x}(uA) = 0 \tag{1}$$

and stress balance between gravity and viscosity, given as:

$$\frac{\partial}{\partial x}\left(3A\mu\frac{\partial u}{\partial x}\right) = -\rho g A \tag{2}$$

Here, $A = \pi R^2$, is the cross-section area of the fiber preform, u is the velocity of the preform in x direction, ρ is the density of the fiber preform material and μ is the dynamic viscosity of the fiber preform. The surface tension force is ignored here since viscous forces are 10^3-10^9 times greater than the surface tension forces in this application [29]. The governing equations are then non-dimensionalized (with non-dimensional terms indicated with primes) as following:

$$A = \epsilon^2 L^2 A' \; ; \; u = U u'$$

$$t = (L/U)t' \; ; \; x = L x' \; ;$$

$$\mu = \frac{L^2 \rho g}{U}\mu' \tag{3}$$

This yields non-dimensional, scaled equations, given as:

$$\begin{cases} \dfrac{\partial A^{'}}{\partial t^{'}} + \dfrac{\partial}{\partial x^{'}}\left(u^{'} A^{'}\right) = 0 \\ \dfrac{\partial}{\partial x^{'}}\left(3A^{'} \mu^{'} \dfrac{\partial u^{'}}{\partial x^{'}}\right) = -A^{'} \end{cases} \tag{4}$$

After dropping the primes, Equation 4 can be expressed as:

$$\begin{cases} \dfrac{\partial A}{\partial t} + \dfrac{\partial}{\partial x}(uA) = 0 \\ \dfrac{\partial}{\partial x}\left(3A\mu \dfrac{\partial u}{\partial x}\right) = -A \end{cases} \tag{5}$$

with boundary conditions, given as:

$$\begin{cases} u(0,t) = 0 \\ A(x,0) = A_0 \end{cases} \tag{6}$$

Since the length of the fiber is increasing throughout this process, Lagrangian transformation is used to solve these equations, given as:

$$\begin{cases} \dfrac{\partial}{\partial \tau} = \dfrac{\partial}{\partial t} + u\dfrac{\partial}{\partial x} \\ \dfrac{\partial}{\partial \xi} = \dfrac{\partial x}{\partial \xi}\dfrac{\partial}{\partial x} \end{cases} \tag{7}$$

Thus, the governing equations are transformed as:

$$\begin{cases} \dfrac{\partial}{\partial \tau}\left(A\dfrac{\partial x}{\partial \xi}\right) = 0 \\ 3\dfrac{1}{\dfrac{\partial x}{\partial \xi}}\dfrac{\partial}{\partial \xi}\left(-\dfrac{\partial A}{\partial \tau}\mu\right) = -A \end{cases} \tag{8}$$

with the boundary conditions,

$$\begin{cases} x(\xi) = 0 \; at \; \xi = 0 \\ x(\xi) = \ell(\tau) \; at \; \xi = 1 \\ A(x(\xi), 0) = A_0 \end{cases} \tag{9}$$

From the transformed continuity equation $\frac{\partial}{\partial \tau}\left(A\frac{\partial x}{\partial \xi}\right) = 0$, it is clear that $A\frac{\partial x}{\partial \xi}$ is only a function of ξ, and not a function of τ. By applying the boundary condition, $A(x(\xi),0) = A_0$, the function is obtained as $A\frac{\partial x}{\partial \xi} = A_0(\xi)$. Then, the stress balance equation can be transformed to,

$$3\frac{\partial}{\partial \xi}\left(\frac{\partial A}{\partial \tau}\mu\right) = A_0(\xi) \tag{10}$$

Since the initial shape of the preform is a straight cylinder (with no neck), the initial condition can be written as $A_0 = 1$. Based on experimental observations, the bottom of the fiber does not deform during the drawing process, so the boundary condition: $\partial A/\partial \tau = 0$ at $\xi = 1$, is also applied to the bottom of the fiber, leading to:

$$A(\xi) = \frac{\tau}{3}\frac{(\xi - 1)}{\mu} + 1 \tag{11}$$

Also, from $A\frac{\partial x}{\partial \xi} = A_0(\xi)$, the total length of the fiber preform can be expressed as,

$$\ell(\tau) = x(1) - x(0) = \int_0^1 \frac{A_0(\xi)}{A(\xi)} d\xi \tag{12}$$

By applying boundary conditions, the total length of the deformed preform can now be expressed as:

$$\ell(\tau) = \int_0^1 \frac{1}{\frac{\tau}{3}\frac{(\xi - 1)}{\mu} + 1} d\xi \tag{13}$$

2.2.1.2 Heat Transfer in the Preform

Since the viscosity of the borosilicate glass varies with the temperature of the fiber preform, it is important to understand the heat transfer process in the fiber preform. For the preform placed in the tube furnace, radiation is the primary heat transfer mechanism [18]. In the radiation model, the surfaces of the glass preform and the tube furnace are both considered as gray bodies. The radiation from the furnace surface to the preform surface is estimated as:

$$q_{21} = \frac{E_{b2} - E_{b1}}{\frac{1 - \varepsilon_1}{\varepsilon_1 A_1} + \frac{1}{A_1 F_{12}} + \frac{1 - \varepsilon_2}{\varepsilon_2 A_2}} \tag{14}$$

where E_{b2} is the energy flux from furnace surface, E_{b1} is the energy flux from the preform surface, ε_2 and ε_1 are the emissivity of the two surfaces, A_2 and A_1 are the surface areas of the furnace and preform, respectively. F_{12} is the view factor from furnace surface to the preform surface.

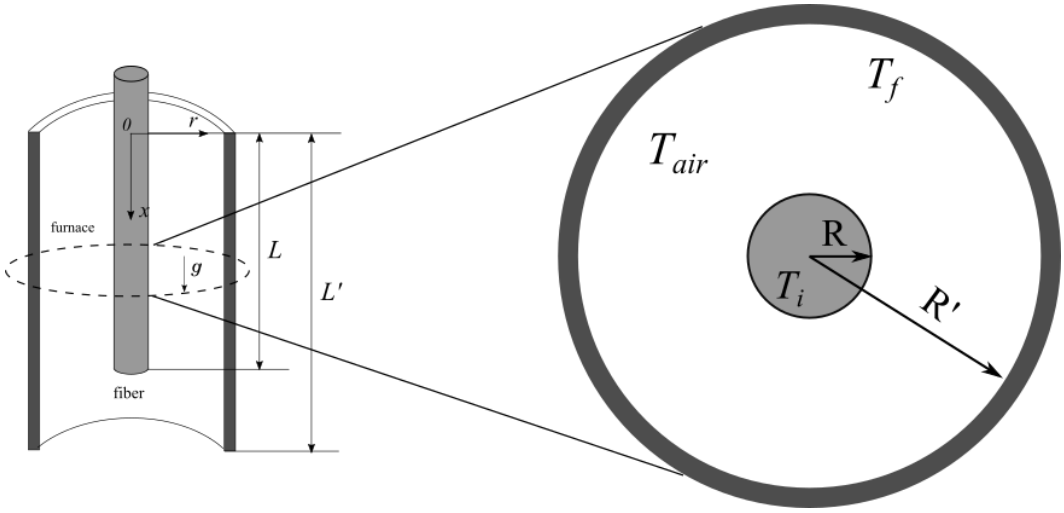

Figure 4. *Cross-section view of the fiber preform and furnace during drawing.*

In addition to thermal radiation, thermal conduction through air from the furnace to the preform and inside the preform also takes place, and can be described as:

$$q = -k\nabla T \tag{15}$$

where k is the thermal conductivity. In the model, the fiber preform at room temperature is introduced into the hot furnace, where the furnace surface and the air inside are at elevated temperature.

Table 1. Materials properties used in heat transfer simulations

Physical Properties	**Value**
Emissivity of furnace wall (ε_2)	0.8
Emissivity of preform (ε_1)	0.6
Thermal conductivity of air (k_{air})	8.58×10^{-2} W/(m·K)
Thermal conductivity of preform (k_i)	1.2 W/(m·K)

Density of air (ρ_{air})	0.26 kg/m^3
Density of preform (ρ_i)	2230 kg/m^3
Specific heat of air (C_{air})	1.197 kJ/(kg·K)
Specific heat of preform (C_i)	0.9 kJ/(kg·K)

Since 3D numerical modeling of the thermal transfer process in the fiber preform is computationally expensive, the heat transfer process of a 2D cross-section of the system (Figure 4) is constructed in COMSOL Multiphysics®. The initial conditions and materials properties are listed in Table. 1. The heat transfer process is simulated for three different preforms at different temperatures. The initial conditions and geometry of these three preforms are listed in Table. 2 with the length of the furnace L' = 35cm and radius R' = 3.8cm.

Table 2. Initial conditions for the heat transfer simulations

Preform	**Radius (*R*)**	**Length (*L*)**	**Furnace and Air Temperature (T_f and T_{air})**	**Initial Preform Temperature (T_i)**
1	0.45cm	32.5 cm	1433K	298K
2	0.7cm	25 cm	1333K	298K
3	1cm	25 cm	1433K	298K

The simulated 2D temperature profile of *Preform 1* at t = 20s is shown in Figure 5, as an example. In the plot, there is a temperature gradient from the surface to the center of the preform. To simplify the model, the temperature of this cross-section is assumed to be

uniform, and equal to the average temperature of the cross-section. The time dependent average temperature variation of the preform at that location is shown in Figure 6.

The axial temperature profile of the furnace heating zone is assumed to be a Gaussian, with the highest temperature located in the middle of the furnace as shown in Figure 7. As mentioned previously, in order to restrict the simulation to 2D, it is assumed that there is no axial heat transfer along the preform. As a result, the axial temperature profile of the preform follows that of the furnace heating zone as shown in Figure 7.

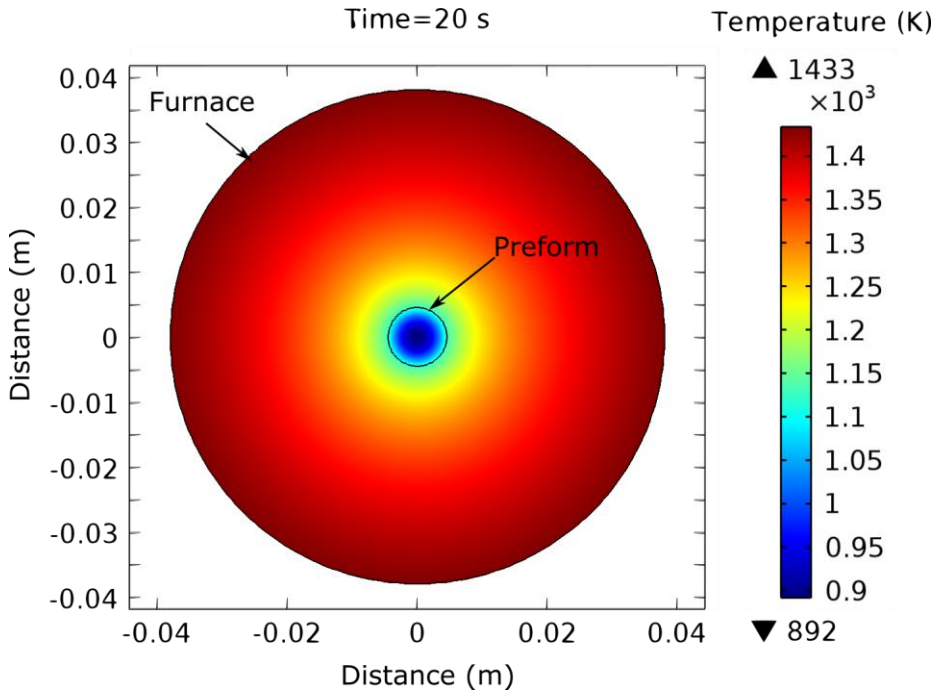

Figure 5*. Simulated temperature profile of fiber preform and furnace cross section.*

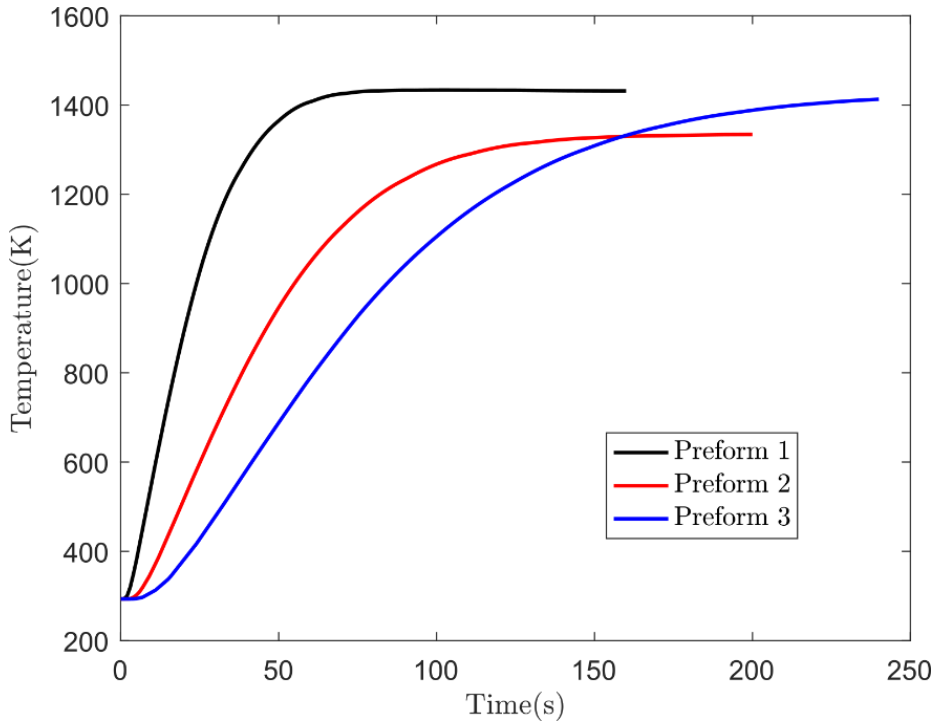

Figure 6. *The temperature variation of the preform at the simulated location.*

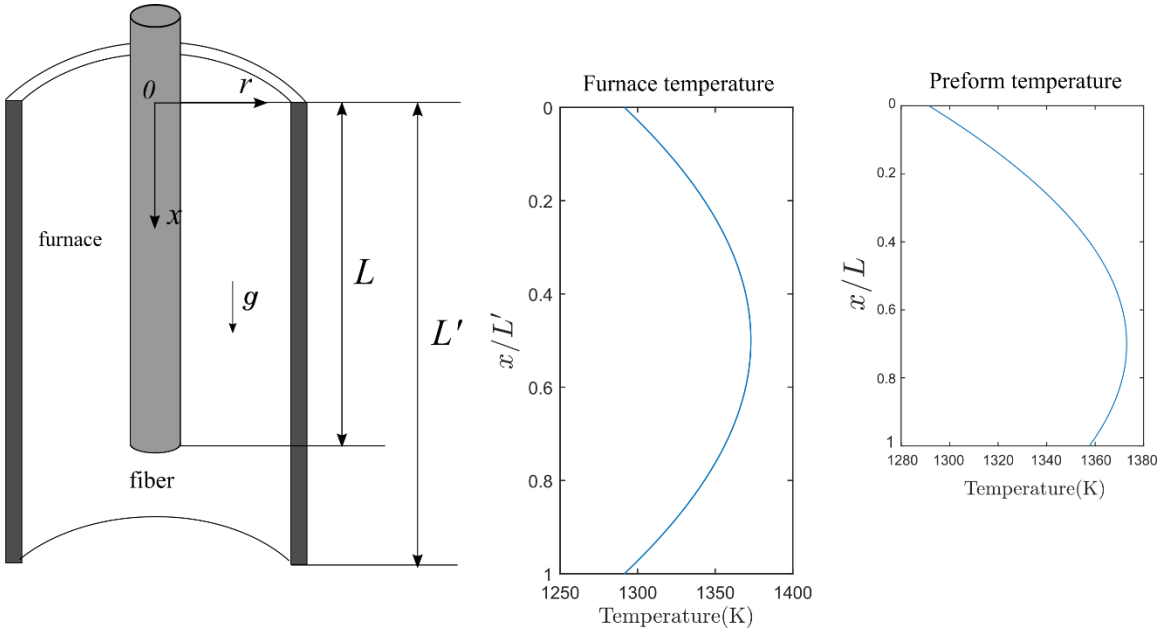

Figure 7. *Schematic of the preform location inside furnace, the furnace axial temperature profile and the preform axial temperature profile.*

The viscosity of the glass preform is temperature dependent, and the relationship can be expressed as [30]:

$$\mu = 10^{-2.15+7254.8/(T(x,t)-342.3)} \tag{16}$$

Thus, for each individual preform, the time dependent variation of viscosity profile along the x-axis was obtained.

2.2.1.3 Simulation and Validation

The perform viscosity profile obtained from the thermal transfer modeling is coupled with the analytical solution obtained from the 'Toutron' model in MATLAB®. The deformation of the fiber preform in the furnace under the influence of varying viscosity was simulated. Figure 8 shows the simulated deformation profile and the viscosity profile along the x-axis of *Preform 1* from t=40s to t=50s. The figure shows that, as time increases, the viscosity decreases while the deformation increases and a neck starts to form. The simulation results in Figure 9 and Figure 10 show the time dependent variation of the cross-section area profile and the total length of *Preform 1* for the time period from t = 30s to t = 50s. From these results, the neck location and necking time can be predicted. For example, the neck on the *Preform 1* starts at around x = 0.3 which is 9 cm from the top of the heating zone. The necking time is defined as the thinnest region along the preform is 0.75 of its initial value, so for *Preform 1*, the necking time is around 45s. The simulated results are compared with the experimental results in Table 3. The modeled results are in good agreement with the experimental results.

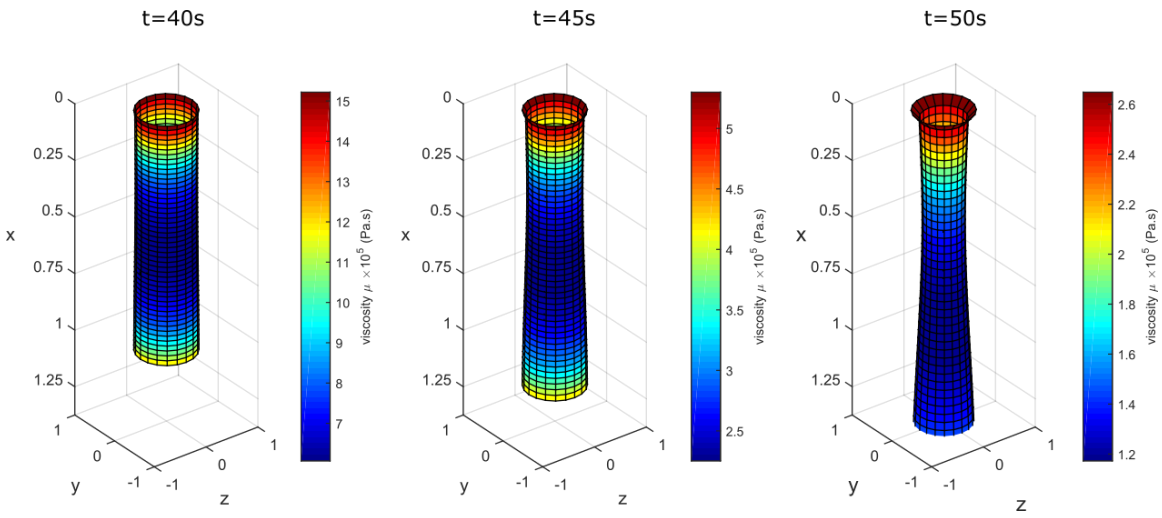

Figure 8. *Simulated deformation and viscosity profile of Preform 1 during drawing process.*

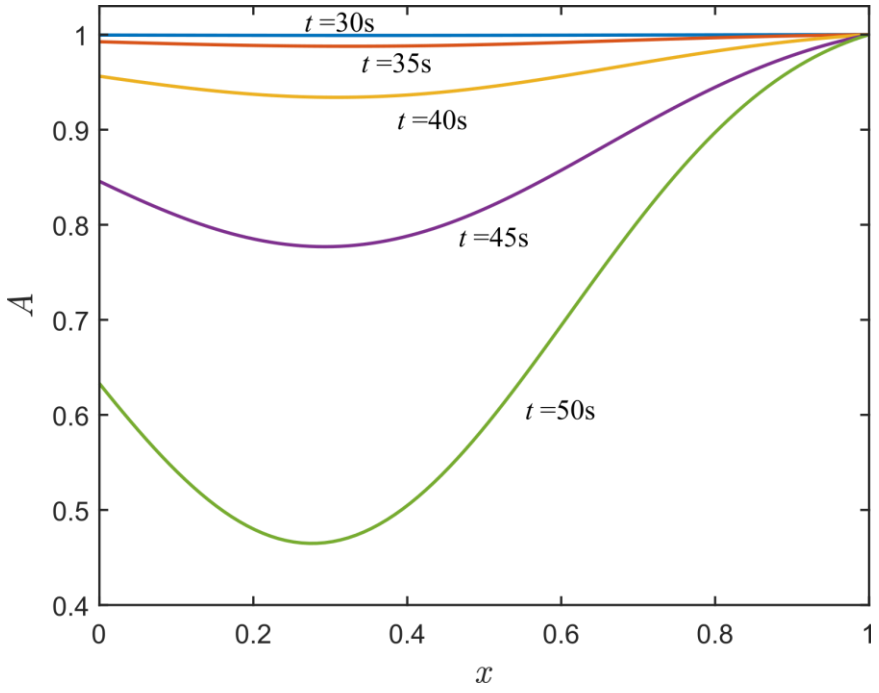

Figure 9. *Cross section area profile along the x axis of Preform 1 as a function of time.*

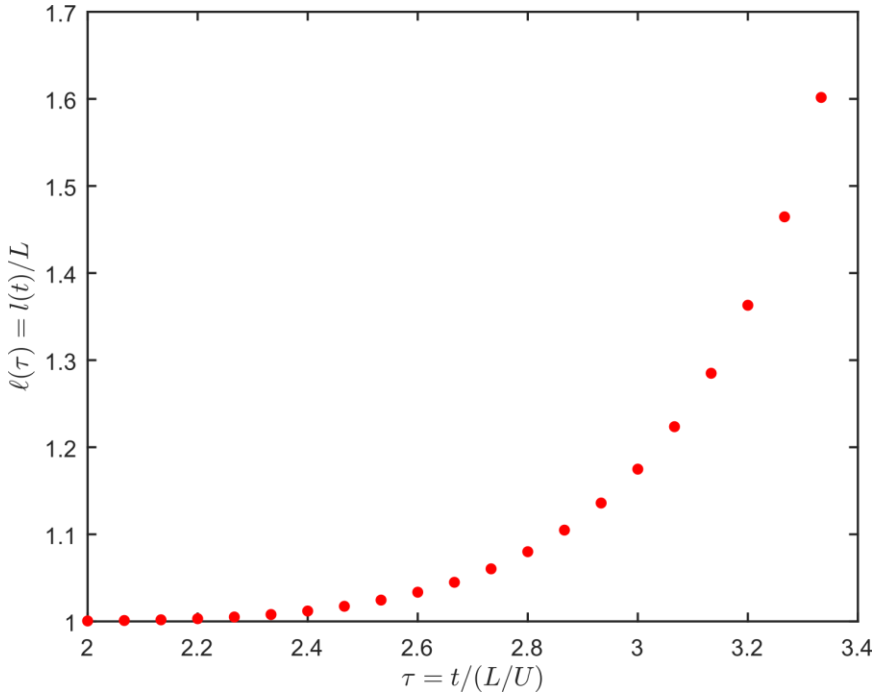

Figure 10. *Variation in the non-dimensionalized length of Preform 1as a function of non-dimensionalized time.*

Table 3. Neck formation simulation data and experimental results

Preform	**Simulated neck location *x* (cm)**	**Experimental neck location *x* (cm)**	**Simulated necking time (s)**	**Experimental necking time (s)**
1	9.75	9	45	64
2	10	10	120	97
3	10	9	145	175

2.2.2 Germanium-Core Fiber Characterization

Mid-IR transmitting Ge-core/borosilicate glass cladded optical fibers were fabricated at 1000°C by the 'rod-in-tube' method using a mini draw tower built in-house.[2] The results reported in this section is based on fibers drawn from a 9mm OD preform. The drawn fibers had a 40 µm Ge-core diameter and a 177 µm borosilicate glass cladding diameter. After drawing, the fibers were placed in epoxy, and the end was polished to observe the fibers in cross section using a Scanning Electron Microscopy (SEM) (Zeiss Supra 55, Carl Zeiss, Oberkochen, Germany). An optical micrograph of a 40µm Ge-core fiber is shown in Figure 11.

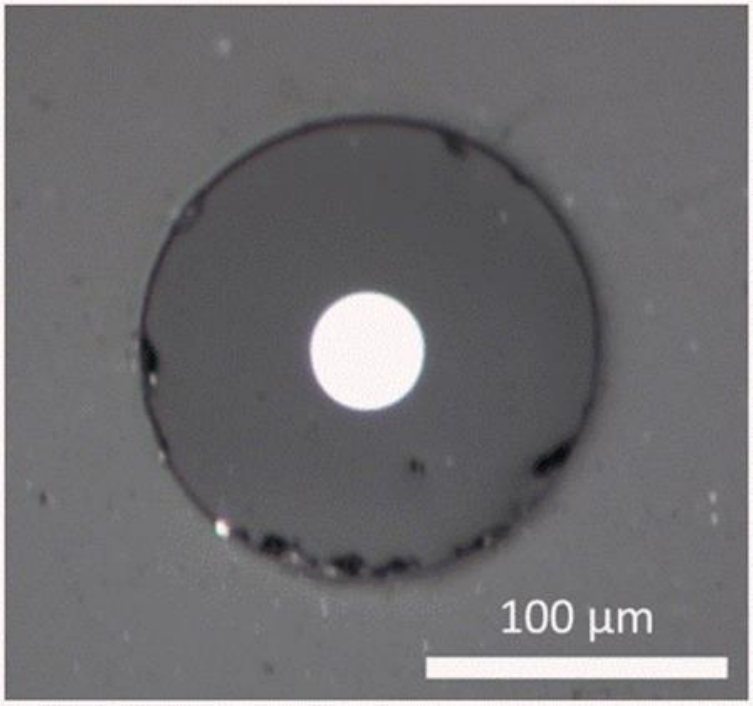

Figure 11. *Optical micrograph of a fabricated fiber cross section.*

[2] Fibers drawn by Dr. Mustafa Ordu

To test the optical performance of the fibers, the fibers were mounted in epoxy and polished at both ends. Before testing mid-IR transmission through the fabricated Ge core fibers, it is important to test the mid-IR transmissivity of all the materials in the mounted samples, to ensure that light is only transmitted through the fiber core. The transmission through epoxy and borosilicate glass in the 1.7-10μm wavelength range measured using Fourier transform infrared (FT-IR) spectroscopy (Bruker Optics Inc., Massachusetts) is shown in Figure 12a.[3] The figure clearly shows that that light transmission stops at wavelengths above 3.3μm and 2.1μm in the borosilicate glass and epoxy, respectively. On the other hand, the transmission spectra through an unprocessed germanium rod and a large diameter (~ 300μm) Ge-core fiber have similar shapes (Figure 12b), although the transmission loss in the cane is higher. This however demonstrates that a molten and re-solidified Ge-core does transmit mid-IR wavelengths.

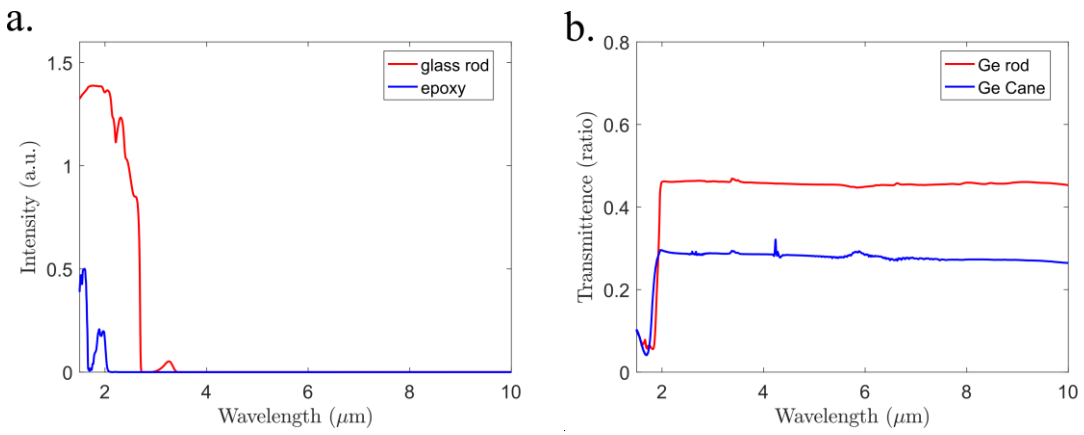

Figure 12. *Wavelength dependent FT-IR spectroscopy of (a) borosilicate glass and epoxy, and (b) unprocessed Ge rod and Ge cane.*

[3] Optical measurements conducted by Dr. Mustafa Ordu.

The transmission through a Ge-core fiber was tested using a quantum cascade laser (QCL) at wavelengths between 5.82 μm and 6.28 μm. The signal through fibers of different lengths (8.63, 8.25, and 7.91mm) are tested and compared with the output signal without a sample in the light path. The transmission loss at each individual length was calculated using:

$$\alpha = -\frac{10}{L}\log_{10}\left(\frac{P_0}{0.64^2 P_i}\right) \tag{17}$$

where L is the length of the fiber, P_i and P_0 are the fiber output power and background power respectively. This led to three sets of wavelength dependent transmission loss data whose wavelength dependent average values are plotted in Figure 13. Since the wavelength range tested is too narrow to deduce any meaningful trends with respect to wavelength dependence, an average transmission loss of all wavelength for all samples tested was then calculated to be 5.1dB/cm.[4]

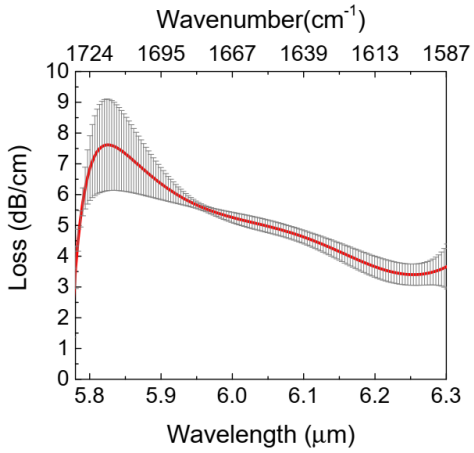

Figure 13. *Transmission losses in Ge-core fiber.*

[4] Optical measurements conducted by Dr. Mustafa Ordu.

To identify the cause(s) for the transmission loss, the fabricated fiber was characterized using electron microscopy based elemental analysis and diffraction analysis. Ballato et al. [17] have reported that the diffusion of light elements (e.g. oxygen) from the cladding into the core is one of the major causes of transmission loss in semiconductor core fibers. In order to study the diffusion profile at a high spatial resolution, electron transparent transmission electron microscopy (TEM) samples containing the fiber core/cladding interface were prepared using a focused ion beam (FIB; FEI, Oregon) based 'lift-out' technique. Elemental dot maps and composition profiles across the core-cladding interface were obtained by scanning/transmission electron microscopy (S/TEM; FEI, Oregon) and energy dispersive x-ray (EDX) spectroscopy at 200KV, using a 1nm diameter electron beam. Electron transparent samples were also made by standard polishing and ion milling techniques for high-resolution TEM (HRTEM) studies of the interface. Finally, the grain structure of the Ge core was also examined by electron back scattered diffraction (EBSD) mapping (Oxford Instruments, Concord, MA).

Figure 14a shows a TEM bright-field micrograph of the Ge-core/borosilicate glass-clad interface of fiber, along with EDX elemental dot maps of Ge, O and Si (Figure 14b-d), indicating that the glass/cladding interface is quite sharp. Figure 14e shows an EDX line-scan across a core/cladding interface region, indicating that the diffusion of the cladding components (Si, O, B, K, Na and Al) diffusion from cladding to core is minimal with the diffusion distances in the submicron regime. The low oxygen content of the core is likely a result of the low drawing temperature and is encouraging for mid-IR transmission since oxygen is known to increase mid-IR transmission losses in fibers. The

extent of impurity diffusion is significantly less than that reported by Ballato et al. for Ge-core borosilicate clad fibers [17].

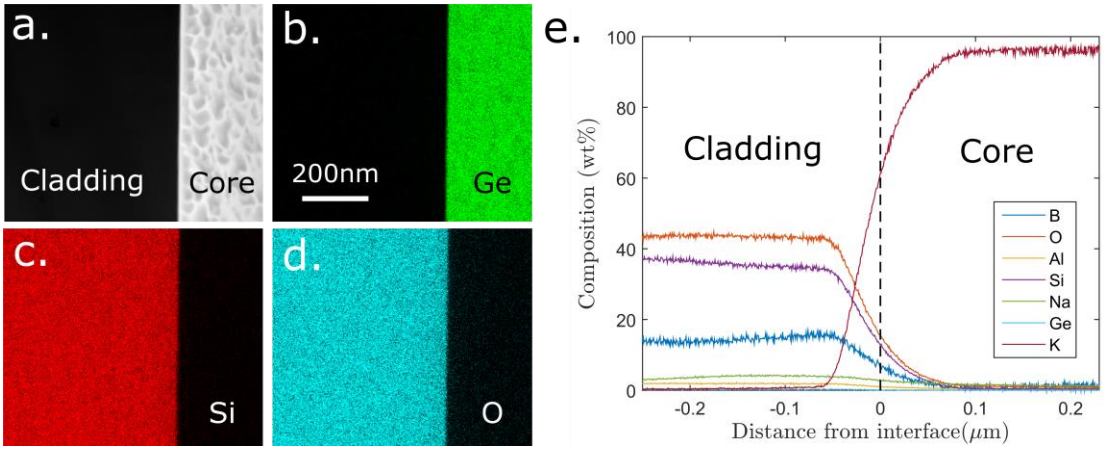

Figure 14. *(a) TEM bright-field micrograph of core/cladding interface of fiber. EDX dot maps of (b) Ge, (c) O, and (d) Si. (e) EDX line scan showing the composition profile of Si, Ge, O, B, K, Na, and Al across the core/cladding interface. The diffusion of oxygen from the cladding to the core is minimal.*

Figure 15a shows an HRTEM micrograph of core/cladding interface in the fiber. The crystalline quality of the Ge core is evident in the micrograph. A higher magnification HRTEM micrograph of the Ge core, imaged on the $[\bar{1}12]$ zone axis is shown in Figure 15b. A selected area diffraction (SAD) pattern from this grain is indexed as shown as an inset in Figure 15b. Clearly, the germanium core shows high crystallinity at the core/cladding interface.

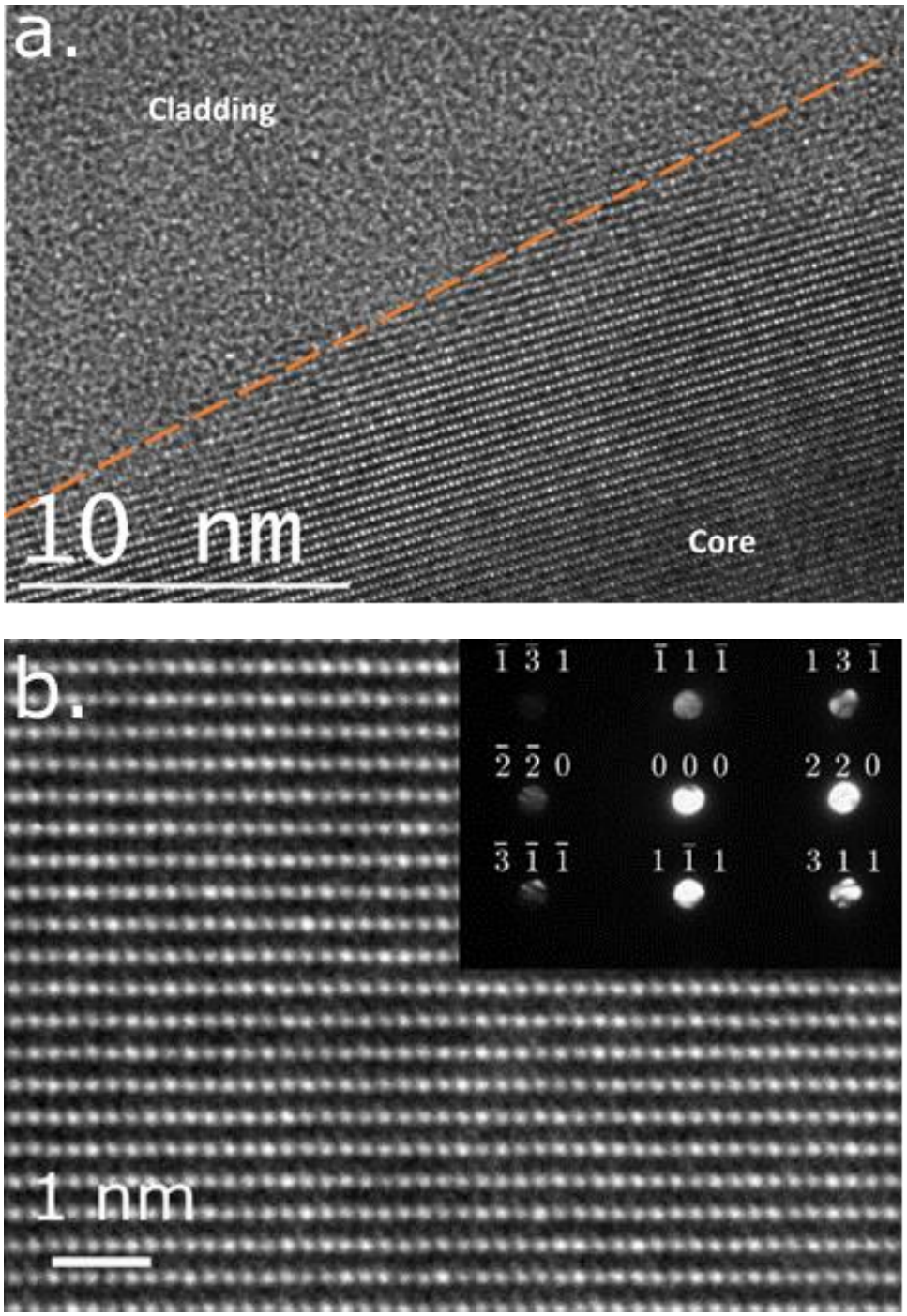

Figure 15. *(a) HRTEM micrograph the core/cladding interface in the Ge-core fiber. (b) HRTEM image of the Ge grain imaged along the* $[\bar{1}12]$ *zone-axis and SAD pattern (insert).*

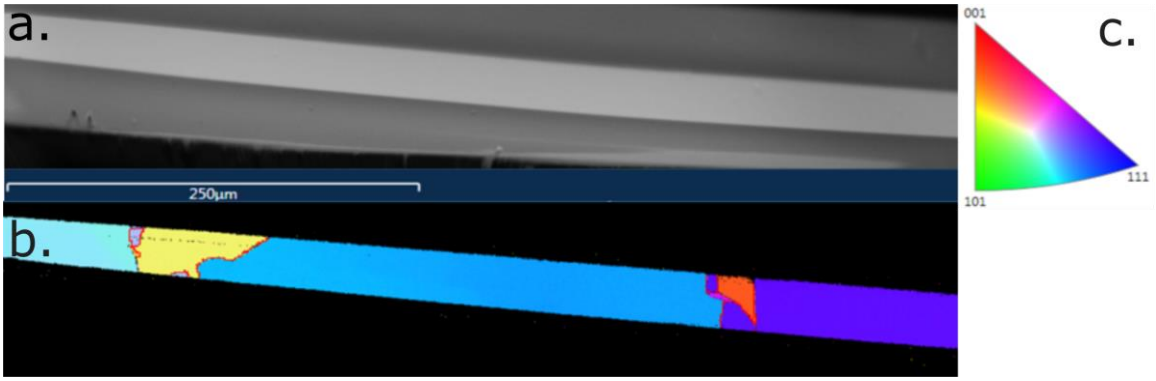

Figure 16. *(a) SEM micrograph of fiber polished along its length. (b) Orientation map measured by EBSD. The red lines show the presence of twin boundaries. (c) Orientation key used in the map in (b).*

In order to investigate the germanium core crystal orientation over a longer range (e.g. sub millimeter range), SEM based EBSD was carried on fibers polished in cross-section along the fiber length. The SEM image of the studied Ge-core fiber is shown in Figure 16a. EBSD mapping in Figure 16b shows the crystal orientation of different regions in the polished fiber with the orientation key shown in Figure 16c. The grains in the germanium core shows an average size of approximate 200µm with different crystal orientations. The grain boundaries in the fiber is also visible in this map. The red lines in Figure 16b shows the location of twin boundaries, which indicates that almost all the grain boundaries observed are actually twin boundaries.

It is clear that the diffusion of light elements into the core is significantly reduced. The germanium core exhibits high degree of crystallinity after re-solidification. For these reasons, the fabricated fibers reported here have the lowest measured losses for a Ge-core, borosilicate cladded optical fiber produced by the ‘rod-in-tube’ method [31]. However, grain boundaries are present in the fiber, which are probably one of the major reasons for

the measured transmission losses.

2.2.3 Ice Melting in a Tube: A Case of Heat Transfer with Phase Change

In order to reduce the transmission loss of fabricated fibers, materials engineering via post processing on fabricated fiber can be applied. Several post-processing techniques, such as tapering and laser treatment, have been developed to optimize both the materials and the geometry of the fibers. Among these techniques, furnace-based annealing of the fabricated fiber in horizontal configuration has been used to re-melt the core and directionally solidify to increase the grain size of the crystalline core [32]. It is important to estimate the time for core re-melt so the fiber exposure to the annealing process can be minimized.

Phase changes of the germanium core during post processing of the fiber is difficult to measure experimentally due to the high temperatures involved and the small sample dimensions. Melting of ice in horizontal cylindrical tubes have been experimentally studied and modeled as a proxy to the fiber core melting process.

2.2.3.1 Experiment details

The experiment set up is shown schematically in Figure 17a. The tube was held horizontally with well-circulated room temperature air around it. The geometry of the tube is shown in Figure 17b, where R is the initial radius of the ice rod, $\ell(t)$ is the effective radius of the ice rod during melting and L is the length of the tube. One end of the tubes

was sealed with a 5mm transparent PVC plate to provide a window to observe the melting process. The other end of the tube was sealed off by a 1 mm latex membrane to prevent air pocket generation resulting from the volume change accompanying the phase transformation.

De-ionized (DI) water was carefully de-gassed by boiling for 45 minutes prior to freezing. Thermocouples were placed both inside and outside the top surface of the tube for temperature measurements. A digital camera is placed at the PVC end of the tube to capture the time dependent melting process. A light source was applied on the back end of the tube for improved imaging. Experiments were carried out with PVC and copper tubes of various diameters at room temperature.

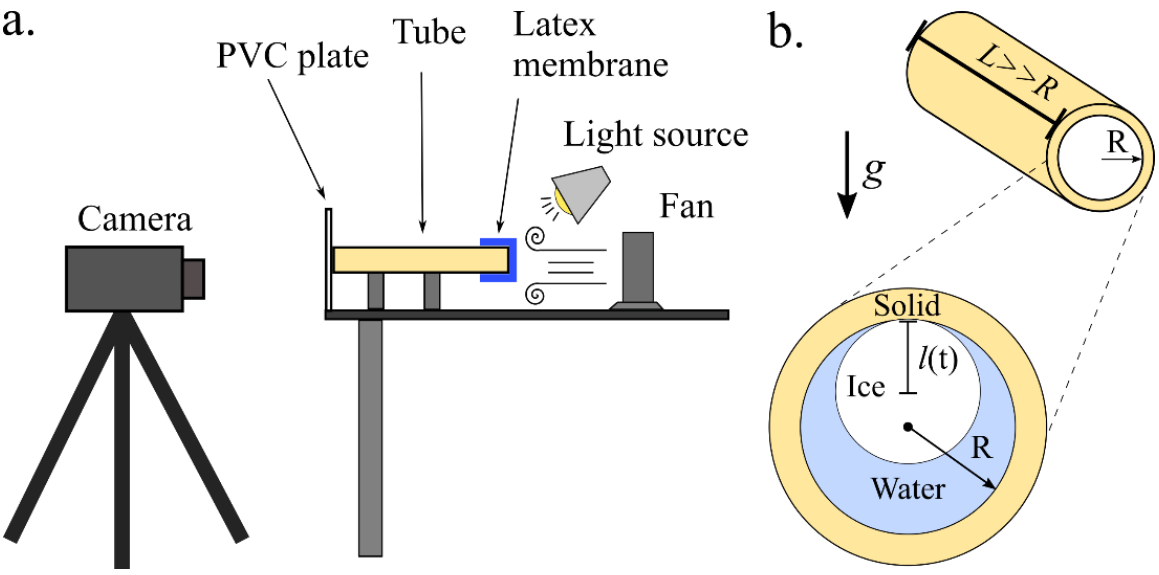

Figure 17. *(a) Schematic of the ice melting experiment. (b) Geometry of the tube used in the experiment.*

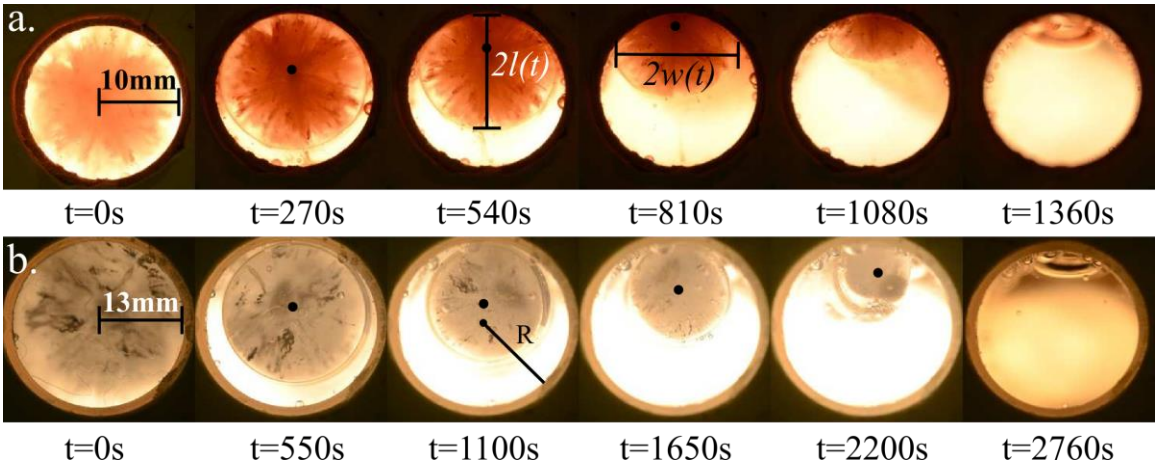

Figure 18. *(a) Time elapsed images of ice melting inside a copper tube. (b) Time elapsed images of ice melting inside a PVC tube.*

Time elapsed images of ice melting in Cu and PVC tubes are shown in Figure 18a and Figure 18b, respectively. Inside the Cu tube, the upper half of the ice rod melts more rapidly than the lower half. The imbalance in melting rates creates elliptical shaped cross-sections with the top part following the container wall curvature and the lower part relatively keeping its initial curvature as shown in Figure 18a. These observations agree those reported by Riviere et al. [24]. However, inside PVC tubes, the ice cylinder cross-section keeps its circular shape during most of the melting process.

2.2.3.2 Results and Discussion

From the time elapsed photos (e.g., Figure 18), the effective radius of the ice rod, ℓ, is plotted as a function of time in Figure 19a for Cu and PVC tubes of different diameters. The results indicates that, in general, the ice-melting time in the Cu tube is shorter than that in the PVC tube, and that the melting time increases with increasing ice rod diameter for

both cases. As seen in Figure 18a, once water from melted ice accumulates in the system, the ice rods rise as a result of buoyancy. The heat conduction is then concentrated at the top part of the tube as a result of the close contact between the ice and the top inner tube surface. [23] This configuration is qualitatively similar to the evaporation of a Leidenfrost drop that features a thin vapor layer between the water drop and hot surface. According to Bareiss et al. [23] and Biance et al. [33], the melting time can be scaled as:

$$\tau_c = \frac{\rho \mathcal{L} R \delta}{(T_i - T_m)\kappa_l}, \delta = (R\frac{\kappa_l(T_i - T_m)}{\rho \mathcal{L}}\frac{\mu}{\rho_l g})^{1/4} \tag{18}$$

where ρ is the density of ice, $\mathcal{L}$ is the latent heat of fusion of ice, R is the initial radius of ice rod, T_i is the container inner wall temperature, T_m is the melting temperature of ice and κ_l, ρ_l and μ are the thermal conductivity, density and viscosity of water, respectively. δ is the characteristic water layer thickness. The experiment results using normalized radius (ℓ/R) and time scales (τ_c) are plotted in Figure 19b. The PVC tube data collapses into a single curve, as does the Cu tube data, the two data sets themselves are distinct, indicating that the dominant mechanism is different for the two cases.

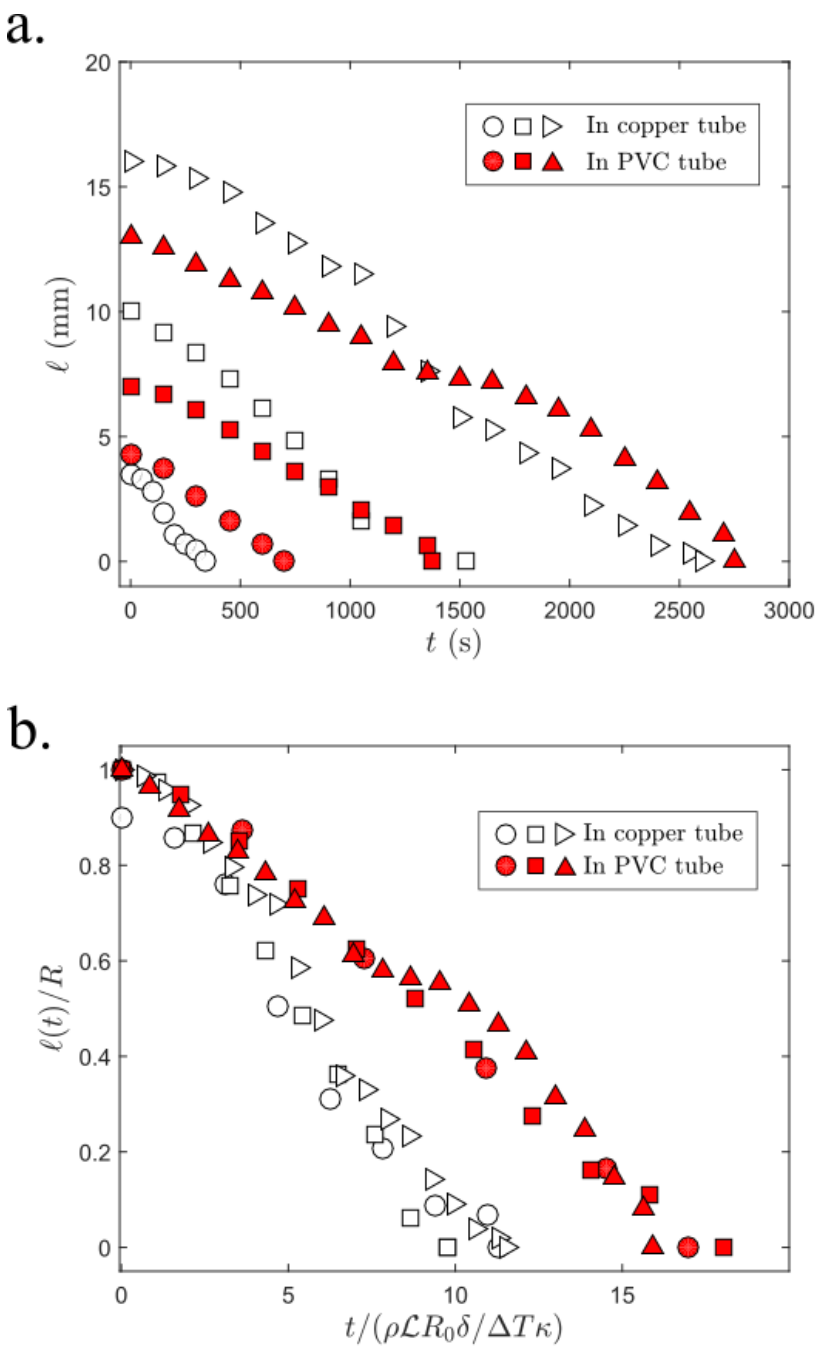

Figure 19. *Results of the ice melting experiments, showing the (a) effective radius of the ice rod, ℓ, as a function of time in copper and PVC tubes, and (b) experiment results normalized by characteristic time from the conduction dominating model.*

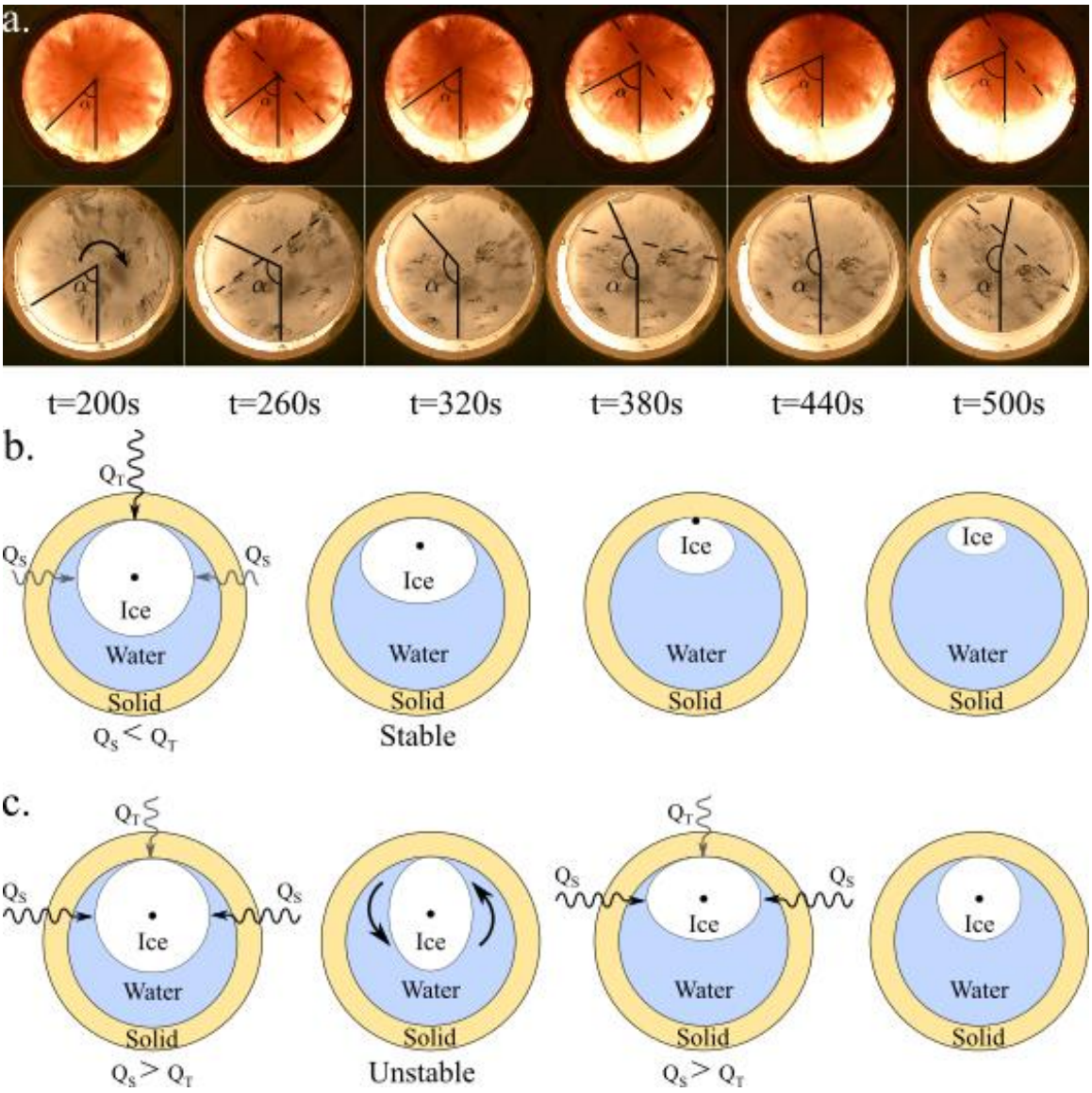

Figure 20. *Rotational motion of ice rod during melting: (a) time elapsed image of ice rod axial angle change inside copper tube (upper row) and PVC tube (lower row) from 200s to 450s. (b) Schematic of melting process when $Q_T > Q_S$, where Q_T and Q_S are the heat flux from the top surface and the heat flux around the sides. (c) Schematic of ice melting process when $Q_T < Q_S$.*

Besides the differences in the ice rod shape and melting time, there are also noticeable differences in the motion of the ice during melting in the two tubes. Figure 20a shows the motion of ice in Cu and PVC tubes during the same time period in the melting

process. The ice rod melting in the Cu tube only wiggles as has been reported in previous studies [24]. The ice rod melting in the PVC tube rotates almost half a circle during the same period. A possible explanation lies in considering melting rate variations in different directions. At the closest contact region at the top of the tube, ice melts mainly by the conductive heat, Q_T, through the thin water layer. In contrast, both sides of the ice rod melt by the convective heat flux, Q_S, due to warmer water flowing downward along the ice surface from the thin top layer (that is itself warmed by the conduction through the tube wall). These warm water streamlines have been visualized by Riviere et al. [24].

When Q_T is larger than Q_S, the top of the ice melts faster, leading to an elliptical shape that is stable to small rotational perturbations as shown Figure 20b. With the top part continuing to melt faster than the sides, the ice rod keeps this elliptical shape till the end. When Q_S is larger than Q_T, the sides melt faster than the top, creating an elliptical shape that is unstable to small rotational perturbations. Thus, the ice rod rolls over to a more stable position in which the major axis of the ellipse is horizontal. Since the sides melt faster, the elliptical shape ends up as a circle and this process starts over again. An exaggerated schematic of this process is shown in Figure 20c. As this process is happening continuously, the continuous rotational motion and the near circular shape of ice rod is observed experimentally.

To analyze this process quantitatively, the convective heat from the top to the sides and bottom of the system is estimated using a correlation proposed by Churchill and Chu [34], and given as:

$$Q_s = \frac{\kappa_l (T_i - T_m)}{2R} (0.6 + \frac{0.387 Ra^{1/6}}{(1 + (0.559/Pr)^{9/16})^{8/27}})^2 \approx 0.15 \kappa_l (\frac{g\beta}{\nu\alpha})^{1/3} (T_i - T_m)^{4/3} \quad (19)$$

where, $Pr = \frac{\nu}{\alpha}$ is the Prandtl number, $Ra = \frac{g\beta}{\nu\alpha}(T_i - T_m)$ is the Rayleigh number, T_m is the melting temperature of ice, ν is the kinematic viscosity of water, β is the thermal expansion coefficient of water and α is the thermal diffusivity of water. The conductive heat transferred through the thin water layer in a copper tube can be estimated from the conduction dominated model [23 33] mentioned previously, as:

$$Q_T = \frac{\rho \mathcal{L} R}{\tau_c} \quad (20)$$

But the conduction dominated model cannot be applied directly to the results from the PVC tube results as shown by the non-convergence of the Cu and PVC tube data shown in Figure 19b. For this case, Q_T is calculated as the total heat transfer through the PVC wall (calculated from the measured temperature difference between inner and outer walls) minus the heat that is transferred downward with the water stream, giving:

$$Q_T = \frac{(T_0 - T_i)\kappa_c}{\ln(R_0/R)R_0} - Q_S \quad (21)$$

The results are shown in Table 4. The ratio Q_T/Q_S, indicates that, in Cu tubes, heat flux from the top, Q_T, is greater than heat flux from the sides, Q_S. In PVC tubes, Q_S is greater than Q_T. As the greater heat flux is the rate controlling driving force, the melting time of ice rods in both tubes can be estimated as,

$$\tau_m = \frac{\rho \mathcal{L} R}{Q_{max}}, Q_{max} = \begin{cases} Q_S, & Q_T/Q_S < 1 \\ Q_T, & Q_T/Q_S > 1 \end{cases} \quad (22)$$

When the melting times are normalized according to Equation 21, the melting time results of PVC tube and copper tube experiments scales with τ_m. Both results collapse on to a single curve, especially before $t/\tau_m = 0.5$ as shown in Figure 21.

Table 4. Table of thermal transport data

Tube Material	$\boldsymbol{R}$ (**mm**)	$\boldsymbol{\kappa_c}$ $(\boldsymbol{W/mK})$	$\boldsymbol{T_i}$ (℃)	$\boldsymbol{Q_T}$ $(\boldsymbol{J/m^2})$	$\boldsymbol{Q_S}$ $(\boldsymbol{J/m^2})$	$\boldsymbol{Q_T/Q_S}$
Copper	3.5	109	4	2785.8	2141.9	1.30
Copper	10	109	3.3	1833.7	1335.8	1.37
Copper	16	109	3.7	1797.0	1473.5	1.22
PVC	4.3	0.19	4	1765.5	2042.5	0.86
PVC	7	0.19	3.4	1246.2	1516.8	0.82
PVC	13	0.19	3.7	707.0	1536.9	0.46

The ice rod morphology and motion is also affected by Q_T/Q_S. For the case of $Q_T/Q_S > 1$, the experimental results in Figure 22 show the ℓ/w plots deviate quickly from $\ell/w = 1$, and follow the $\ell/w = \ell/\sqrt{2R\ell - \ell^2}$ trend which is the largest ℓ/w ratio possible at given ℓ, indicating a 'stable' elliptical shape. For the case of $Q_T/Q_S < 1$, the aspect ratio of the melting ice rod, ℓ/w, stays around 1 with some fluctuation above and below 1 indicating the flipping and rotation motion as a result of an 'unstable' (near circular)

elliptical shape. The rotation motion recorded is plotted as the angle turned throughout the melting process in Figure 23. When $Q_T / Q_S > 1$, ice rod reaches a 'stable' ellipse and does not rotate over $\pi/2$. However, when $Q_T / Q_S < 1$, the ice rod forms an unstable ellipse that rotates over $\pi/2$ and in some cases more than a full circle. These results indicate the competition between the heat fluxes melting the top (conduction) and sides (convection) is a critical factor in determining the melting time and the shape of the ice rod, and its rotation during melting.

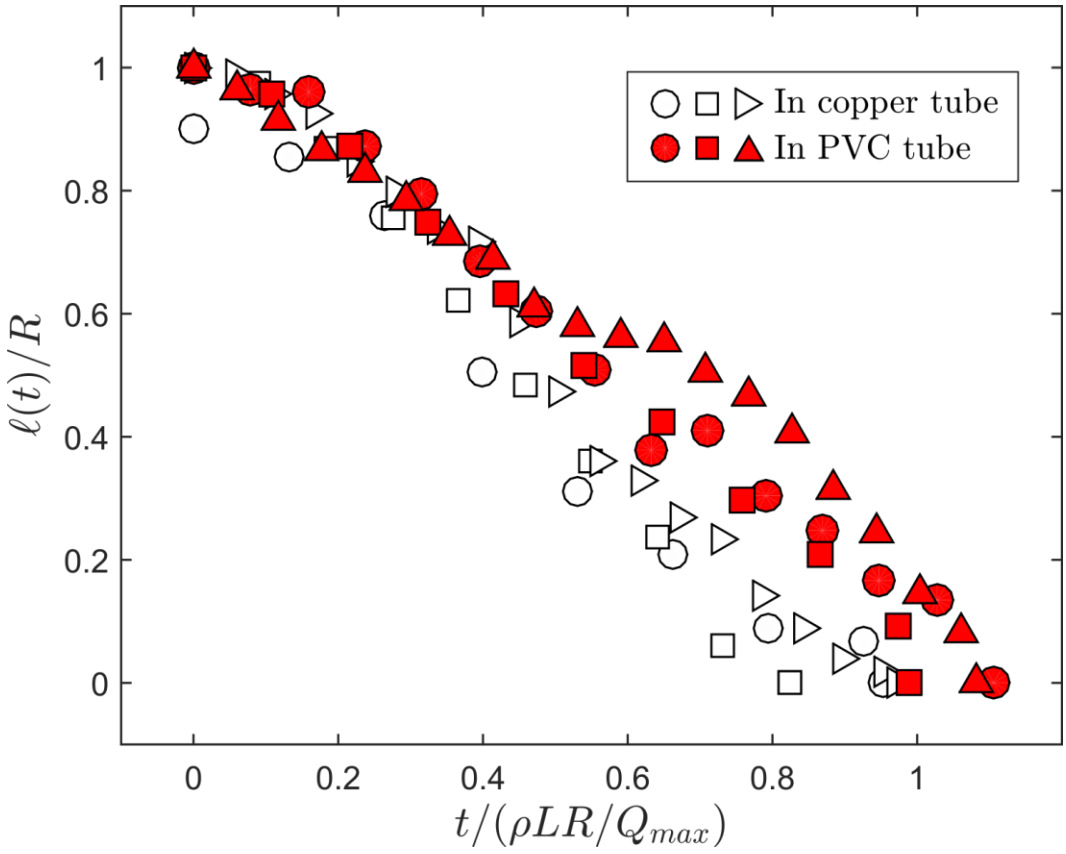

Figure 21. *Time variation of ice rod size normalized by characteristic time scale obtained from Qmax.*

Based on the above analysis, Q_T/Q_S can be quantified as:

$$\frac{Q_T}{Q_S} = \frac{1}{0.03Ra^{1/3}} \frac{\Delta T_o \kappa_c}{\Delta T_i \kappa_l} \tag{23}$$

where $\Delta T_o = T_o - T_i$, $\Delta T_i = T_i - T_m$, Ra is the Rayleigh number ($\frac{g\beta}{\nu\alpha}(T_i - T_m)x^3$), and κ_c and κ_l are the thermal conductivity of the tube wall and the liquid, respectively. Some common phase change applications involving melting in a tube are shown in Figure 24 as a plot of $\frac{\Delta T_o \kappa_c}{\Delta T_i \kappa_l}$ versus Ra. The $Q_T/Q_S = 1$ is shown as a line with a slope of 1/3 in this log-log plot. Areas above this line correspond to $Q_T/Q_S > 1$, while areas below this line correspond to $Q_T/Q_S < 1$.

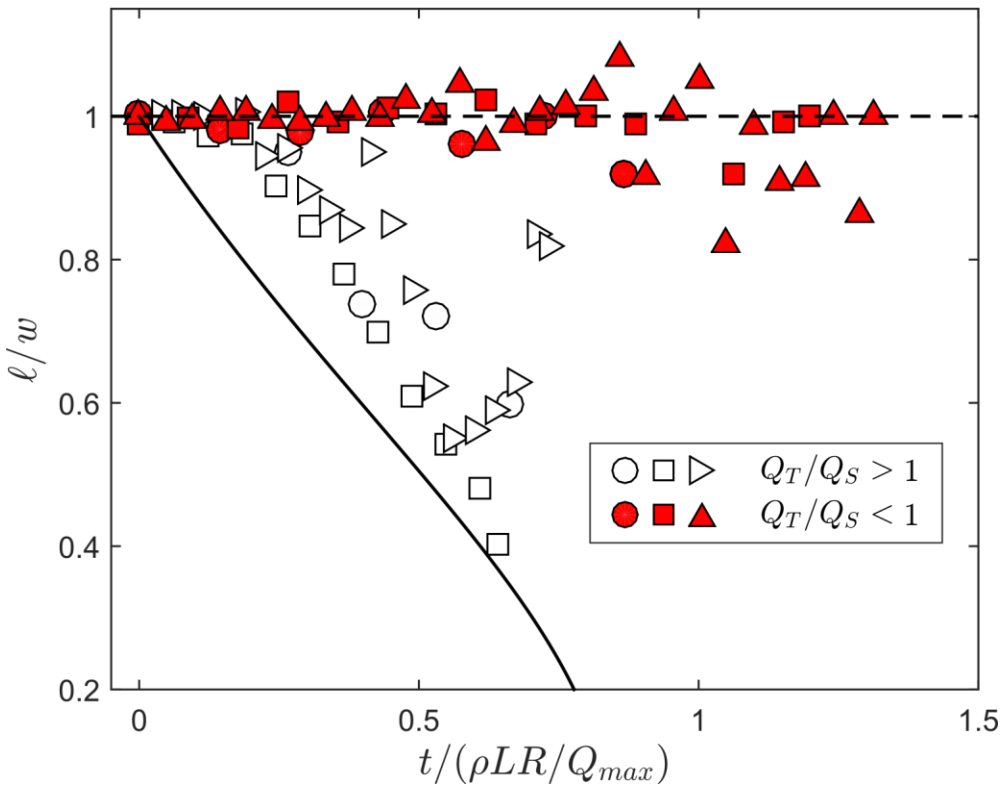

Figure 22. *Variation of the aspect ratio, ℓ/w,* over time in Cu and PVC tubes.

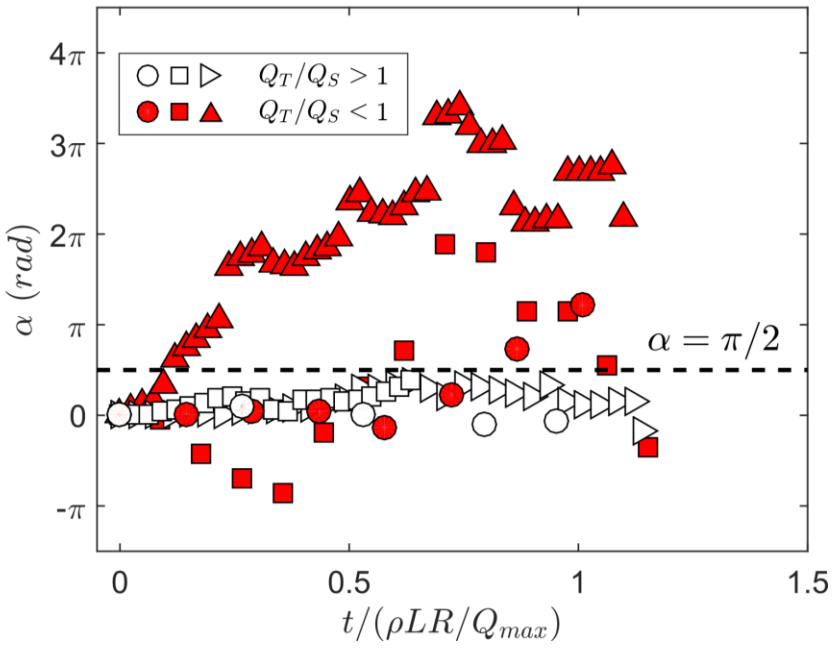

Figure 23. *Variation of ice rod axial angles in Cu and PVC tubes over time.*

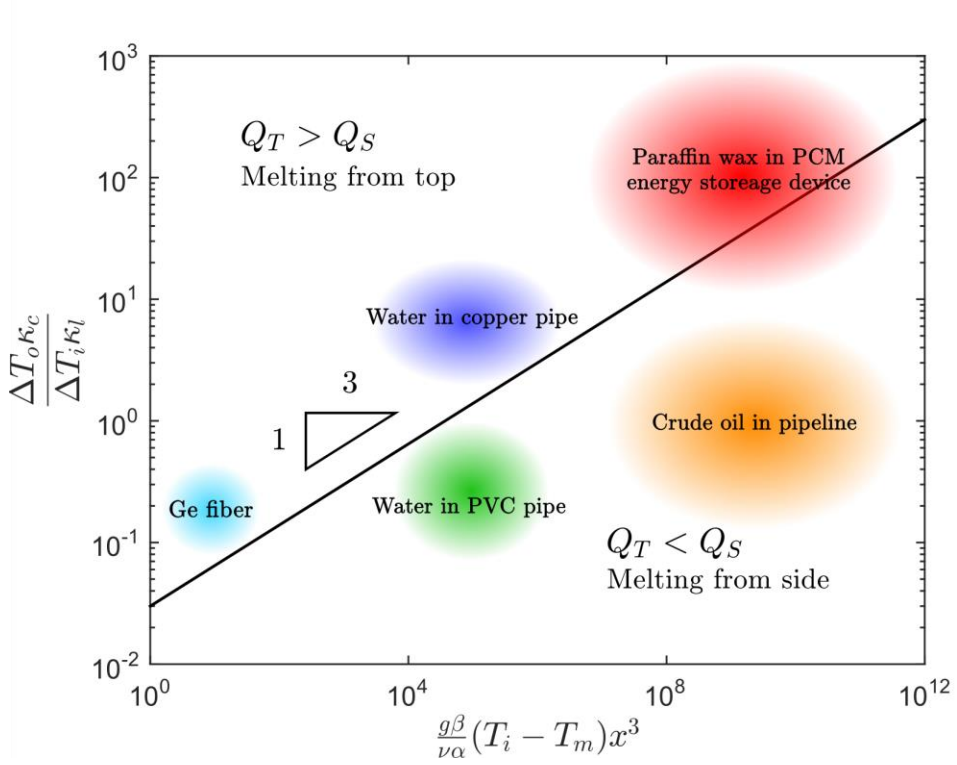

Figure 24. *Q_T and Q_S ratio distribution in various applications in a plot of Ra vs.* $\frac{\Delta T_o \kappa_c}{\Delta T_i \kappa_l}$.

The plot shows that water in metal pipeline has the same *Ra* as that in plastic tube, but because of the high thermal conductivity κ_c of the metal wall, it falls in the $Q_T/Q_S > 1$ regime, while water in a plastic tube falls on the other side due to the low κ_c value. For crude oil in a pipeline, the large pipe diameter leads to a large value of *Ra*. For this case, even with a steel pipe, the phase change will be Q_S dominated. In a semiconductor core fiber, the very small diameter (in the μm range) leads to a small value of *Ra*. However, since the thermal conductivity of semiconductor κ_l is much greater than that of glass cladding κ_c, it falls in the $Q_T/Q_S > 1$ regime, indicating that the dominating heat transfer mechanism in core melting in the fiber during post processing process is heat conduction. Finally, melting of paraffin wax, a commonly used PCM in energy storage devices can be moved from convection dominated to the preferred conduction dominated melting by decreasing the diameter of the tube encasing the wax (decreasing *Ra*), or by increasing the tube wall thermal conductivity. Approaches studied to achieve this have included use of mini-capsules for PCM [35] and installing fins on the tube wall [36].

2.3 Conclusions

A novel germanium-core borosilicate clad optical fiber for mid-infrared transmission was successfully fabrication using the ‘rod-in-tube’ method. The neck formation process of the fiber preform during the drawing process was modeled by coupling the ‘Toutron’ model with a 2D heat transfer model. The predicted neck formation location and formation time was found to be in good agreement with the experimental data. The results provide the guidance for the accurately positioning of semiconductor core in the preform, which ultimately lead to the lowest reported transmission loss for Ge-core borosilicate cladded fibers made by this method. The optical characterization shows the transmission of mid-infrared through the fiber with relatively high loss. The electron microscopy characterization on the fiber materials indicates that germanium core shows high crystallinity and minimal light element diffusion. Although grain boundaries did exist in the Ge-core, they were found to be predominantly twin boundaries.

The heat transfer in the semiconductor core fiber during annealing-based post processing was studied using a proxy of ice melting in cylindrical containers. It was found that the melting time is scaled to the dominating heat transfer mechanism in the system. The heat transfer from the top and the heat transfer from the side are two competing mechanism. The ratio between them is found to depend on both the Rayleigh number of the fluid and the thermal conductivity of the wall. This result can also be applied to guide the design of phase change materials for energy storage.

3. Yttria Stabilized Zirconia Stability in Silicon Solid Oxide Membrane Electrolysis

3.1 Introduction

Solid Oxide Membrane (SOM) based electrolysis process can produce high purity metals from their oxides efficiently and in an environmental friendly manner [37]. Several high value metals including Mg [38-42], Si [43 44], Al [45] and Ta [46] have been successfully produced through SOM electrolysis. Thus, SOM electrolysis is a potential alternative route of producing solar grade silicon that can overcome some of the challenges of the currently used Siemens method, that is energy and cost intensive and also produces environmentally harmful byproducts [47].

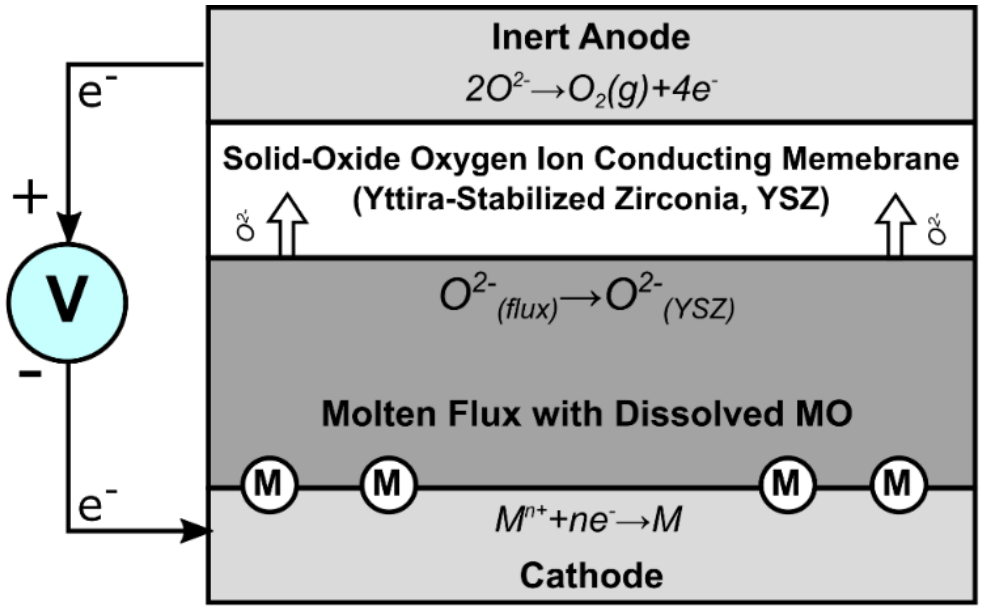

Figure 25. *Schematic of SOM process for metal production.*

Figure 25 shows the working principle of the SOM electrolysis process. A potential that is higher than the disassociation potential of a metal oxide that is dissolved in a molten flux is applied between the electrodes. This causes the metal cations to migrate to the

cathode where they are reduced to metal, while the oxygen anions migrate through the YSZ membrane to the anode where they are oxidized to oxygen gas.

3.1.1 Silicon SOM process

To produce silicon from silica using SOM electrolysis, silica is dissolved in a molten oxyfluoride flux at elevated temperatures (1100-1300°C). Figure 26 shows the schematic of the SOM assembly used in this study. The cathode is made of a silicon plate connected to a graphite rod current collector, which responds to the applied potential by plating silicon onto itself. The anode is made of inert materials that does not react with oxygen, and it is separated from the molten flux by the YSZ (SOM) tube. When the oxygen anions reach the silver pool in the YSZ tube, they are oxidized into oxygen gas, which is isolated from the flux and the cathode and then removed from the system though the YSZ tube outlet. To overcome the mass transfer limitation of silica in the flux, the flux is mechanically agitated by bubbling forming gas (95% Ar and 5% H_2) into the flux through a molybdenum tube.[5]

[5] Apparatus designed by Dr. Thomas Villalon Jr.

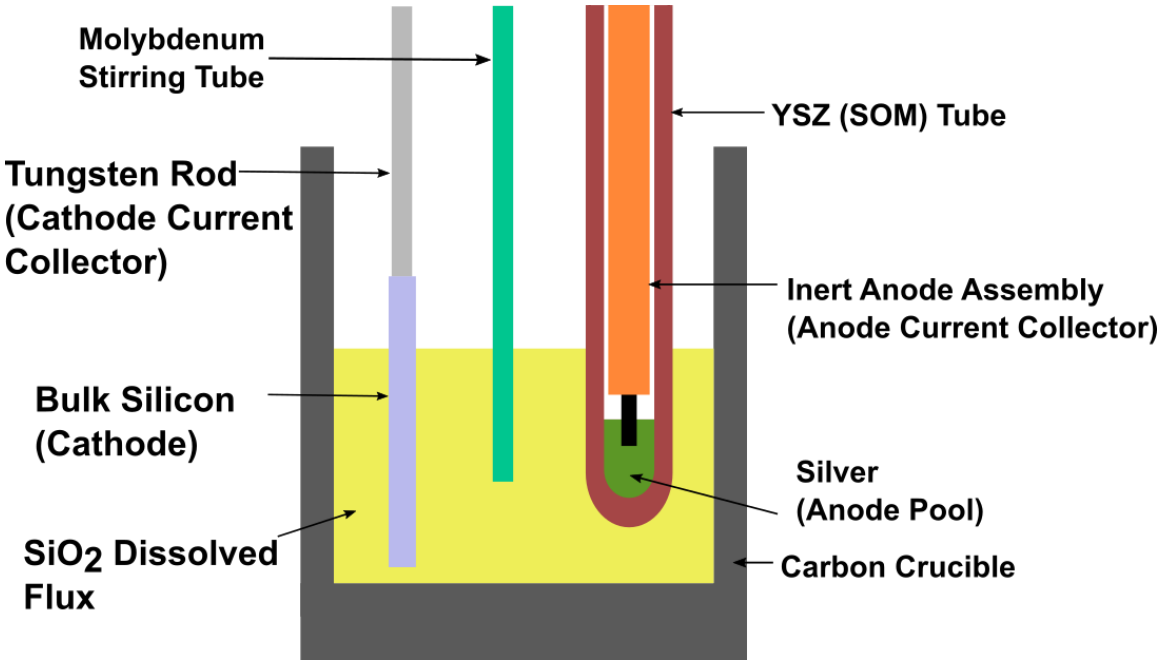

Figure 26. *The schematic of Si-SOM electrolysis assembly.*

3.1.2 YSZ degradation in flux

In a previous study, silica dissolved in a eutectic BaF_2-MgF_2 melt was found to chemically attack the partially yttria stabilized zirconia (6 mol% Y_2O_3, pYSZ) ceramic membrane, even in the absence of an applied electric potential [44]. This attack caused yttria depletion from YSZ grains, which led to their phase transformation to tetragonal yttria stabilized zirconia (tYSZ) at the operating temperature (1100ºC). Upon cooling, the tYSZ underwent a tetragonal to monoclinic phase transformation accompanied by a volume change, which led to cracking of the YSZ membrane. This YSZ phase transformation pathway is shown on the Y_2O_3 – ZrO_2 phase diagram in Figure 27. It was also found that increasing the silica content in the flux accelerated the attack while the

addition of YF_3 to the flux retarded the attack on the YSZ membrane. Finally, a flux with 2 wt% SiO_2, 15 wt% YF_3 and a balance of eutectic BaF_2-MgF_2 was used to successfully produce Si without any attack on the YSZ membrane. However, even though the production of Si was demonstrated, several issues remained, including the presence of potentially harmful Ba^{2+} cations [48], the requirement of a very high YF_3 content in the flux (15 wt%), and the relatively low SiO_2 content in the flux (2 wt%) which causes higher concentration polarization losses and lower energy efficiency.

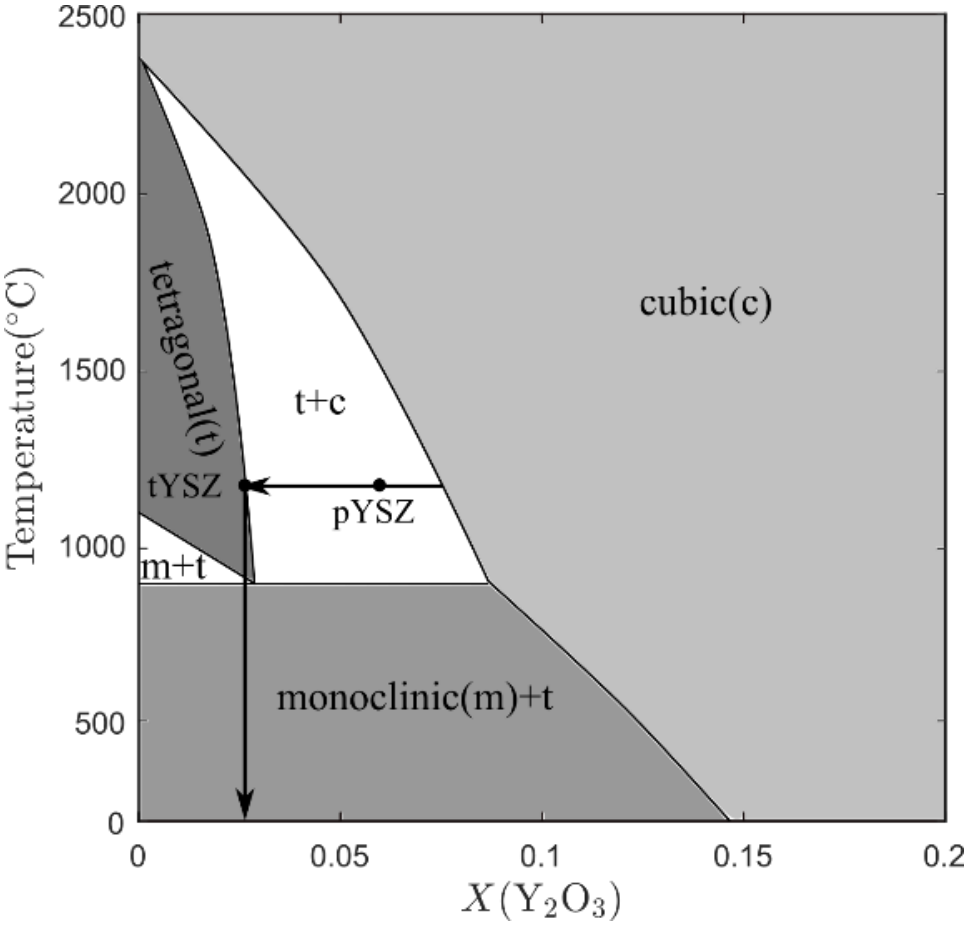

Figure 27. *ZrO_2–Y_2O_3 phase diagram and proposed path of yttria depletion in YSZ (reconstructed from Reference [49]).*

In previous research on aluminum production from SOM electrolysis of alumina dissolved in a molten fluoride flux, Su et al. [45] pointed out that oxides like Al_2O_3 in the molten flux corrode the YSZ membrane because alumina has a lower optical basicity compared to the YSZ ceramic. When oxides with higher optical basicity, such as CaO, were added to the flux, the CaO neutralized the Al_2O_3 containing flux and retarded the corrosion of YSZ. However, the relationship between the optical basicity of the flux and the YSZ corrosion was not fully explored or explained in that study.

3.1.3 Optical Basicity

The acid-base reactions between oxides in the molten state at high temperatures is extensively studied in several important processes, such as in the production of iron and steel [50], and in glass making [51]. An oxide with lower basicity acts as an oxygen ion acceptor, while an oxide with higher basicity acts as an oxygen donor. Several acid-base theories have been proposed to explain the reactions of molten oxides, such as the Lux-Flood theory [52 53]. However, there are limitations when describing a system with multiple oxides with different basicity. Empirical coefficients were used, which is not satisfactory from the chemical point of view. Duffy proposed the concept of the optical basicity of an oxide as an effective measurement of the acidity/basicity of the oxide at its molten state [51 54]. To measure the optical basicity of an oxide, the ultraviolet spectrum of a ‘probe ion’ is used to determine the negative charge borne by the oxygen atoms. The optical basicity of an oxide, Λ, can be obtained from the 6s-6p ultraviolet absorption

frequency, ν, using the following equation:

$$\Lambda = \frac{60700cm^{-1} - \nu}{31000cm^{-1}} \tag{24}$$

By definition, the optical basicity of CaO, Λ = 1.0. For a system with multiple oxides, its optical basicity can be calculated using the following equation.

$$\Lambda = \frac{\sum X_1 n_1 \Lambda_{th,1} + X_2 n_2 \Lambda_{th,2} + \cdots}{\sum X_1 n_1 + X_2 n_2 + \cdots} \tag{25}$$

where, Λ is the optical basicity of the system, and $\Lambda_{th,i}$, X_i, and n_i are the optical basicity, mole fraction, and the oxidation state of the ith oxide in the mixture, respectively. With the optical basicity of values of the flux, the propensity for acid-base reactions between a molten flux in contact with oxides can be predicted.

3.2 Experimental Details

3.2.1 Experimental Design

Since BaF_2 in the BaF_2 – MgF_2 eutectic flux is potentially harmful, it was replaced in this study by a relatively benign CaF_2 –MgF_2 eutectic which also has a similar low melting eutectic (974°C) [55]. In addition, since the SiO_2-CaO-CaF_2 system is well known to form liquid oxy-fluoride over a wide range of compositions [56], the chosen flux composition was able to dissolve up to 7.7 wt% SiO_2 and 9 wt% CaO. It is known that the yttrium ion activity difference between the YSZ membrane and the molten flux contributes to its diffusion from the YSZ to the flux [57]. In this study, 4 wt% YF_3 was added to the

flux to reduce this difference in yttrium ion activity. To design fluxes to analyze the correlation between flux optical basicity and YSZ corrosion, it is necessary to understand the relation between flux oxide optical basicity and flux composition. The flux optical basicity can be estimated using Duffy's optical basicity model for multiple oxides system mentioned above. In this case, the optical basicity of the molten flux can be calculated as:

$$\Lambda = \frac{X_{CaO} n_{CaO} \Lambda_{CaO} + X_{SiO_2} n_{SiO_2} \Lambda_{SiO_2}}{X_{CaO} n_{CaO} + X_{SiO_2} n_{SiO_2}} \tag{26}$$

Table 5. Optical basicity and cation oxidation state of oxides

Oxide	CaO	SiO_2	Y_2O_3	ZrO_2
Optical Basicity (Λ)	1.0 [54]	0.48 [54]	0.72 [58]	0.71 [58]
Cation Oxidation State (n)	+2	+4	+3	+4

Table 5 lists the optical basicity and oxidation of the relevant oxides in this study. By taking the optical basicity and cation oxidation state values of CaO and SiO_2 into the equation, Equation 26 can be further simplified to a function of the ratio of mole fractions of CaO and SiO_2, as:

$$\Lambda = \frac{(\frac{X_{CaO}}{X_{SiO_2}}) n_{CaO} \Lambda_{CaO} + n_{SiO_2} \Lambda_{SiO_2}}{(\frac{X_{CaO}}{X_{SiO_2}}) n_{CaO} + n_{SiO_2}} = \frac{\left(\frac{X_{CaO}}{X_{SiO_2}}\right) + 0.96}{\left(\frac{X_{CaO}}{X_{SiO_2}}\right) + 2} \tag{27}$$

Two groups of fluxes were designed to examine the effects of flux oxide content on flux optical basicity and YSZ degradation. Fluxes in the first group contained a constant SiO_2 content of 5 wt% with CaO contents ranging from 0 wt% to 9 wt%. Fluxes in the

second group contain a constant CaO content of 9 wt% and SiO_2 contents ranging from 5 wt% to 7.7 wt%. The detailed composition and optical basicity of each tested flux is listed in Table 6.

Table 6. Composition and optical basicity of tested flux

Composition (wt%)	**Group 1** Constant SiO_2 varying CaO				**Group 2** Constant CaO varying SiO_2			
CaO	0	3.6	7.5	9	9	9	9	9
SiO_2	5	5	5	5	5	5.4	6.7	7.7
YF_3	4	4	4	4	4	4	4	4
CaF_2	50.2	48.2	46.1	45.3	45.3	45	44.3	43.8
MgF_2	40.8	39.1	37.4	36.7	36.7	36.6	36	35.5
Optical basicity (Λ)	0.48	0.625	0.71	0.735	0.735	0.725	0.70	0.68

3.2.2 Experimental Process

All chemicals used in this study were purchased from Alfa-Aesar (Ward Hill, MA). Before mixing, the chemicals were heated to and held at 450ºC for 8 hours in ceramic crucibles to remove any water. Eutectic CaF_2-MgF_2 mixtures were heated in carbon crucibles to 1150°C under forming gas (95% Ar and 5% H_2) and held in the molten state for 2 hours before cooling to room temperature. Residual carbon deposits on the solidified CaF_2-MgF_2 eutectic from the crucible was mechanically removed. The eutectic fluorides were then crushed and mixed with the desired amount of oxides and YF_3 for a total mass of 60g. This mixture of oxides and fluorides was then heated in a cylindrical 304 stainless steel crucible with a 41.15 mm (1.62 in) inner diameter under forming gas atmosphere to

1150°C and held in the molten state for 2h before cooling to room temperature. YSZ containing 6 mol% Y_2O_3 (which will hereon be referred to as 6YSZ) tubes with a 19.05 mm (0.75 in) outer diameter and a 14.22 mm (0.56 in) inner diameter (McDanel Advanced Ceramic Technology, Beaver Falls, PA) were cut into approximate 0.4 cm long rings, each weighing around 4g.

The high temperature annealing process to test the chemical stability of YSZ in molten flux is shown in Figure 28. The 6YSZ ring was first placed on top of the solidified pre-selected flux in the stainless steel crucibles at room temperature. One YSZ ring sample was used for each flux composition. The crucible containing the flux (including fluorides and oxides) and the ring was weighed before it was heated to 1200°C with a ramp rate of 6°C/min and held at 1200°C for 24h under forming gas atmosphere. Due to density differences between the liquid flux and the 6YSZ, the 6YSZ ring sank to the bottom of the crucible and was completely immersed in the flux. After 24h, the system was cooled to room temperature at a rate of 6°C/min after which the crucible containing the flux and the YSZ ring was weighed again. The difference in the weights of the crucible before and after the 24h hold at 1200°C under the forming gas atmosphere that the flux is exposed to in an actual SOM electrolysis experiment was attributed to the volatilization of the flux. Thus, the weight loss of the flux was a measure of the stability of the flux under SOM electrolysis operating conditions.

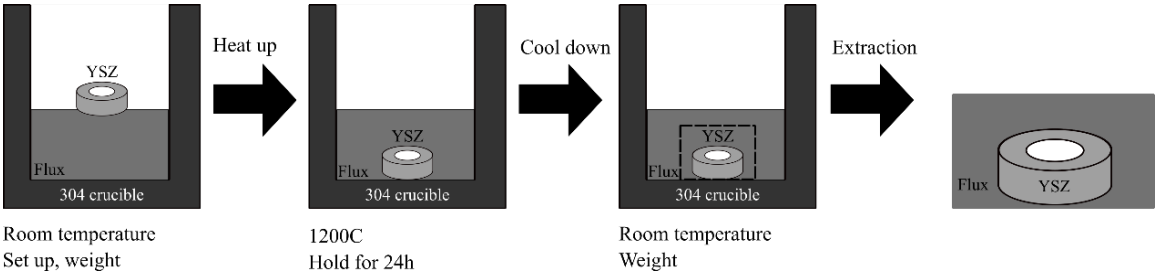

Figure 28. *Schematic of the annealing process of YSZ in molten flux.*

The 6YSZ ring together with the flux were taken out from the steel crucibles and mounted in epoxy. Mounted samples were polished using diamond abrasives down to a 0.05 μm finish for microstructural analysis. Scanning electron microscopy (SEM) and Energy-dispersive X-ray spectroscopy (EDX) analyses are performed using a Zeiss Supra 55 SEM (Carl Zeiss, Oberkochen, Germany) equipped with Genesis EDX detector (EDAX, Inc., Mahwah, NJ). Transmission electron microscopy (TEM) analysis was performed (Tecnai Osiris, FEI, Hillsboro, Oregon) on electron transparent samples prepared by the 'lift-out' method using a Focused Ion Beam instrument (Quanta 3D FEG, FEI, Hillsboro, Oregon).

3.3 Results

3.3.1 Volatility

To track the volatility of the fluxes tested, the mass of the samples before and after the 24h hold at 1200°C were recorded. The volatility was calculated using the following equation,

$$Volatility = \frac{\Delta m}{A \cdot t} \tag{28}$$

where Δm is the mass loss of the sample, A is cross section area of the crucible and t is the duration of the high temperature hold. The mass loss and the corresponding volatility of the different flux samples are listed in Table 7. The table shows that in general, the addition of CaO decreases the volatility of the flux while the addition of SiO_2 increase the flux volatility. During the stability test of fluxes with constant silica content, the mass loss and calculated volatility remains almost unchanged for flux with 0wt% CaO and 3.6wt% CaO, but it decreases significantly when CaO content reaches 7.5wt%. For the samples tested in flux with constant CaO content, the volatility increases with the SiO_2 content, increasing from 5wt% to 7.7wt%.

Table 7. Mass loss and volatility of different fluxes

Group	**Group 1 Constant SiO_2 varying CaO**				**Group 2 Constant CaO varying SiO_2**			
CaO/SiO_2 Content (wt%/wt%)	0/5	3.6/5	7.5/5	9/5	9/5	9/5.4	9/6.7	9/7.7
Mass Loss (g)	0.467	0.504	0.035	0	0	0.34	0.347	1.058
Volatility ($\frac{\mu g}{cm^2 \cdot s}$)	0.407	0.439	0.030	0	0	0.296	0.302	0.921

3.3.2 YSZ degradation

An SEM micrograph of a polished cross-section of the 6YSZ membrane tested in the flux containing 5wt% SiO_2 and 0wt% CaO is shown in Figure 29a. In the YSZ region close to the YSZ/flux interface, there is a layer exhibiting a different contrast compared to the bulk 6YSZ. The yttrium concentration profile obtained through an EDX line-scan across this interface region is overlaid in Figure 29a. The figure shows a clear decrease in

yttrium content from the bulk 6YSZ to ~ 2at% in this layer. This layer is the yttria depletion layer (YDL) as described in a previous study [44]. A higher magnification SEM micrograph of the YDL, shown in Figure 29b, clearly shows that the YSZ grains in YDL region have been attacked by the flux. The EDX spectrum of this region (shown by a box in Figure 29b) is shown in Figure 29c. The EDX spectrum confirms the presence of the flux components, i.e., Ca, Mg, F and Si, in the YDL region of the 6YSZ membrane.

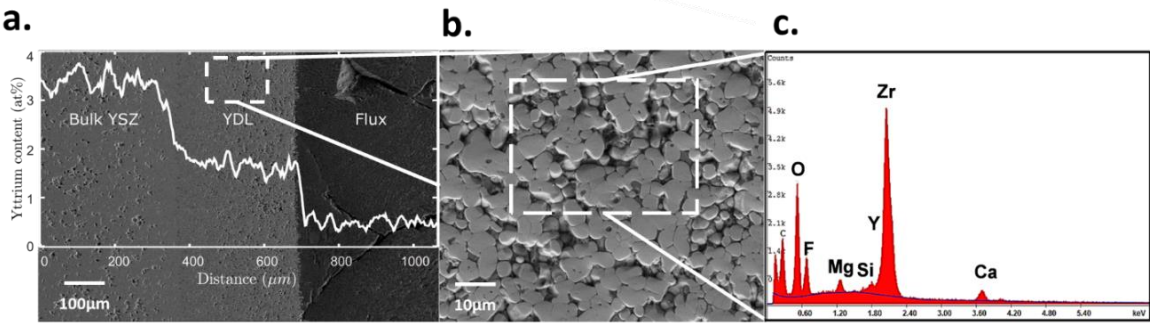

***Figure 29**. (a) SEM micrograph of YSZ and flux (5wt% SiO_2, 0wt% CaO) interface, with overlaid Y concentration profile showing Y depletion in the YDL. (b) SEM micrograph of the YDL at a higher magnification. (c) The EDX spectrum of the selected region in (b).*

In order to isolate the location of the flux components in the YDL, EDX-based elemental dot maps were obtained in the YDL, and the results are shown in Figure 30. The figure shows that Ca, Mg and F accumulate in the triple grain junctions of YSZ. This suggests that the flux has penetrated in the YDL, presumably by attacking the grain boundaries, and has accumulated at the triple grain junctions. These results are consistent in all samples in which a YDL is formed as a result of the presence of silica in the flux.

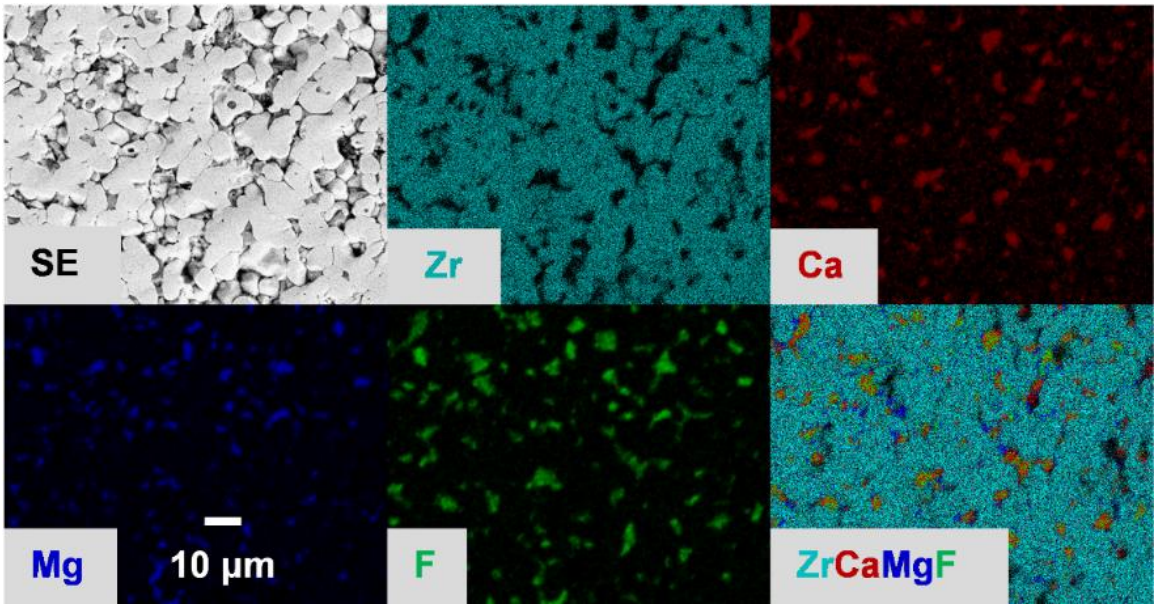

Figure 30. *SEM micrograph of a portion of the yttria deleted layer and the corresponding EDX dot maps of Zr, Ca, Mg, F, and an overlay of all the elemental dot maps.*

To study the grain boundary attack in more detail, TEM studies (in the STEM mode) were carried out on an electron transparent sample from the YDL region of a YSZ membrane exposed to a flux containing 5wt% SiO_2 and 0wt% CaO. Figure 31a shows a bright-field STEM image of three YSZ grains (dark grey contrast) around a triple junction in the YDL. The brighter regions around the grains represent the flux, which itself appears to have phase separated upon cooling to room temperature. A grain boundary between two grains is visible on the lower left of the micrograph. A high angle annular dark-field (HAADF) micrograph and EDX-based elemental dot maps of a region marked by a rectangle in Figure 31a are shown in Figure 31b. Clearly, the flux has separated into MgF and CaF phases at room temperature. Interestingly, the silica in the phase-separated flux is confined mostly to the MgF phase at room temperature.

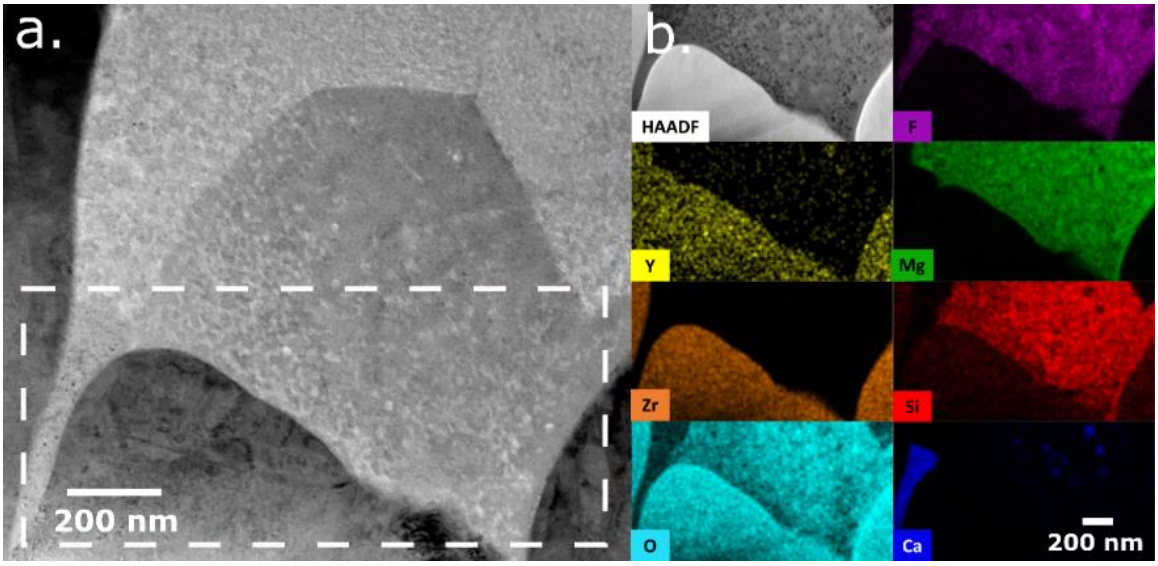

Figure 31. *(a) Bright filed (BF) STEM image, and (b) high-angle annular dark-field (HAADF) image and elemental dot maps of F, Y, Mg, Zr, Si, O, and Ca of YSZ grains and flux accumulated at a triple grain junction in the YDL.*

Quantitative EDX analysis was performed on the several YSZ grains inside the YDL, and an example is shown in Figure 32, which shows that the Y content was somewhat uniform across the grain but was depleted from the original value of 3.8at% in 6YSZ to around 2at%. This value is closer to the yttria solubility limit of tYSZ at 1200ºC (which is 2 mol% Y_2O_3 or 2YSZ according to the ZrO_2-$Y2O_3$ phase diagram [49 59]). This observation is in agreement with the Y profile in Figure 29a. Xu et al. also reported that 6YSZ grains can lose yttria and become 2YSZ in the YDL region when attacked by a silica containing flux [44].

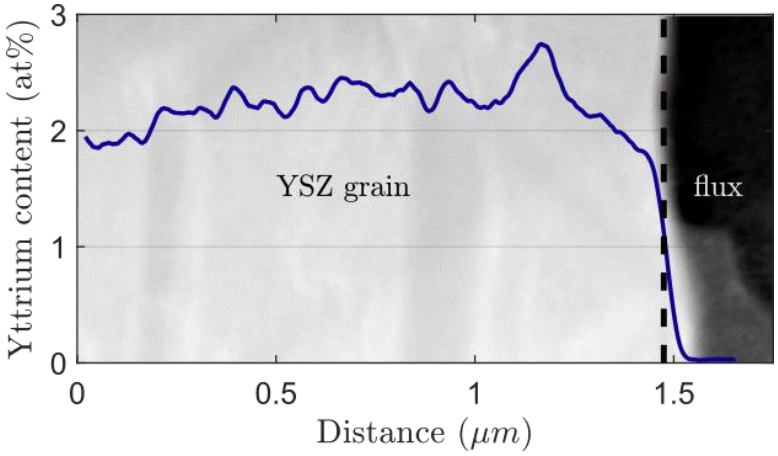

Figure 32. *Yttrium content profile from the center of a YSZ grain in the YDL to the grain boundary where flux has penetrated.*

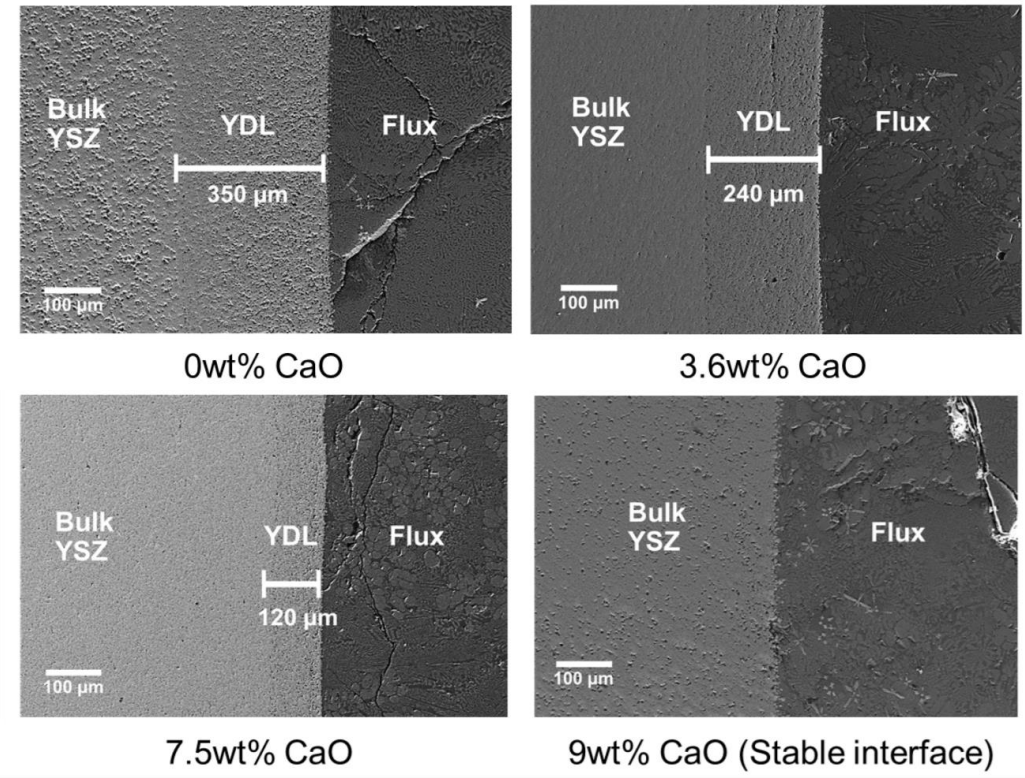

Figure 33. *SEM micrographs of YSZ and flux interface of samples in Group 1.*

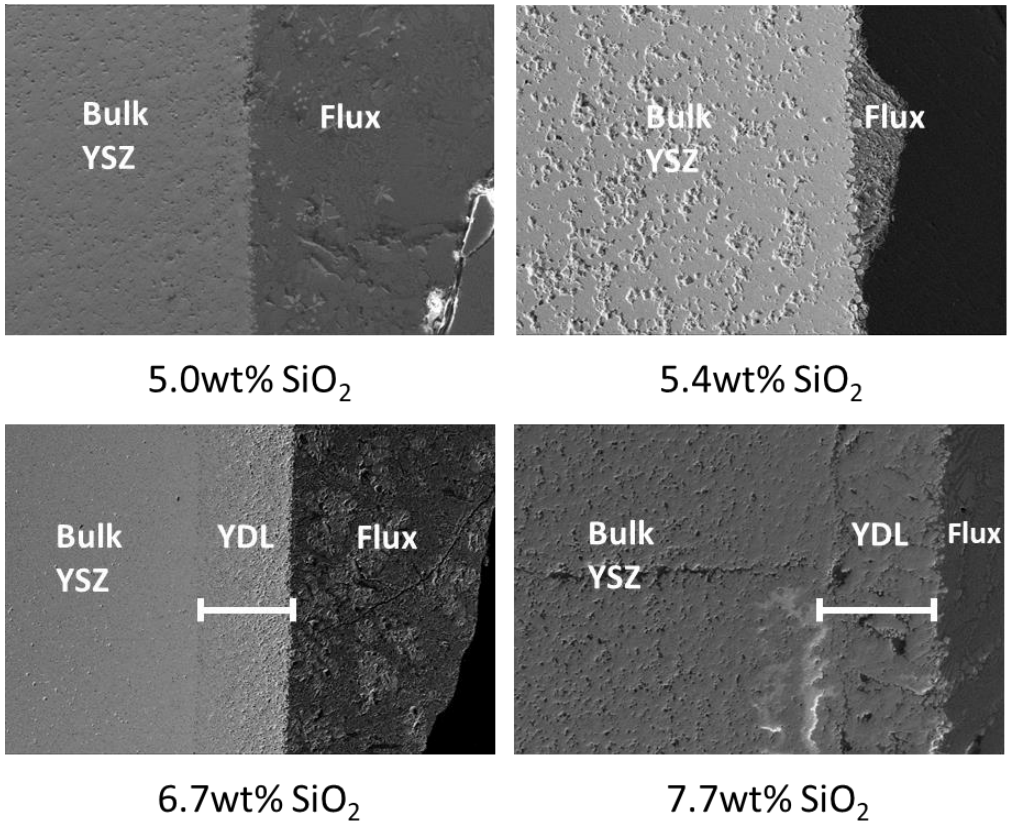

Figure 34. *SEM micrographs of YSZ and flux interfaces of samples in Group2.*

SEM images of the interfaces between the flux and the YSZ membrane of all the samples tested are shown in Figure 33 and Figure 34. In addition, SEM-based EDX line scans were taken across the YSZ flux interface to identify the composition and thickness of the YDL in all the samples tested, and the Y concentration profiles of all two groups of samples are plotted in Figure 35. In each case, the yttrium content decreased from ~ 4 at% in the bulk (unattacked) YSZ to around 2 at% in the YDL. The thickness of the 2 at% region at the YSZ/flux interface is the YDL thickness. Figure 33 and Figure 35a show that for Group 1 samples exposed to fluxes containing 5wt% SiO_2, the YDL thickness decreased as the CaO content in the flux increased and essentially reached 0 at 9wt% CaO.

Figure 34 and Figure 35b show that, for Group 2 samples exposed to fluxes containing 9wt% CaO, the YDL does not form until the SiO_2 content in the flux reached 6.7wt%, after which the YDL thickness increased with increasing SiO_2 content.

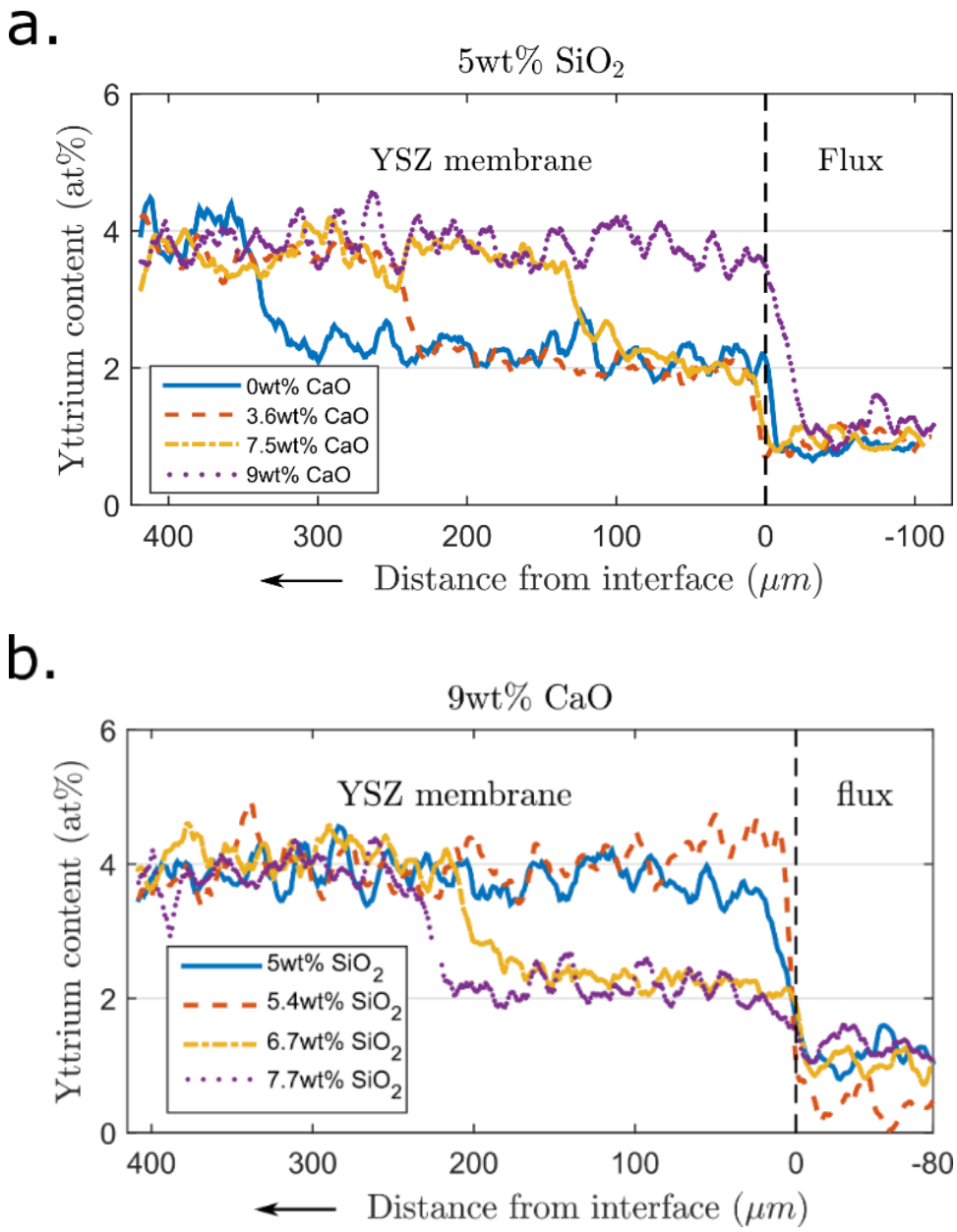

Figure 35. *Yttrium content profile across the YSZ membrane and flux interface for (a) Group 1 (constant 5wt% SiO_2, varying CaO content), and (b) Group 2 (constant 9wt% CaO, varying SiO_2, content).*

3.4 Discussion

3.4.1 Volatility

Volatility data (Table 7) of Group 1 fluxes (constant SiO_2 content) shows that the volatility of the flux generally decreases as the amount of CaO increases in the flux, while the data for Group 2 fluxes (constant CaO content) shows that the volatility increases with increasing silica content in the flux. Since all the chemicals used in the experiments were properly dried in advance, the mass loss of the flux is mainly attributed to the formation and loss of SiF_4 according to the following reaction between SiO_2 and CaF_2 [56 60]:

$$SiO_2 + 2CaF_2 \rightleftharpoons 2CaO + SiF_4(g) \tag{29}$$

This reaction is highly undesirable, because it not only generates toxic SiF_4 gas, but also causes Si to leave the system, thereby reducing the SOM electrolysis efficiency. The partial pressure of SiF_4, p_{SiF_4}, can be written as:

$$p_{SiF_4} = \frac{a_{SiO_2} a_{CaF_2}^2 K_{eq}}{a_{CaO}^2} \tag{30}$$

where a_{SiO2}, a_{CaF2} and a_{CaO} are the activities of SiO_2, CaF_2 and CaO, respectively, in the flux. Increasing the CaO concentration in the flux increases a_{CaO}, thereby reducing p_{SiF4}, leading to a reduction in mass loss as SiF_4 and accompanying loss of Si from the flux. Conversely, increasing the silica content of the flux increases a_{SiO2}, thereby increasing p_{SiF4}, leading to a larger mass loss.

3.4.2 YSZ degradation mechanism

3.4.2.1 The Effect of flux optical basicity

The experimental results clearly show that the addition of SiO_2 in the flux enhances YSZ degradation, while the addition of CaO mitigates it. It has been shown in previous studies that silica can cause the segregation of yttria to the grain boundaries in the YSZ membranes [61 62] and the formation of a glassy silica phase at the YSZ grain boundaries [61 63-65]. De Wet et al. reported that the acidity of silica causes the grain boundary attack on YSZ grains in their study of interaction between sand and YSZ thermal barrier coatings [65]. According to the Duffy's optical basicity theory [54], the optical basicity of an oxide is a measure of its tendency to release oxygen anions (electron pairs) when interacting with other oxides. The optical basicity, Λ, of SiO_2 is 0.48, which is very acidic compared to both ZrO_2 (Λ=0.71) and Y_2O_3 (Λ=0.72) [58]. Therefore, SiO_2 tends to attract the oxygen from both oxides in the YSZ and preferably from Y_2O_3. However, experimentally, the zirconia in the YSZ remains intact upon exposure to the flux, while the yttria does not. There may be two explanations for this phenomenon. Although the optical basicity of ZrO_2 (Λ=0.71) is very close to that of yttria, the ZrO_2 is considered to be a network former when its cation coordination number is 6 and an intermediate oxide when its cation coordination number is 8 [65-67]. Since the zirconia used in this study is doped with 6 mol% yttria, the majority of Zr cations have a coordination number of 8. As a result, the ZrO_2 in the YSZ acts as weak oxygen acceptor/intermediate oxide, in comparison to Y_2O_3, which acts as an oxygen donor. Therefore, yttria loses oxygen anions to silica while the ZrO_2 in the YSZ remains intact after exposure to the silica containing flux at high temperature. An alternate

explanation may be related to the difference in Y^{3+} and Zr^{4+} solubility in the melt when in equilibrium with the YSZ phase. A significant lower solubility of Zr^{4+} can also explain this observation.

In the molten flux, the SiO_2 molecules form a silica network featuring $(SiO_4)^{-4}$ tetrahedral connected by 'bridging' oxygen atoms, making Si a strong oxygen acceptor as well as a network former [54 68]. Since yttria has a higher optical basicity than SiO_2 and it is known to be a network modifier to SiO_2 [69 70], it acts as an oxygen donor to the silica network. The O^{2-} ions from Y_2O_3 breaks the silica network by turning the 'bridging' oxygens into 'non-bridging' oxygens as [54 68 71]:

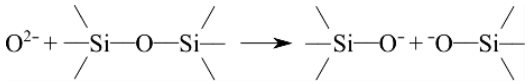

(31)

Grain boundaries being are high-energy interfaces are locations where the silica in the molten flux preferentially attacks by removing O^{2-} ions from Y_2O_3. At the same time, free Y^{3+} ions at the YSZ grain boundaries are incorporated into the molten flux. This process is shown schematically in Figure 36a. This attack on the grain boundaries of the YSZ membrane leads to the penetration of flux into the YSZ through the grain boundaries, as shown in Figure 30 and Figure 31.

The preferential removal of yttria from the YSZ grain boundary also causes an yttria concentration gradient between the center of the YSZ grains and the attacked grain boundaries as shown in Figure 36b. This concentration gradient drives the yttria diffusion from the center of the grain to the grain boundary. While yttria being consumed at the grain boundary by the silica network breaking reaction, the yttria diffusion continues in the bulk

of the grain until the entire YSZ grain loses yttria and transforms into tetragonal YSZ (2YSZ) as shown in Figure 36c. The uniform yttrium concentration profile from the center to the edge of the YSZ grain (Figure 32) supports this assumption.

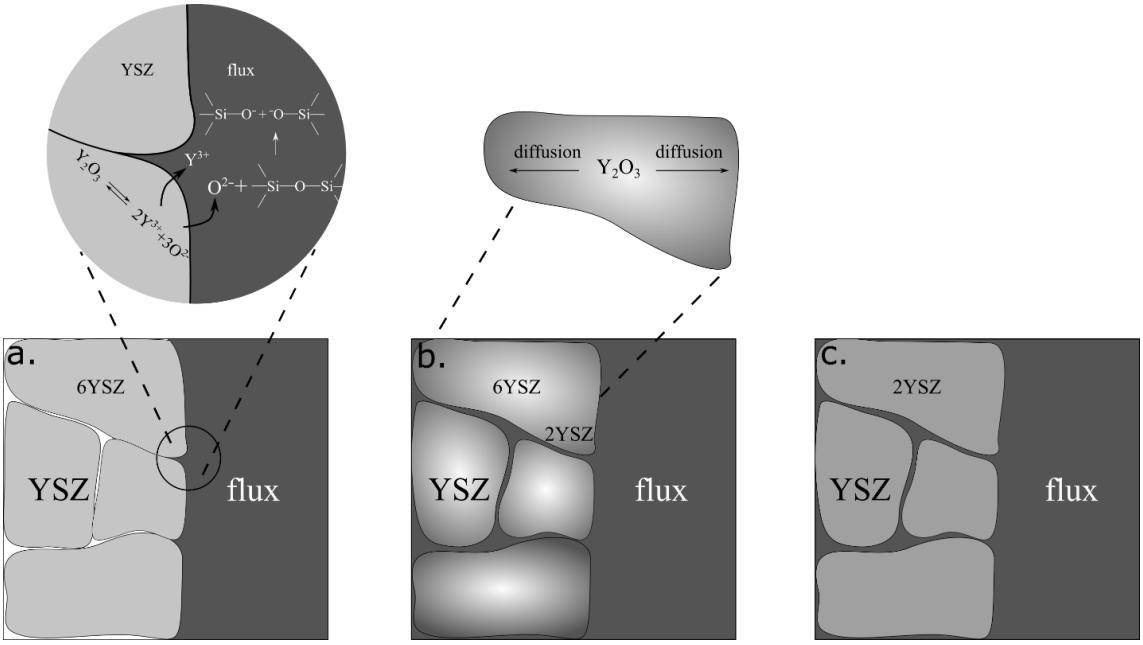

Figure 36. *Schematic of YSZ degradation mechanism when exposed to silica containing flux showing (a) grain boundary attack by SiO_2 in the flux, (b) outward diffusion of yttria in the grains, and (c) resulting formation of YDL with 2YSZ grains with flux accumulated at triple grain junctions.*

The somewhat linear interface between the YDL and unattacked region in the YSZ membrane, as well as the uniform 2YSZ composition in the entire YSZ region indicates that the rate of YDL formation is controlled by the grain boundary attack by the silica in the molten flux. This assertion is supported by the study by Xu et al. [44], which showed that the YDL thickness increases linearly with time of exposure of the YSZ membrane to the silica-containing flux. Since diffusion distances are of the order the average grain radius (< 5μm), this diffusion process is a relatively rapid as compared to the kinetics of the grain

boundary attack.

It is interesting that the yttria depletion in the grains do not continue below the 2YSZ, which is the concentration of yttria in saturated tetragonal YSZ. This phenomenon has been observed in various studies [44 57]. A possible explanation is that the diffusivity of yttria in tetragonal YSZ is an order of magnitude smaller than that in cubic YSZ at 1200ºC [72]. Another possible explanation is that the 2YSZ composition is in thermodynamic equilibrium with the fluxes, all of which contain 4 wt% YF_3.

Since the acidity of silica is responsible for its attack on the YSZ grain boundaries, introduction of CaO, which is a basic oxide, into the flux helps neutralize the acidity of SiO_2. The optical basicity of CaO, Λ=1.0, is higher than that of Y_2O_3, implying that CaO is the strongest electron pair (oxygen ion) donor in the system. When CaO is introduced into the flux, the O^{2-} ions from CaO break the silica network. As a result, the number of oxygen acceptors in the silica network is reduced, leading to a decrease in the oxygen accepting capability of the silica network [51]. This reduces the propensity of the silica network to accept oxygen ions from yttria in the YSZ, thereby reducing the rate of grain boundary attack. Since the optical basicity is a measure of the oxygen donation capability, it is reasonable to assume that when the flux optical basicity is equal to or higher than the optical basicity of yttria, the silica network in the flux no longer acts as an oxygen ion acceptor from yttria, and the grain boundary attack of the YSZ stops. The variation of the optical basicity of the flux as a function of the CaO/SiO_2 mole fraction ratio (based on Equation 27) is plotted in Figure 37. The figure shows that the flux optical basicity is greater than that of yttria when X_{CaO}/X_{SiO_2} ratio in the flux is greater than 1.714 (X_{SiO2} <

$0.583X_{CaO}$). The optical basicity of fluxes used in this study are plotted in the same figure.

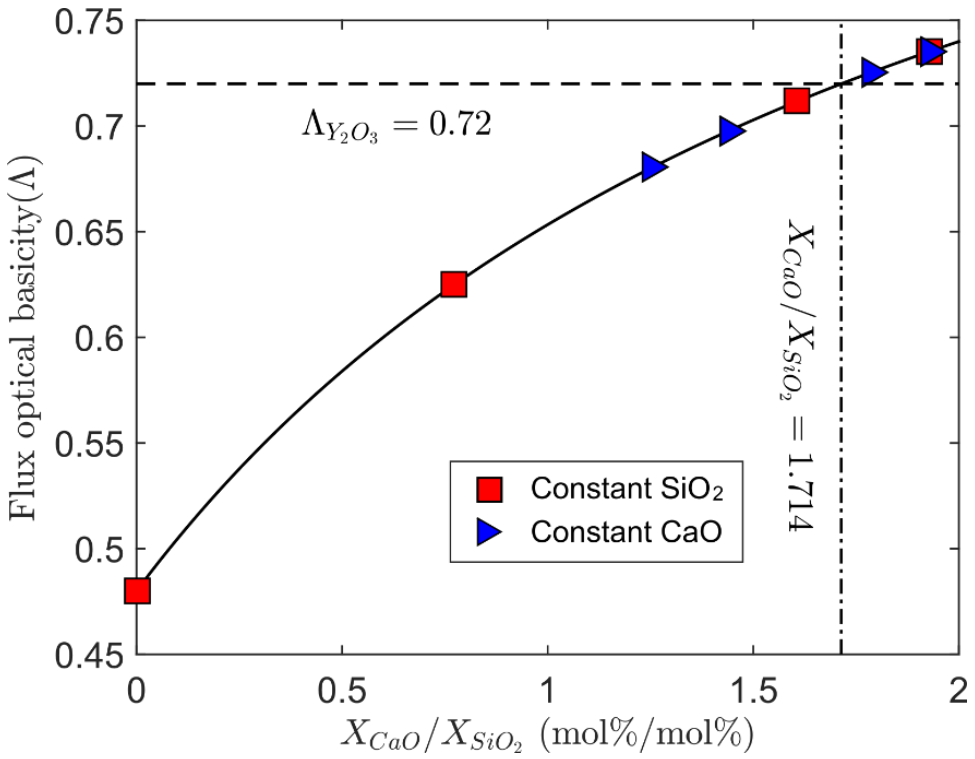

Figure 37. *The optical basicity as a function of the CaO and SiO_2 mole fraction ratio and the optical basicity of the tested fluxes.*

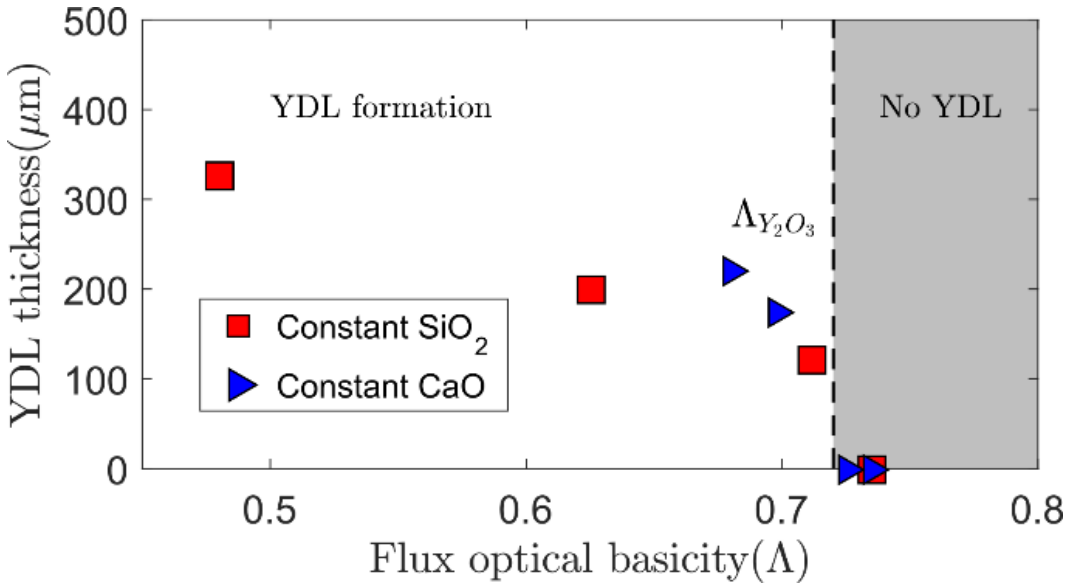

Figure 38. *Plot of optical basicity and YDL thickness for various samples.*

A plot of the YDL thickness versus the optical basicity of the flux is shown in Figure 38. As predicted, when the flux optical basicity is greater than the optical basicity of yttria ($\Lambda = 0.72$), the YDL vanishes and the YSZ membrane is protected. This proves the yttria is no longer an oxygen donor to the modified silica network, once the flux optical basicity is higher than that of the yttria. However, when the optical basicity of the flux is lower than that of yttria, the correlation between the optical basicity and the YDL thickness is unclear. For example, a sample with lower optical basicity exhibits a larger YDL thickness than another sample with higher optical basicity. This implies that the optical basicity of the flux only predicts if the YSZ membrane will be attacked. However, when the grain boundary attack does take place, the kinetics of the attack is not controlled solely by the optical basicity of the flux.

3.4.2.2 The effect of excess silica

As explained in the previous section, the rate-controlling step in the YSZ degradation is the grain boundary attack caused by the interaction between yttria in the YSZ and silica network in the flux, and the attack occurs only when the optical basicity of the flux is lower than that of yttria. When grain boundary attack does take place (i.e., the optical basicity of the flux is lower than that of yttria), one way to think about the effect of the CaO addition is that the CaO neutralizes a portion of the silica, i.e., the neutralized portion of the SiO_2 and the added CaO make the optical basicity of the flux the same as that of yttria ($\Lambda = 0.72$). It is reasonable to assume that the YDL formation kinetics depends on the concentration of the silica that is not neutralized by the CaO. According to the optical basicity calculations, every mole of CaO added to the flux neutralizes 0.583 moles of SiO_2. Thus, the excess (unneutralized) amount of SiO_2 that is active, $X_{SiO2,excess}$, can be calculated as:

$$X_{SiO_2,excess} = X_{SiO_2} - 0.583 \bullet X_{CaO} \tag{32}$$

To explore the role of excess silica in the flux on the YSZ degradation kinetics, a group (Group 3) of fluxes with identical optical basicity but different CaO and SiO_2 amount were tested. Since the YSZ degradation only happens when the flux optical basicity is smaller than that of yttria, the flux optical basicity of 0.625 was chosen. The detailed compositions of tested fluxes are listed in Table 8.

Table 8. Composition of tested flux with a constant optical basicity

Composition (wt%)	**Group 3 Constant optical basicity**			
CaO	2.7	3.6	4.5	5.4
SiO_2	3.75	5	6.25	7.5
YF_3	4	4	4	4
CaF_2	49.43	48.2	47.05	45.9
MgF_2	40.12	39.2	38.2	37.2
Optical basicity (Λ)	0.625	0.625	0.625	0.625

SEM-based EDX line scans were taken across the YSZ flux interface to identify the composition and thickness of the YDL in all the samples tested, and the Y concentration profiles of this group of samples are plotted in Figure 39. The YDL thickness of all samples tested in this group together with the previous two groups are plotted versus the optical basicity of the fluxes they were exposed to, in Figure 40. Clearly, the kinetics of the attack is not controlled solely by the optical basicity of the flux.

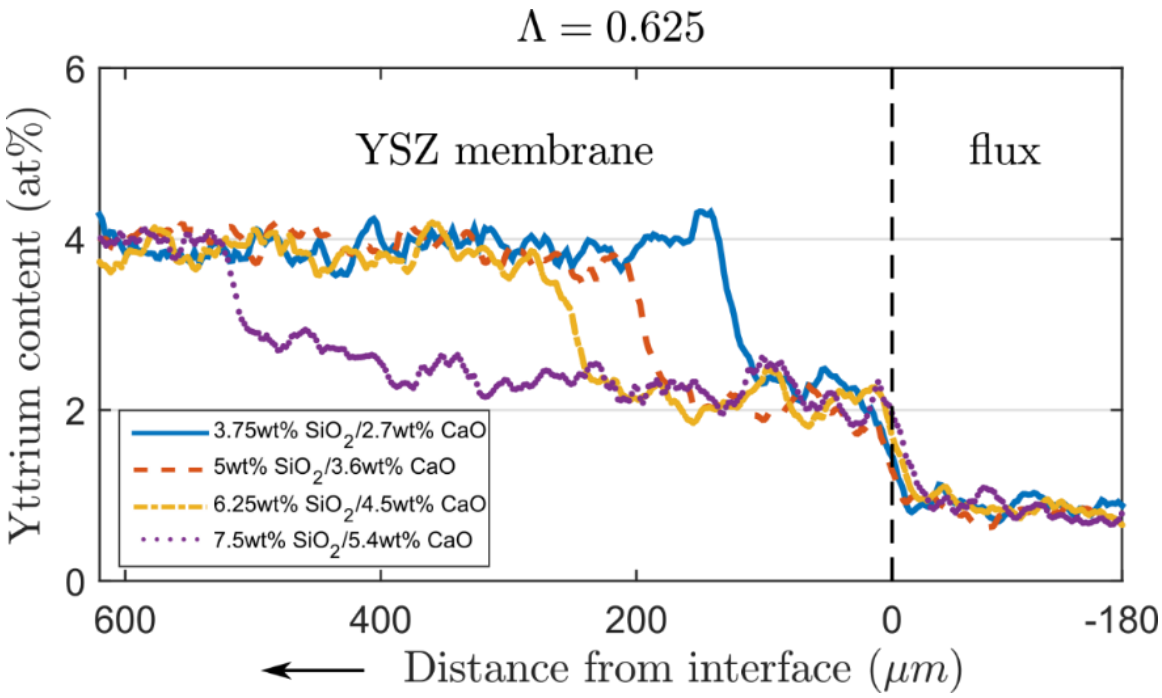

Figure 39. *Yttrium content profile across the YSZ membrane and flux interface for Group 3 (varying CaO and SiO_2 content for a constant optical basicity of 0.625).*

The YDL thickness of each sample in Group 3 is obtained from Figure 39 and is plotted against the excess silica amount of each sample in Figure 41. The YDL thickness shows a near linear positive correlation with the excess silica mole fraction in the flux, indicating that the corrosion reaction is first order with respect to excess silica concentration. These results indicate that while optical basicity predicts whether a grain boundary attack of the YSZ membrane will occur, the kinetics of the grain boundary attack is controlled by the concentration of excess silica (or active portion of the silica network) in the system.

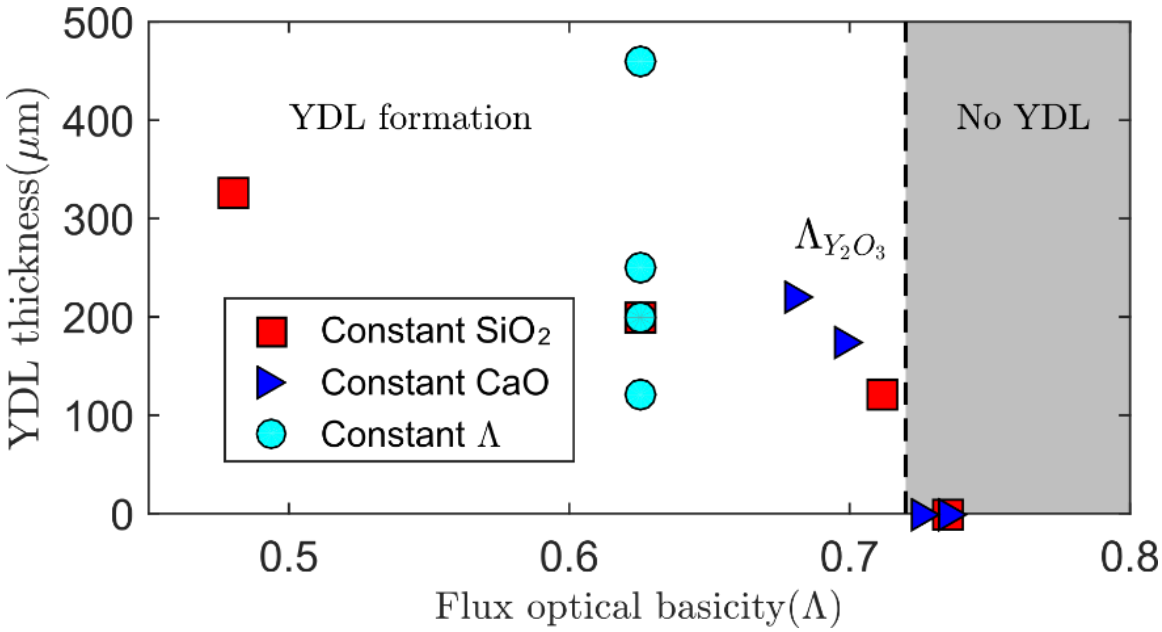

Figure 40. *Plot of optical basicity and YDL thickness for various samples.*

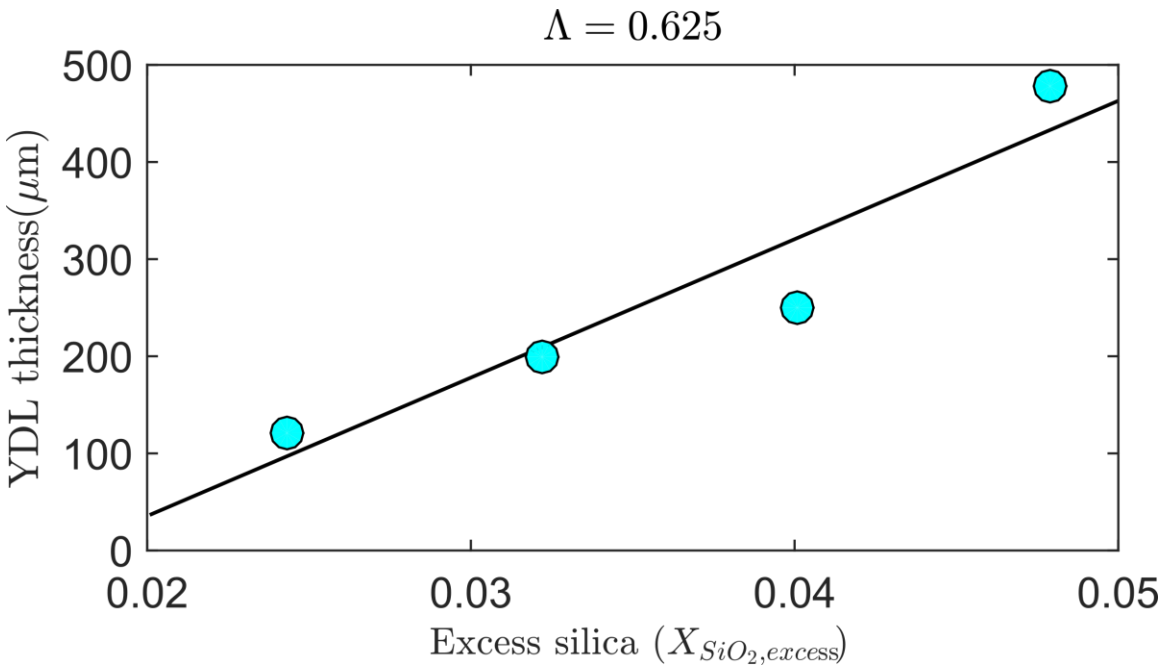

Figure 41. *Plot of excess silica in the flux versus YDL thickness for Group 3 samples.*

3.4.2.3 Diffusion of yttrium in YSZ

In a previous study on the SOM electrolysis of Mg from MgO dissolved in MgF_2-CaF_2 eutectic, it is found that the imbalance between the yttria activity in YSZ and that in flux led to the diffusion of yttrium in a direction perpendicular to the YSZ/flux interface [57]. This outward diffusion of yttrium is independent of the grain boundary attack by the flux, and constitutes a mechanism that can also contribute the formation of the YDL. Since the optical basicity of MgO, $\Lambda = 0.78$ is higher than that of yttria, according to the analysis above, MgO does not cause the grain boundary attack on the YSZ membrane. However, in the Si-SOM, the SiO_2 in the flux can cause YSZ degradation by attacking its grain boundaries. Therefore, in order to study the diffusion behavior of yttrium in the YSZ exposed to the silica dissolved flux, it is necessary to adjust the optical basicity to be higher than that of yttria to remove the grain boundary attack from this process.

Another set of experiments was carried out using a set of flux compositions (Group 4) with higher optical basicity compare to that of yttria (Λ=0.72) and varying YF_3 content from 0wt% to 6wt%. The flux compositions are listed in Table 9. The high temperature annealing experiments are carried out under the same condition as described in Section 3.2.2 except that the annealing time was increased to 120 hours.

Table 9. Flux compositions with varying YF_3 content

Composition (wt%)	**Group 4** **Constant SiO_2 varying YF_3 content**			
CaO	10.4	9.7	9	8.3
SiO_2	5	5	5	5
YF_3	0	2	4	6
CaF_2	46.7	45.0	45.3	44.5
MgF_2	37.9	37.3	36.7	36.2
Optical Basicity	0.754	0.745	0.735	0.725

The SEM based EDX line scans were carried out across the YSZ membrane and flux interface, and the results are plotted in Figure 42. Since the optical basicity of all the fluxes were higher than that of yttria, YSZ grain boundary attack from the silica in the flux was expected to be prevented in all samples. The results indicate that the yttrium activity difference between the YSZ and the flux does drive yttrium diffusion in the YSZ towards the YSZ/flux interface. When the YF_3 content in the flux is low, yttrium diffused into the flux and this leads to the formation of a YDL. The removal of yttrium does allow for flux penetration in the YDL. When the YF_3 content equals or is greater than 2 wt% in the flux, the diffusion of yttria from the YSZ into the flux stops.

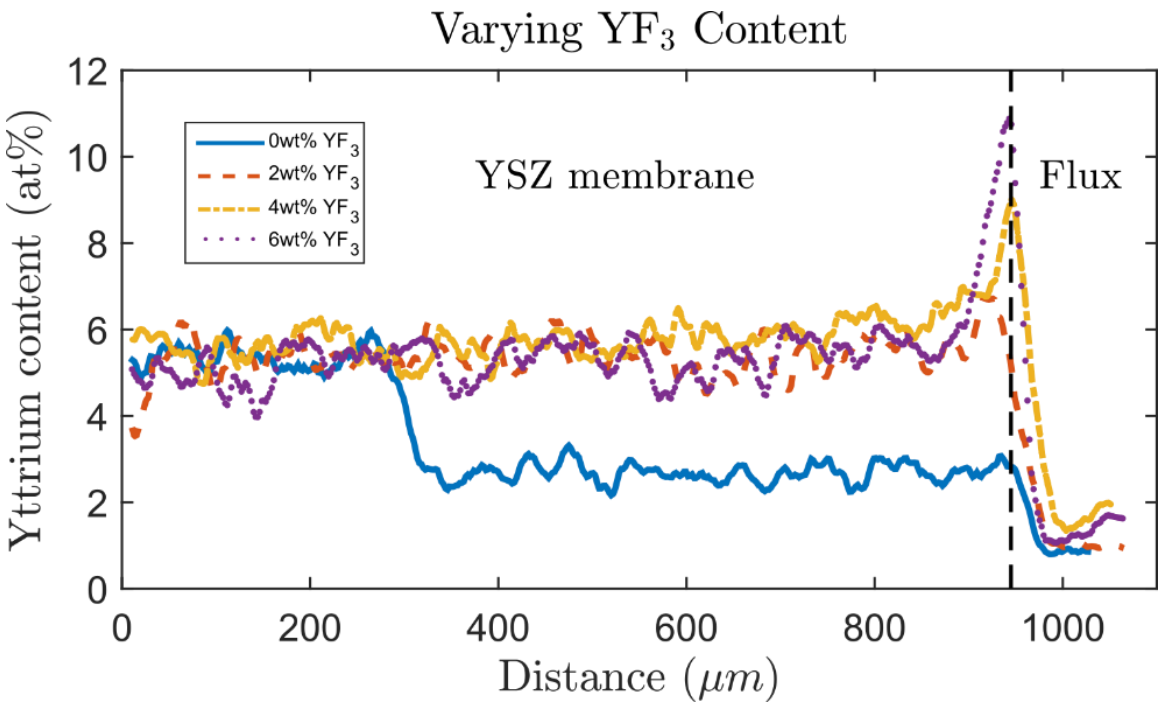

Figure 42. *Yttrium concentration profiles across the YSZ membrane and flux interface for Group 4 samples.*

As observed in a previous study [57], when the YF_3 content in the flux is high (e.g. 4wt% and 6wt%), there is accumulation of yttrium at the YSZ/flux interface. As a result, the yttrium diffused from the flux into the YSZ membrane. The diffusion profile of yttrium diffusion into the YSZ was modeled using the semi-infinite solution to the Fick's second law, given as:

$$C = C_0 + (C_\infty - C_0)\text{erf}(\frac{x}{2\sqrt{Dt}}) \tag{33}$$

where C_0 is the steady state concentration at the flux/YSZ interface, C_∞ is the concentration of yttrium in the bulk YSZ membrane, D is the diffusivity of yttrium in the YSZ membrane. The semi-infinite boundary conditions assume that the YSZ membrane is much thicker

than the diffusion profile.

The experimental data was fitted to the model using the nonlinear least square approximation method. For the experimental data of 6 wt% YF_3, the fitted curve is shown in Figure 43a, and the diffusivity obtained was $D = 7.205 \times 10^{-12}\ cm^2/s$. For the experimental data of 4 wt% YF_3, the fitted curve is shown in Figure 43b and the diffusivity obtained was $D = 6.362 \times 10^{-12}\ cm^2/s$. The two calculated diffusivity values are very close. Since the grain boundary diffusivity of cations is orders of magnitude greater than the lattice diffusivity in the YSZ at 1200°C (1473K), the obtained yttrium diffusivity is compared with the grain boundary diffusivity of yttrium in 3 mol% yttria stabilized tetragonal zirconia (3YTZ) in Figure 44. The figure shows that the calculated diffusivity of yttrium in 6YSZ is higher than the reported diffusivity value in 3YSZ. This might be due to the fact that the tetragonal and cubic structures co-exist in 6YSZ. The cation diffusivity is significantly higher in cubic YSZ than in tetragonal YSZ at this temperature range as shown in Figure 44.

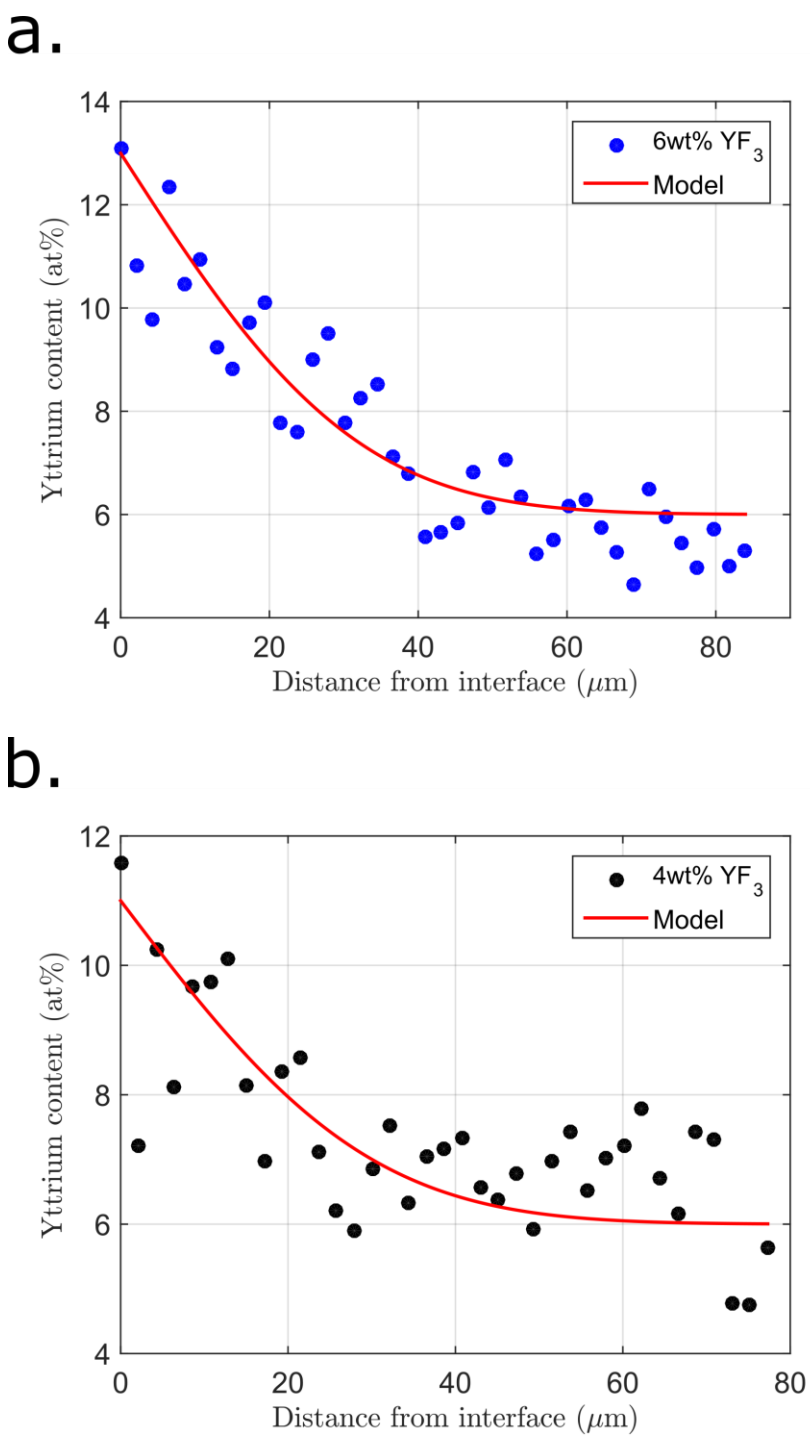

Figure 43. *Diffusion profile of yttrium at the YSZ and the flux interface of (a) the sample exposed to flux containing 6wt% YF_3; (b) the sample exposed to flux containing 4wt% YF_3.*

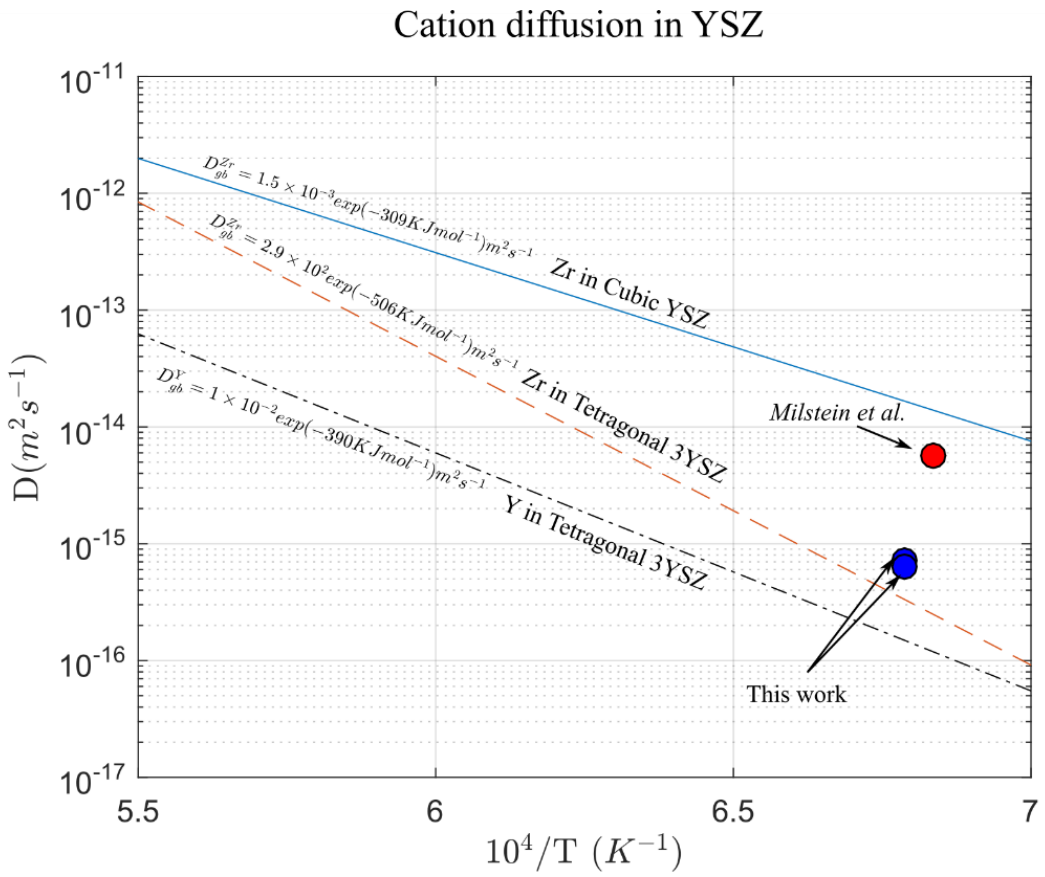

Figure 44. *Diffusivity of cations in cubic YSZ and tetragonal YSZ.(Reconstructed from References [57] and [72])*

It is clear that when there is an imbalance of yttria activity in the flux and the membrane, yttrium can diffuse from the high activity phase into low yttrium activity phase. For the yttria free flux case, losing yttrium from the 6YSZ phase led to the formation of 2YSZ accompanied with a volume change, which could lead to the formation of cracks which leads to the penetration of flux into the membrane. As a result, the diffusion distance for yttrium in the YSZ membrane to reach liquid flux is significantly reduced, thereby increasing the rate of diffusion of yttrium into the flux. This allows for yttrium depletion across 100s of microns in thickness. When the yttria activity in the flux is higher than that

in YSZ, yttrium diffuses into the YSZ from the flux. Since there is no cracks formation and the liquid flux was unable to creep into the grain boundaries. The yttrium can only diffuse though the solid phase, and the diffusion distances are much shorter (only 10s of microns).

These experiments confirm that the oxide acidity is not the sole reason that causes the degradation of YSZ. A low activity of yttria in the flux (compared to YSZ) can also led to the formation of a YDL. Therefore, to prevent the YSZ membrane from degradation, both the optical basicity of the flux and the yttria activity of the flux has to match with that of YSZ. A flux containing 5wt% SiO_2 requires 8wt% CaO to neutralize the acidity of the silica and match the optical basicity of the flux to that of yttria. Since silica is a common impurity in the MgF_2 [73], excess CaO is recommended to ensure the YSZ membrane is protected from the attack. To prevent yttrium diffusion from the YSZ membrane into the flux, more than 2wt% of YF_3 is required in the flux. Therefore, a flux with 5wt% SiO_2, 9wt% CaO, 4wt% YF_3 and reminder eutectic MgF_2-CaF_2 was selected for SOM electrolysis.

3.5 Conclusions

In this study, the detailed correlation between the flux composition, its optical basicity, and the chemical stability of a YSZ membrane exposed to the flux at high temperature, was investigated. The optical basicity of the flux can be adjusted by changing the ratio between the acidic SiO_2 and basic CaO. When the optical basicity of the flux is lower than the optical basicity of the yttria in the YSZ membrane, the silica network in the

flux attacks the YSZ grain boundaries by attracting oxygen ions from yttria at the YSZ grain boundaries, and causing yttrium ions at these locations to get incorporated into the flux. This leads to yttria depletion in the 6YSZ grains, and the concentration difference between the bulk of the grain and the grain boundary leads to an out-diffusion of yttria from the grain to the grain boundary. This converts the partially stabilized 6YSZ to tetragonal 2YSZ in the YDL. The kinetics of YDL formation is controlled by the rate of grain boundary attack by the silica in the flux, which is itself controlled by the concentration of the silica in the flux that is not neutralized by CaO. Once the optical basicity of the flux matches than that of yttria, the YSZ membrane is protected from the grain boundary attack and YDL formation. In addition to the grain boundary attack, chemical diffusion of yttrium due to the imbalance of yttria activity in the YSZ and flux is another cause of yttria depletion. To counter this imbalance, greater than 2wt% of YF_3 in the flux is required. Based on these results, a eutectic CaF_2-MgF_2 flux with 5wt% SiO_2, 9wt% CaO, and 4wt% YF_3 is proposed for SOM electrolysis for Si production with lower concentration polarization losses and no attack on the SOM membrane.

4. Structures of Molten Lithium Chloride and Lithium Mixtures

4.1 Introduction

Molten LiCl-Li_2O is commonly used as the electrolyte in the electrolytic production of metal such as Ti [74], Ta [75], Nb [76] and U [77] from their oxides. In some of these electrolysis processes, when the dissociation potential of metal oxide is close to that of Li/Li^+, Li^+ is unavoidably reduced with the desired metal cation. As the process proceeds, the produced Li metal is found to be dispersed in the electrolyte [77 78]. The dissolution of Li reduces the current efficiency of the electrolysis system and causes corrosion of system components. Therefore, it is important to understand the dispersion mechanism of Li metal in the molten salt. Although there have been extensive studies on this subject [77 78], however the detailed mechanism is not fully understood.

One possible mechanism is the formation of hyperlithiated compounds such as Li_2Cl in the molten LiCl matrix which has been studied theoretically [79 80]. However, no experimental evidence has been reported about their existence in a fused phase. In several other studies, micron-sized metallic particles were found in quenched LiCl-Li, which suggests colloidal suspension is another path of Li dispersion in LiCl [81-84].

Suspensions of nanoparticles in other molten salts have been investigated in various applications due to their unique physical properties [85]. In a recent study, Merwin et al. reported that *in-situ* Raman spectra of LiCl-(LiO_2)-Li mixtures corresponded to the presence of Li_8 nanoclusters in the mixture with and without the presence of LiO_2 [86]. However, the Raman spectroscopy measurements were taken from the top surface of the

Li-LiCl mixture that might be affected by the presence of Li vapors. To eliminate the uncertainty of interference from Li vapor, a direct measurement on bulk liquid is required. The use of synchrotron based high energy x-ray diffraction (HEXRD) has a long history of studying liquid structure by obtaining the Pair Distribution Function (PDF) of the liquid being studied [87]. Information, including distance between neighboring atoms, bond angles and density can be extracted from the pair distribution function of liquid. The high penetration of high energy x-rays allows for the direct measurement on the bulk molten salts by transmitting the beam through a transparent port in the crucible and through the bulk fluid. In this work, the structure of molten Li-LiCl mixture is characterized using *in-situ* HEXRD.

4.2 Experimental Details

Due to the reactivity of the components present in the liquid, the experiments need to be conducted under an inert atmosphere. The schematic of the chamber design for the in-situ study of molten Li-LiCl is shown in Figure 45. The stainless steel chamber has five circular openings which host the gas outlet/inlet, heating element power inlet, electrodes inlet and two Kapton film windows. Inside the chamber, the holder for the amorphous carbon crucible is fixed using screws on to an aluminum silicate plate that is itself bolted to the bottom stainless steel plate of the chamber. The amorphous carbon crucible used in this study had an inner diameter of 4 mm and a wall thickness of 0.5mm.

The HEXRD experiments were performed at the Advanced Photon Source (APS)

station 6-ID-D at Argon National Laboratory. The high-energy synchrotron-based x-ray has a wavelength of 0.1235Å (100keV energy). The HEXRD experiments are conducted using a direct transmission geometry setup as shown in Figure 46. The incident X-ray beam goes through the Kapton film window and hits the carbon crucible, while the diffracted beam comes out from the other side and reaches the 2D detector through the other Kapton film window. Kapton was chosen as the window material due to its nearly perfect transmission of high energy x-rays. Additionally, vitreous amorphous carbon was used for the melt containing crucible due to its lack of crystallinity and minimal absorption cross section for high energy x-rays.

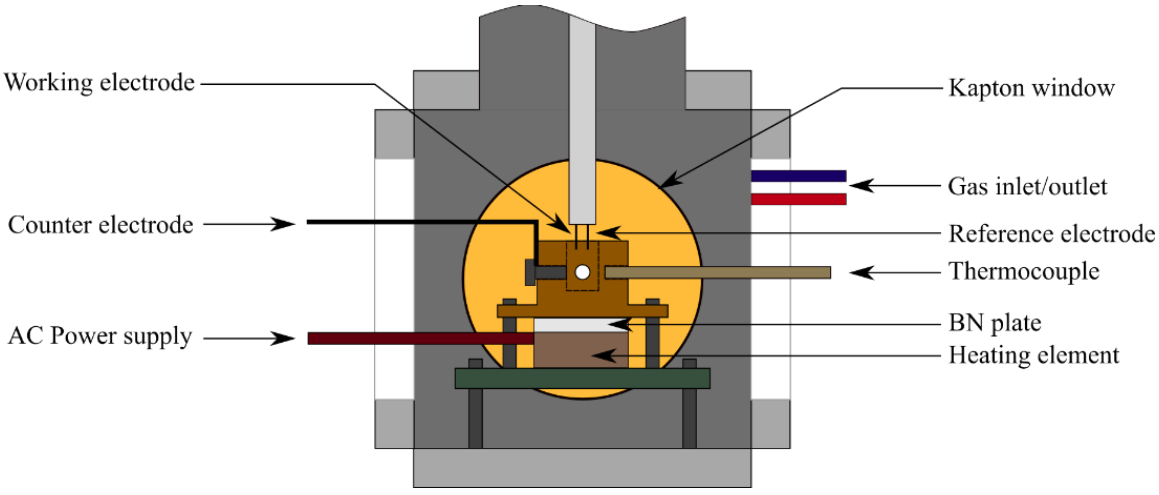

Figure 45. *Schematic of the vacuum chamber for in-situ HEXRD experiment.*

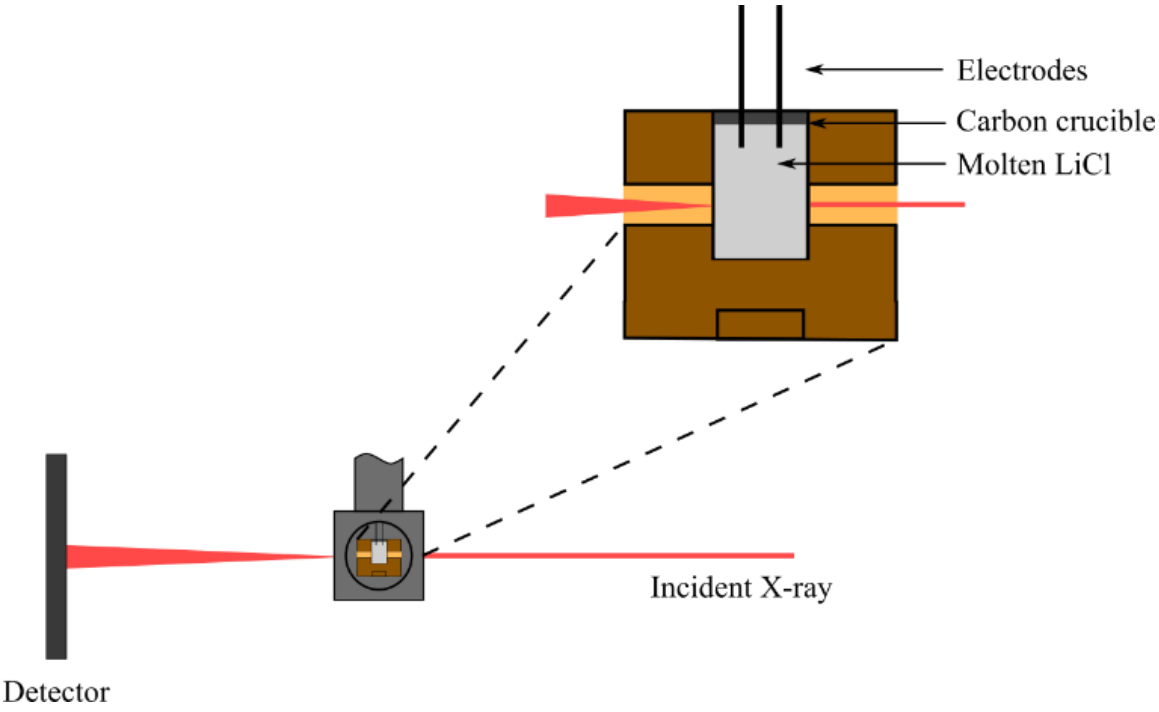

Figure 46. *Schematic of High Energy X-ray Diffraction experiment setup.*

To obtain the background diffraction of the containers (e.g. carbon crucible and Kapton films) used in this experiment, the empty amorphous carbon crucible was loaded into the chamber. The system was then heated to and held at 500, 600 and 650°C. During the heating process, the system was first pumped down to -20 inHg gauge pressure for 30 minutes and then purged with Ar to 5 inHg gauge pressure to establish an inert atmosphere in the chamber. The HEXRD data of the amorphous carbon crucible and Kapton windows at different temperatures were recorded. After the system was cooled down, approximately 0.15g solid LiCl (99.998% Purity, Sigma-Aldrich, Milwaukee, WI) was loaded into the cylindrical amorphous carbon crucible. The system was then first pumped down to vacuum for 30 minutes to eliminate the water and oxygen inside the chamber, before it was purged with Ar back to 5 inHg gauge pressure to avoid the evaporation of molten LiCl during the

heating process. While the system was held at 650°C and the LiCl melted, the high energy X-ray beam was incident on the sample, and the diffraction data was recorded. After the diffraction data of pure LiCl was recorded, the tungsten electrodes were lowered into the molten LiCl. As shown in Figure 45 and 46, one of the tungsten wires acted as the working electrode, the other tungsten wire acted as the quasi-reference electrode, and the amorphous carbon crucible that was connected to a stainless steel wire acted as the counter electrode. These electrodes were connected to a potentiostat (Solartron Analytical, Hampshire, UK) that electrochemically reduced Li+ to Li by passing a constant current of 60 mA through the system for 120 s with an applied voltage between the working electrode and counter electrode greater than the dissociation voltage of LiCl. Assuming 100% current efficiency, the reduced lithium can be calculated using Faraday's law of electrolysis as:

$$m = \frac{It}{zF} M \approx 0.52 \times 10^{-3}\ g \tag{34}$$

where *I* is the input current, *t* is the electrolysis duration, *z* is the valence number of lithium ion, and *F* is Faraday constant. Under these conditions, the theoretical maximum amount of reduced lithium is about 0.35 wt% or 2.1 mol% of the total LiCl in the crucible, which is within the range of solubility limit of Li in LiCl (greater than 3 mol%) reported in various sources using different methods at 923K [83 84 88 89]. The HEXRD data was recorded during the electrolysis process, and was continued after the electrolysis for a total time of 300s.

4.3 Results

The diffraction data of pure molten LiCl was obtained by subtracting the signal obtained from amorphous carbon crucible and Kapton film windows. The structure factor of molten LiCl is plot in Figure 47a. The structure factor of LiCl is transformed into the Pair Distribution Function (PDF) of LiCl using a Fourier Transform. The PDF of molten LiCl before electrolysis is plot in Figure 47b. The PDF data obtained from these HEXRD experiments is compared with that obtained from neutron scattering [90 91] in Figure 47a and Figure 47b. Both structure factor and PDF data from HEXRD show reasonable agreement with the neutron diffraction data. McGreevy et al. identified the first peak in the PDF LiCl as the Li-Cl bond and the second peak is the combination of Li-Li and Cl-Cl bonds from the neutron scattering data of molten LiCl [91]. Since the scattering probability is proportional to the square of the atomic number of the atom, the Li-Li bond peak intensity is approximately 1/32 of the Cl-Cl bond peak intensity. As a result, The Li-Li bond is embedded in the shoulder of the Cl-Cl bond.

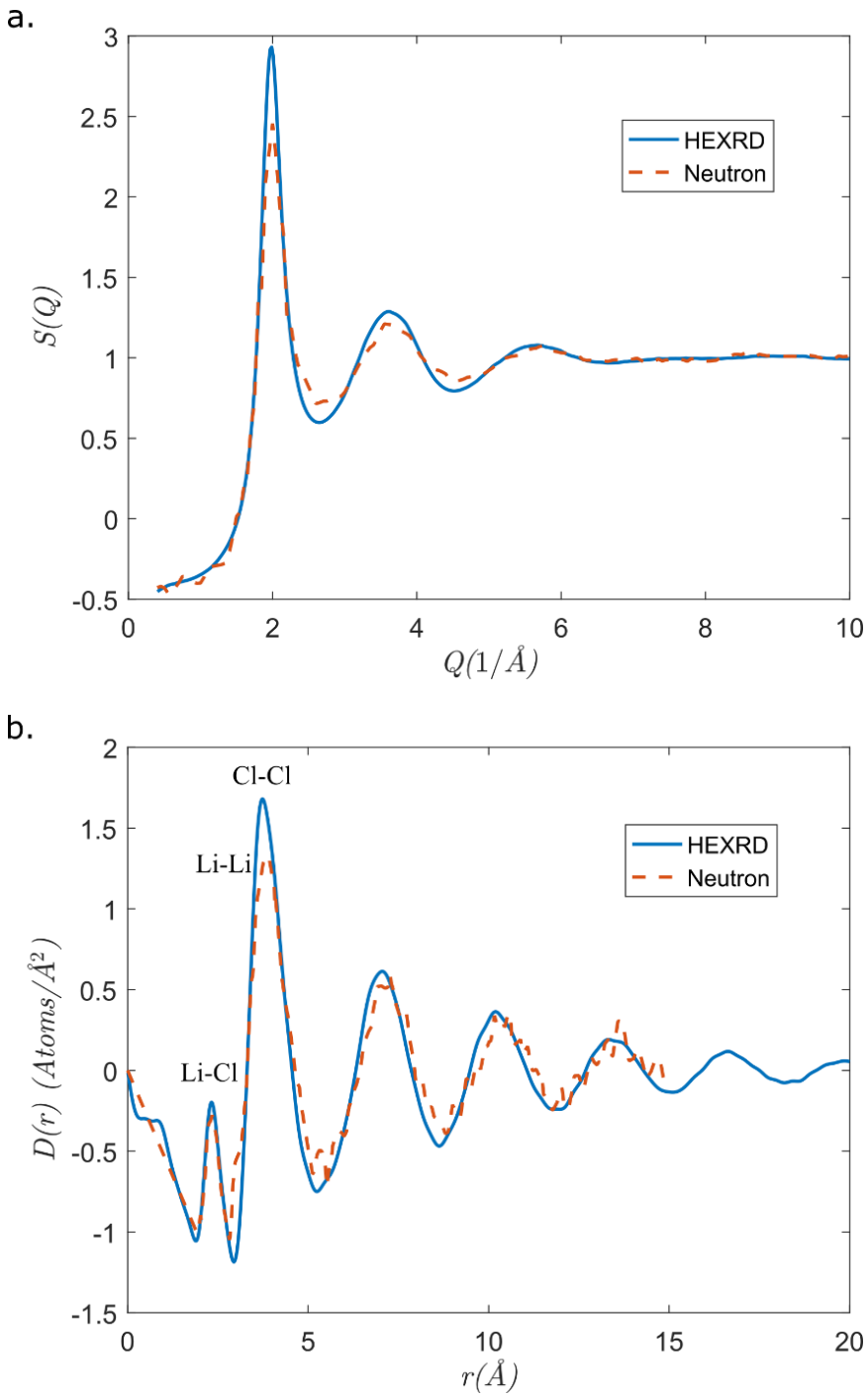

Figure 47. *(a) The structure factor and (b) the pair distribution function of molten LiCl at 650°C*

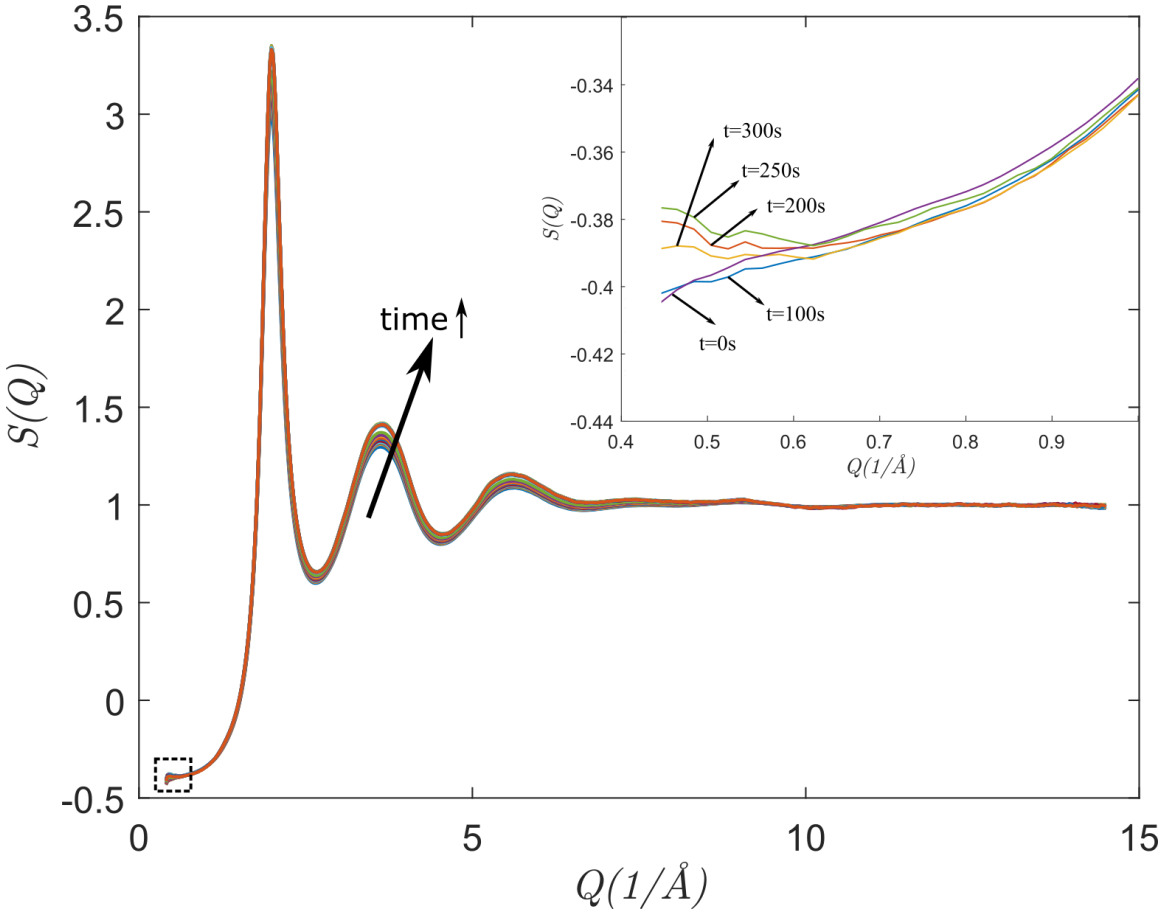

Figure 48. *Structure factor of molten LiCl-Li mixture during the electrolysis experiment. The insert shows the structure factor data in low scattering vector (Q) region.*

The structure factor of LiCl during the entire electrolysis experiment is plotted in Figure 48 with each line representing an average of the structure factor data within every 10s interval. The structure factor of LiCl-Li curve in general keeps the same shape with an increasing intensity in the mid to high scattering vector *Q* region (2 - 14Å^{-1}). In the low scattering vector *Q* region (Q < 1Å^{-1}, selected using a dashed square), the increase in structure factor curve intensity is more obvious as shown in the insert in Figure 48. The pair distribution function of LiCl obtained during the same electrolysis process is plotted in Figure 49 with each line representing an average of the PDF data within every 10s

interval. From the plot, a subtle change in the pair distribution function of the molten LiCl is observed as the electrolysis proceeds. To exam this change in detail, the PDF data of LiCl during electrolysis in the range of r = 3.3Å to r = 4.5Å (Li-Li and Cl-Cl peak) at t = 0s (before electrolysis), 100s (during electrolysis), 200s and 300s (after electrolysis) is plotted in Figure 50. It is clear that the peak intensity increases as the electrolysis proceeds and keeps relatively constant after electrolysis ends. To extract this increase in the LiCl-Li mixture PDF peak intensity over time, the peak intensity at r = 3.76Å is plotted against time in Figure 51. In the plot, the period that electrolysis was in progress is indicated as a shaded area. It is apparent that the atomic density in this region increases during the electrolysis and once the electrolysis ends, the atoms density stays almost constant. Besides the peak intensity increase, the peak position was found to be shifted during the electrolysis process. To observe this shift in more detail, the position r at the half maximum of the peak on the left side of the curve and on the right side of the curve shown in Figure 50 is tracked and plotted in Figure 52. From the plot, it is clear that the both the left and right half maximum points of the peak shifted to the left by around 0.01Å after the electrolysis process stops.

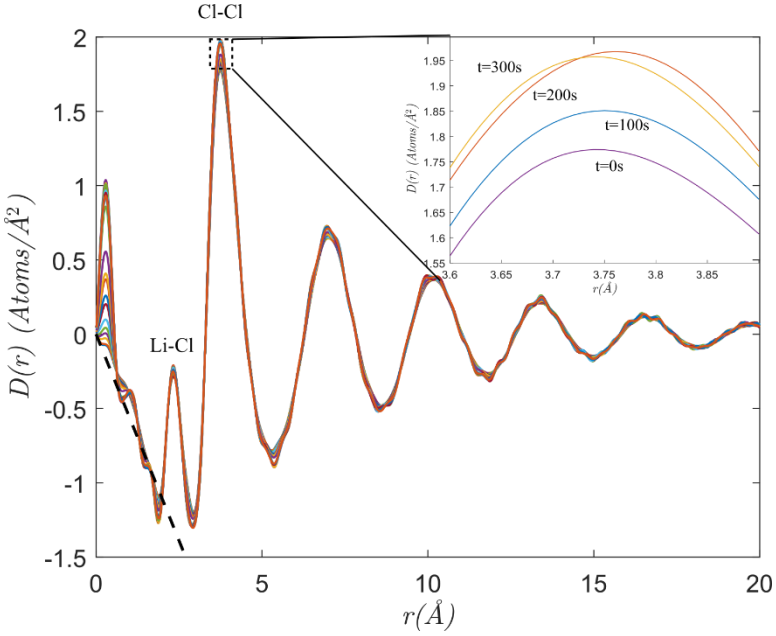

Figure 49. *Pair distribution function of LiCl-Li mixture during the electrolysis experiment. The insert shows the zoomed selected region*

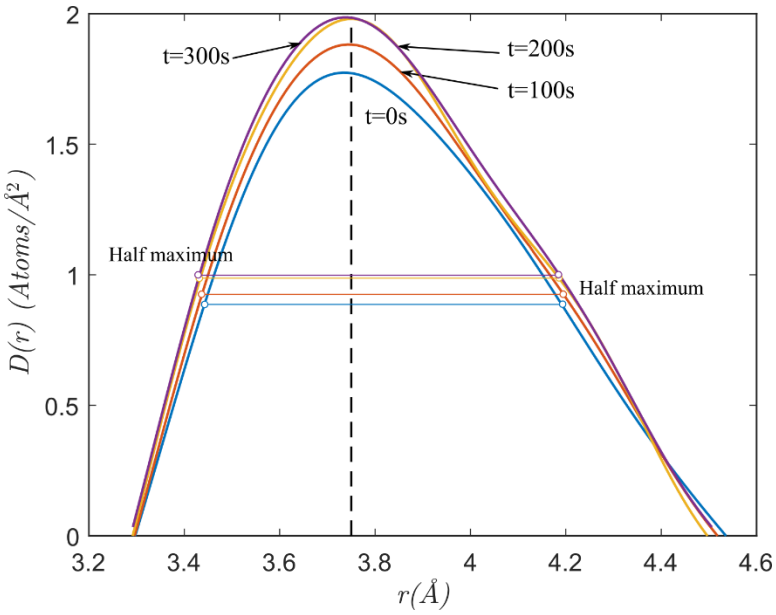

Figure 50. *Pair distribution function of LiCl-Li mixture during the electrolysis experiment at r = 3.3 to 4.5Å.*

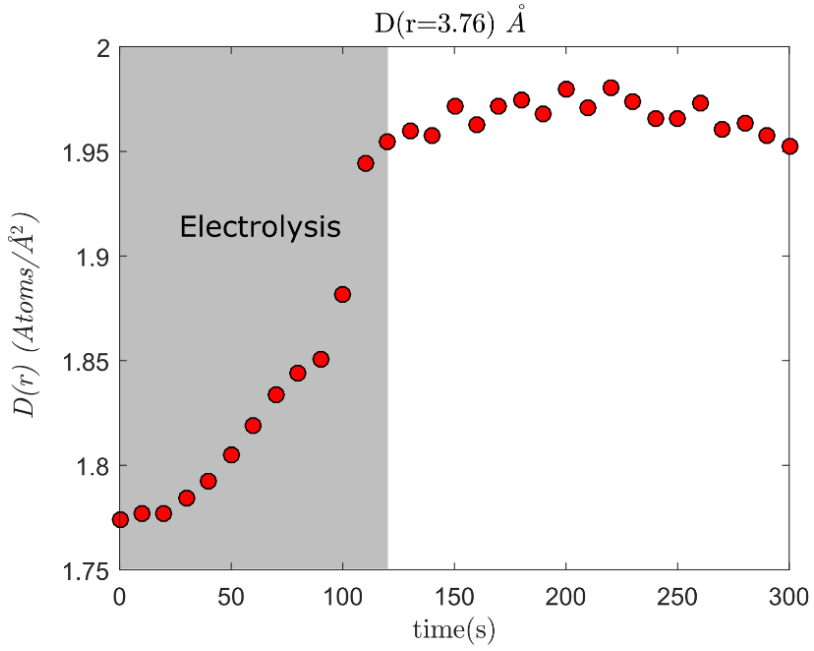

Figure 51. *Pair distribution function peak intensity of LiCl-Li during the electrolysis experiment at r = 3.76Å.*

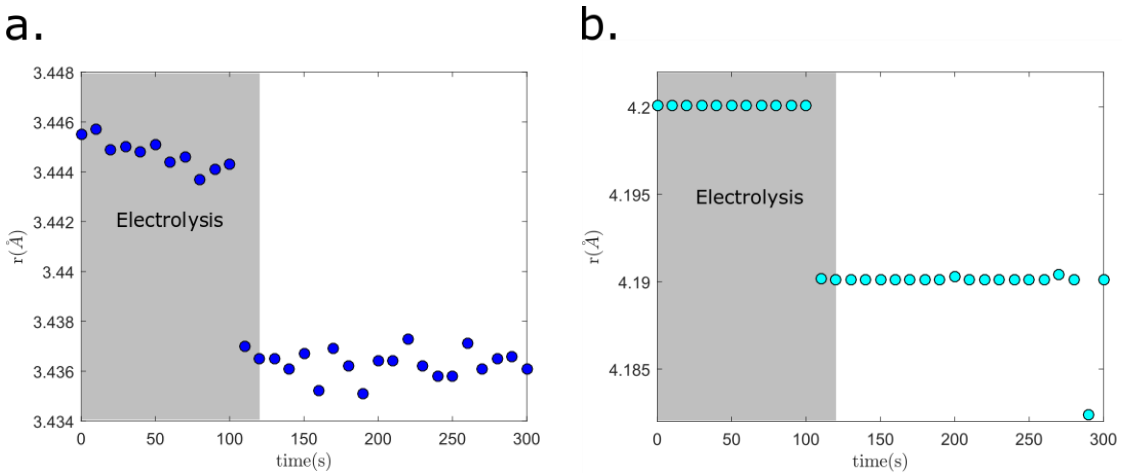

Figure 52. *The position of the half maximum point of the peak on a. the left side and b. the right side of the curve.*

4.4 Discussion

The PDF of LiCl-Li mixture during and after electrolysis indicate that the electrolysis caused a short range (2-5Å) atoms density fluctuation in the LiCl. However, the bulk density, as measured by the unphysical region (0-2Å), did not change. Furthermore, no additional Li-Li peak is observed. A possible reason is that the Li-Li peak intensity in the PDF plot of LiCl is much weaker compared to that of the Cl-Cl peak. As shown in Figure 53, in the combined LiCl PDF data, the weight of Li-Li partial PDF is much smaller compared to that of Li-Cl and Cl-Cl [91]. The Li-Li peak is embedded in the left shoulder of the Cl-Cl peak. Another possible explanation is that the concentration of Li in the LiCl-Li mixture produced through electrolysis process was low (~ 2mol% or less). As a result, the signal intensity from the Li is weaker comparing to that from LiCl. Therefore, it is difficult to distinguish the change in Li-Li peak from the Cl-Cl peak.

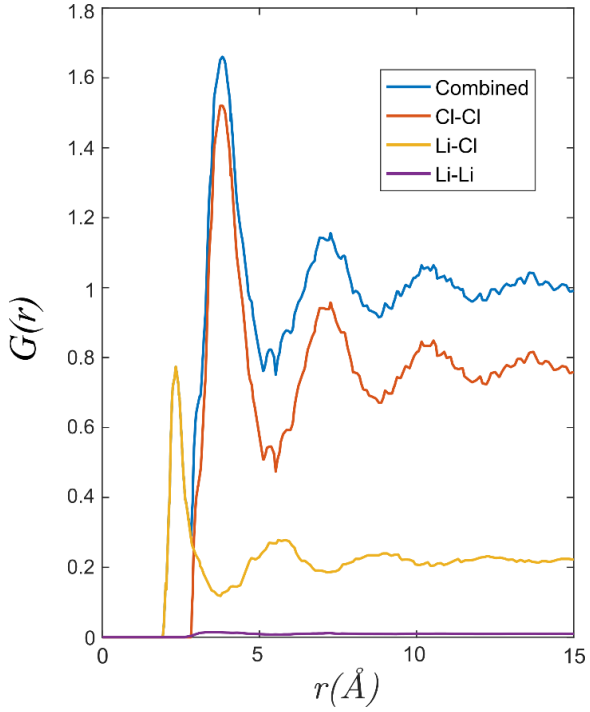

Figure 53. *Partial PDF and combined PDF of LiCl (reconstructed from [91])*

The increase in the structure factor of the LiCl-Li mixture at low scattering vector *Q* range (0.4-0.6Å^{-1}) during electrolysis process indicates local atom density fluctuations in the mid-long range (10-15Å) in real space. This implies the existence of nanometer sized structuring in the melt. Structuring on this length scale is hypothesized to indicate the presence of the previously mentioned Li nanoclusters (e.g. Li_8). The presence of such clusters in the otherwise homogenous fluid may be the cause of atomic density fluctuations in this region. It is also worth noticing that, in the PDF of LiCl-Li mixture, the position of the fist Cl-Cl peak is shifted to the lower distances after the electrolysis by 0.01Å. This indicates the distance between Cl^- ions is shortened. This Cl-Cl distance shortening might also be caused by the formation of lithium nano clusters. A possible mechanism of this shortening effect is shown schematically in Figure 54. In molten LiCl, a Li^+ ion is most

likely surrounded by 5 Cl^- ions as shown in Figure 54 [91]. In a unit volume, after the electrolysis, the Li-Cl cluster is pushed away by the formed Li cluster (Li_8 is used here as an example). However, the bulk density of the liquid did not change over the electrolysis process, as evidenced by the constant slope of the dashed line in Figure 49, which is proportional to the bulk density of the liquid. This implies that the mass of the atoms in this unit volume should be relatively constant. The formation of one Li_8 cluster causes about 1.5 Cl ions out of the unit area, but total numbers of atoms in the unit area increases. To accommodate the increased numbers of atoms in the unit volume, the distance between atoms is shortened, which is observed as the Cl-Cl peaks shifting to the shorter distance direction in the PDF of the molten mixture.

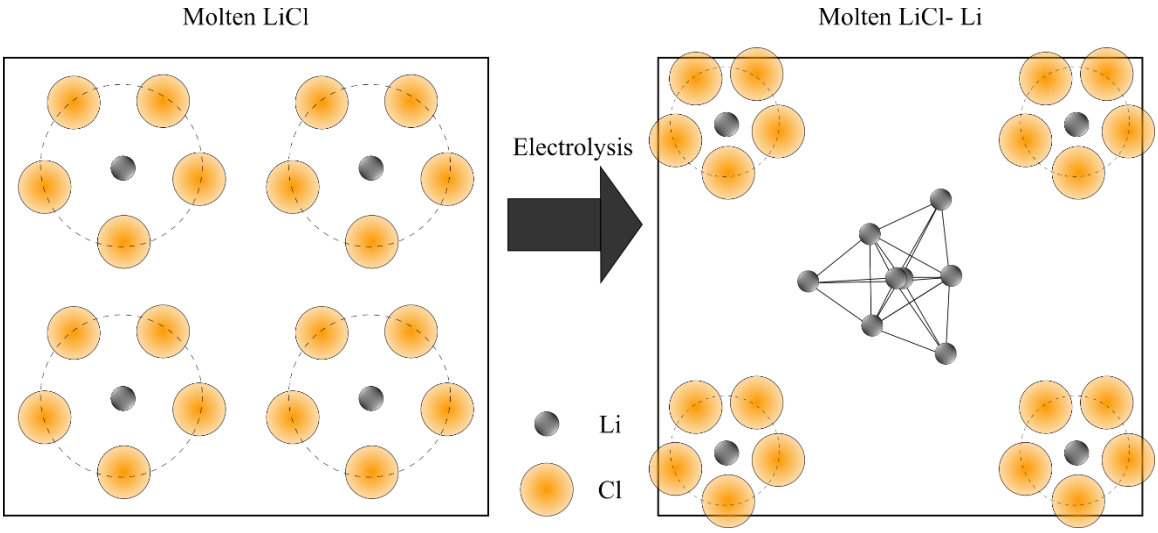

***Figure 54**. Schematic of the formation of Li_8 clusters in molten LiCl (not to scale)*

Thus, the HEXRD experimental results indicate the presence of atomic density fluctuations in the mid-long range (~10 Å) in the molten fluid, which is accompanied by

the reduction in the distance between Cl atoms. It is hypnotized that the metallic Li atoms form lithium clusters in molten LiCl that causes these changes.

4.5 Conclusions

In this study, the structure of molten LiCl and molten LiCl-Li mixtures was characterized using the high energy X-ray diffraction technique. The obtained structure factor and pair distribution function of molten LiCi agrees with those obtained from neutron scattering. The LiCl-Li mixture was produced by electrochemically reducing Li^+ to Li in molten LiCl under an inert atmosphere. The structure factor and pair distribution function of LiCl-Li mixture was recorded during and after the electrolysis process. It was found that the intensity of the Cl-Cl peak in the pair distribution function of LiCl-Li mixture increased while the Li was being produced and remained constant after the electrolysis stopped. The Cl-Cl distance was found shortened by 0.01Å in the PDF plot after the electrolysis, which is proposed to result from the formation of Li nano-clusters. The findings from this study are in agreement with the hypothesis that metallic Li disperses in Li as nano-clusters. The detailed size and structure of the Li nano cluster can not be discerned in the HEXRD experiment, since the resolution of HEXRD is limited at lower angles (low scattering vector region). To quantitatively study the specific sizes of these Li nano-clusters, small angle scattering (SAX) technique can be applied in future studies.

5. Conclusions

This dissertation covers three diverse applications of materials interactions under high temperatures. In the first application, a germanium-core borosilicate cladding optical fiber that showed mid-infrared transmission was successfully fabricated using the 'rod-in-tube' method. The neck formation in the fiber preform during the drawing process was modeled. The model is in good agreement with the experimental data and provided guidance for the optimal positioning of the semiconductor core in the preform. Characterization of the fibers showed excellent crystalline quality of the fibers with most grain boundaries being twin boundaries. Also, the optimal placement of the Ge core in the preform minimized the time the molten core was in contact with the borosilicate glass, thereby allowing minimal impurity diffusion from the cladding to the core. This led to the lowest reported losses in such fibers fabricated by the 'rod-in-tube' method, to date.

The solidification of the germanium core in the drawn fiber was studied using a proxy of ice melting in cylindrical containers. The melting time is found to scale with the dominant heat transfer mechanism in the system. The competing mechanisms are the conductive heat transfer from the top and convective heat transfer from the side. The ratio between them depends on the Rayleigh number of the fluid and the thermal conductivity of the container wall. This result provides an estimation of the germanium core solidification time and can be further applied to guide the design of phase change materials for energy storage.

For the application of Si production by SOM-based electrolysis, the corrosion of

YSZ ceramic membrane in contact with the silicon containing molten oxy-fluoride flux was studied. It is found the silica network in the flux attacks the YSZ grain boundaries, when the optical basicity of the flux is lower than that of the yttria in the YSZ membrane. Silica in the flux, which is more acidic than yttria in the YSZ, attracts oxygen ions away from the yttria, especially located at the grain boundaries of YSZ. In addition, yttrium diffuses out of the YSZ grains to the flux due to an activity difference in the YSZ grains and the flux. This grain boundary attack causes the formation of an yttria depletion layer. The kinetics of the YDL formation is controlled by the rate of grain boundary attack by the silica in the flux. The flux can be made more basic by adding CaO, and its optical basicity can be adjusted by changing the ratio between the acidic SiO_2 and basic CaO. Once the optical basicity of the flux matches than that of yttria, the YSZ membrane is protected from the grain boundary attack and no YDL formation occurs. Adding YF_3 in the flux also reduces the activity difference of yttrium between the membrane and the flux. Based on the experimental results, a eutectic CaF_2-MgF_2 flux with 5wt% SiO_2, 9wt% CaO, and 4wt% YF_3 was chosen for SOM electrolysis for Si production, and led to lower concentration polarization losses with no attack on the SOM membrane.

In the last application, the structure of molten LiCl and molten LiCl-Li mixture is studied using in-situ High Energy X-Ray Diffraction (HEXRD) technique. The structure factor and pair distribution function (PDF) obtained from the HEXRD agrees with those derived from the neutron diffraction. The LiCl-Li mixture is produced by the electrochemical reduction of Li+ ions to Li metal in molten LiCl, while its structure being examined using HEXRD. The structure factor and pair distribution function of LiCl-Li

mixture is compared with those of pure LiCl. The structure factor intensity is found increased in the low scattering vector region which indicates the formation of nanometer sized clusters. The atoms density fluctuation and the decrease between Cl-Cl shown in the PDF of LiCl-Li mixture are also found caused by the formation of Li nano clusters. These changes qualitatively confirm that Li disperses in LiCl in the form of lithium nano-clusters.

BIBLIOGRAPHY

1. The Nobel Prize in Physics 2009. Secondary The Nobel Prize in Physics 2009. http://www.nobelprize.org/nobel_prizes/physics/laureates/2009/.

2. Loewenstein KL. The manufacturing technology of continuous glass fibers. 1973

3. Saleh BE, Teich MC, Saleh BE. *Fundamentals of photonics*: Wiley New York, 1991.

4. Willer U, Saraji M, Khorsandi A, Geiser P, Schade W. Near-and mid-infrared laser monitoring of industrial processes, environment and security applications. Optics and Lasers in Engineering 2006;**44**(7):699-710

5. Sanghera J, Shaw L, Busse L, et al. Development and infrared applications of chalcogenide glass optical fibers. Fiber & Integrated Optics 2000;**19**(3):251-74

6. Sulfide and heavy metal oxide glasses for active fibers. Infrared Glass Optical Fibers and Their Applications; 1998. International Society for Optics and Photonics.

7. Optical and mechanical properties of silver halide fibers. Infrared optical materials and fibers V; 1987. International Society for Optics and Photonics.

8. Simhony S, Schnitzer I, Katzir A, Kosower E. Evanescent wave infrared spectroscopy of liquids using silver halide optical fibers. Journal of Applied Physics 1988;**64**(7):3732-34

9. Szebesta D, Davey S, Williams J, Moore M. OH absorption in the low loss window of ZBLAN (P) glass fibre. Journal of Non-Crystalline Solids 1993;**161**:18-22

10. Sanghera J, Aggarwal I. Active and passive chalcogenide glass optical fibers for IR applications: a review. Journal of Non-Crystalline Solids 1999;**256**:6-16

11. Kanamori T, Terunuma Y, Takahashi S, Miyashita T. Chalcogenide glass fibers for mid-infrared transmission. Journal of Lightwave Technology 1984;**2**(5):607-613

12. Harrington JA. *Infrared fibers and their applications*: SPIE press Bellingham, WA, 2004.

13. Scott BL, Wang K, Caluori V, Pickrell G. Fabrication of silicon optical fiber. Optical Engineering 2009;**48**(10):100501

14. Ballato J, Hawkins T, Foy P, et al. Silicon optical fiber. Optics Express 2008;**16**(23): 18675-18683

15. Lagonigro L, Healy N, Sparks JR, et al. Low loss silicon fibers for photonics applications. Applied Physics Letters 2010;**96**(4):041105

16. Ballato J, Hawkins T, Foy P, et al. Silica-clad crystalline germanium core optical fibers. Optics Letters 2011;**36**(5):687-688

17. Ballato J, Hawkins T, Foy P, et al. Glass-clad single-crystal germanium optical fiber. Optics Express 2009;**17**(10):8029-8035

18. Paek U, Runk R. Physical behavior of the neck - down region during furnace drawing of silica fibers. Journal of Applied Physics 1978;**49**(8):4417-4422

19. Yin Z, Jaluria Y. Neck down and thermally induced defects in high-speed optical fiber drawing. Journal of Heat Transfer 2000;**122**(2):351-362

20. Chung JD, Lee JS, Yoo H. Thermal instability during the melting process in an isothermally heated horizontal cylinder. International Journal of Heat and Mass Transfer 1997;**40**(16):3899-3907

21. Rieger H, Projahn U, Bareiss M, Beer H. Heat transfer during melting inside a horizontal tube. Journal of Heat Transfer 1983;**105**(2):226-234

22. Nicholas D, Bayazitoglu Y. Heat transfer and melting front within a horizontal cylinder. Journal of Solar Energy Engineering 1980;**102**(3):229-232

23. Bareiss M, Beer H. An analytical solution of the heat transfer process during melting of an unfixed solid phase change material inside a horizontal tube. International Journal of Heat and Mass Transfer 1984;**27**(5):739-746

24. Riviere P, Beer H. Experimental investigation of melting of unfixed ice in an isothermal horizontal cylinder. International Communications in Heat and Mass Transfer 1987;**14**(2):155-165

25. Agyenim F, Hewitt N, Eames P, Smyth M. A review of materials, heat transfer and phase change problem formulation for latent heat thermal energy storage systems (LHTESS). Renewable and Sustainable Energy Reviews 2010;**14**(2):615-628

26. Zalba B, Marın JM, Cabeza LF, Mehling H. Review on thermal energy storage with phase change: materials, heat transfer analysis and applications. Applied Thermal Engineering 2003;**23**(3):251-283

27. Aadmi M, Karkri M, El Hammouti M. Heat transfer characteristics of thermal energy storage for PCM (phase change material) melting in horizontal tube: Numerical and experimental investigations. Energy 2015;**85**:339-352

28. Bechiri M, Mansouri K. Analytical study of heat generation effects on melting and solidification of nano-enhanced PCM inside a horizontal cylindrical enclosure. Applied Thermal Engineering 2016;**104**:779-790

29. Howell PD. Extensional thin layer flows. University of Oxford, 1994.

30. Fluegel A. Glass viscosity calculation based on a global statistical modelling approach. Glass Technology-European Journal of Glass Science and Technology Part A 2007;**48**(1):13-30

31. Ordu M, Guo J, Tai B, et al. Mid-infrared transmission through germanium-core borosilicate glass-clad semiconductor fibers. Optical Materials Express 2017;**7**(9):3107-15

32. Healy N, Gibson U, Peacock AC. A review of materials engineering in silicon-based optical fibres. Semiconductor Science and Technology 2018;**33**(2):023001

33. Biance A-L, Clanet C, Quéré D. Leidenfrost drops. Physics of Fluids 2003;**15**(6):1632-37

34. Churchill SW, Chu HH. Correlating equations for laminar and turbulent free convection from a horizontal cylinder. International Journal of Heat and Mass Transfer 1975;**18**(9): 1049-1053

35. Chow L, Zhong J, Beam J. Thermal conductivity enhancement for phase change storage media. International Communications in Heat and Mass Transfer 1996;**23**(1):91-100

36. Velraj R, Seeniraj R, Hafner B, Faber C, Schwarzer K. Experimental analysis and numerical modelling of inward solidification on a finned vertical tube for a latent heat storage unit. Solar Energy 1997;**60**(5):281-290

37. Pal UB, Powell AC. The use of solid-oxide-membrane technology for electrometallurgy. JOM: Journal of the Minerals, Metals and Materials Society 2007;**59**(5): 44-49

38. Krishnan A, Pal U, Lu X. Solid oxide membrane process for magnesium production directly from magnesium oxide. Metallurgical and Materials Transactions B 2005;**36**(4): 463-473

39. Guan X, Pal UB, Powell AC. An environmentally friendly process involving refining and membrane-based electrolysis for magnesium recovery from partially oxidized scrap alloy. JOM: Journal of the Minerals, Metals and Materials Society 2013;**65**(10):1285-1292

40. Guan X, Zink PA, Pal UB, Powell AC. Recycling of magnesium alloy employing refining and solid oxide membrane (SOM) electrolysis. Metallurgical and Materials Transactions B 2013;**44**(2):261-271

41. Gratz ES, Guan X, Milshtein JD, Pal UB, Powell AC. Mitigating electronic current in molten flux for the magnesium SOM process. Metallurgical and Materials Transactions B 2014;**45**(4):1325-1336

42. Guan X, Pal UB, Powell AC. Energy-efficient and environmentally friendly solid oxide membrane electrolysis process for magnesium oxide reduction: experiment and modeling. Metallurgical and Materials Transactions E 2014;**1**(2):132-144

43. Jiang Y, Xu J, Guan X, Pal UB, Basu SN. Production of silicon by solid oxide membrane-based electrolysis process. MRS Online Proceedings Library Archive 2013; **1493**:231-235

44. Xu J, Lo B, Jiang Y, Pal U, Basu S. Stability of yttria stabilized zirconia in molten oxy-fluorite flux for the production of silicon with the solid oxide membrane process. Journal of the European Ceramic Society 2014;**34**(15):3887-3896

45. Su S, Pal U, Guan X. Solid Oxide Membrane Electrolysis Process for Aluminum Production: Experiment and Modeling. Journal of The Electrochemical Society 2017;**164**(4):F248-F255

46. Krishnan A, Lu XG, Pal UB. Solid Oxide Membrane (SOM) technology for environmentally sound production of tantalum metal and alloys from their oxide sources. Scandinavian Journal of Metallurgy 2005;**34**(5):293-301

47. O'Mara WC, Hunt LP, Herring RB. Handbook of semiconductor silicon technology. 1990

48. Council NR. *Mineral Tolerance of Animals: 2005*: National Academies Press, 2006.

49. Asadikiya M, Sabarou H, Chen M, Zhong Y. Phase diagram for a nano-yttria-stabilized zirconia system. RSC Advances 2016;**6**(21):17438-17445

50. Suito H, Inoue R. Effects of Na2O and BaO additions on phosphorus distribution between CaO-MgO-FetO-SiO2-slags and liquid iron. Transactions of the Iron and Steel Institute of Japan 1984;**24**(1):47-53

51. Duffy J, Ingram M. An interpretation of glass chemistry in terms of the optical basicity concept. Journal of Non-Crystalline Solids 1976;**21**(3):373-410

52. Lux H. "Säuren" und "Basen" im Schmelzfluss: Die Bestimmung der Sauerstoffionen - Konzentration. Zeitschrift für Elektrochemie und Angewandte Physikalische Chemie 1939;**45**(4):303-309

53. Flood H, Förland T. The acidic and basic properties of oxides. Acta Chemica Scandinavica 1947;**1**:592-604

54. Duffy J. Optical basicity: A practical acid-base theory for oxides and oxyanions. Journal of Chemical Education 1996;**73**(12):1138

55. FactSage. Collection of phase diagram. http://www.crct.polymtl.ca/fact/phase_diagram.php?file=CaF2-MgF2.jpg&dir=FTsalt

56. Shahbazian F, Sichen D, Mills K, Seetharaman S. Experimental studies of viscosities of some CaO–CaF2–SiO2 slags. Ironmaking & Steelmaking 1999;**26**(3):193-199

57. Milshtein J, Gratz E, Pati S, Powell AC, Pal U. Yttria stabilized zirconia membrane stability in molten fluoride fluxes for low-carbon magnesium production by the SOM process. Journal of Mining and Metallurgy, Section B: Metallurgy 2013;**49**(2):183-190

58. Lebouteiller A, Courtine P. Improvement of a bulk optical basicity table for oxidic systems. Journal of Solid State Chemistry 1998;**137**(1):94-103

59. Appel C, Bonanos N, Horsewell A, Linderoth S. Ageing behaviour of zirconia stabilised by yttria and manganese oxide. Journal of Materials Science 2001;**36**(18):4493-4501

60. Wang H, Qin R, He G. SiO2 and CaF2 Behavior During Shielded Metal Arc Welding and Their Effect on Slag Detachability of the CaO-CaF2-SiO2 Type ENiCrFe-7-Covered Electrode. Metallurgical and Materials Transactions A 2016;**47**(9):4530-4542

61. Ikuhara Y, Thavorniti P, Sakuma T. Solute segregation at grain boundaries in superplastic SiO2-doped TZP. Acta Materialia 1997;**45**(12):5275-5284

62. Primdahl S, Thölen A, Langdon T. Microstructural examination of a superplastic yttria-stabilized zirconia: implications for the superplasticity mechanism. Acta Metallurgica et Materialia 1995;**43**(3):1211-1218

63. Badwal S, Drennan J. Yttria-zirconia: effect of microstructure on conductivity. Journal of Materials Science 1987;**22**(9):3231-3239

64. Appel CC, Bonanos N. Structural and electrical characterisation of silica-containing yttria-stabilised zirconia. Journal of the European Ceramic Society 1999;**19**(6):847-851

65. De Wet D, Taylor R, Stott F. Corrosion mechanisms of ZrO2-Y2O3 thermal barrier coatings in the presence of molten middle-east sand. Le Journal de Physique IV 1993;**3**(C9):C9-655-C9-63

66. Schmidt H, Seiferling B. Chemistry and applications of inorganic-organic polymers (organically modified silicates). MRS Online Proceedings Library Archive 1986;**73**

67. Karell R, Kraxner J, Chromciková M. Properties of selected zirconia containing silicate glasses. Ceramics - Silikáty 2006;**50**(2):78-82.

68. Moore JJ. *Chemical metallurgy*: Elsevier, 2013.

69. Šesták J, Simon P. *Thermal analysis of micro, nano-and non-crystalline materials: transformation, crystallization, kinetics and thermodynamics*: Springer Science & Business Media, 2012.

70. Van Vlack LH. *Physical ceramics for engineers*. Reading, Massachusetts: Addison Wesley Publishing Company, 1964.

71. Turkdogan ET. *Physicochemical properties of molten slags and glasses*: Metals Society, 1983.

72. Chokshi AH. Diffusion, diffusion creep and grain growth characteristics of nanocrystalline and fine-grained monoclinic, tetragonal and cubic zirconia. Scripta Materialia 2003;**48**(6):791-796

73. Shuai L., Wu W. Status and trend of preparation technology of magnesium fluoride. Materials Review 2011;**25**(363):322-325

74. Hur J-M, Lee S-C, Jeong S-M, Seo C-S. Electrochemical reduction of TiO2 in molten LiCl–Li2O. Chemistry Letters 2007;**36**(8):1028-1029

75. Jeong SM, Jung J-Y, Seo C-S, Park S-W. Characteristics of an electrochemical reduction of Ta2O5 for the preparation of metallic tantalum in a LiCl–Li2O molten salt. Journal of Alloys and Compounds 2007;**440**(1-2):210-215

76. Jeong SM, Yoo HY, Hur J-M, Seo C-S. Preparation of metallic niobium from niobium pentoxide by an indirect electrochemical reduction in a LiCl-Li2O molten salt. Journal of Alloys and Compounds 2008;**452**(1):27-31

77. Park W, Hur J-M, Hong S-S, et al. An experimental study for Li recycling in an electrolytic reduction process for UO2 with a Li2O–LiCl molten salt. Journal of Nuclear Materials 2013;**441**(1-3):232-239

78. Choi E-Y, Won CY, Cha J-S, et al. Electrochemical reduction of UO2 in LiCl–Li2O molten salt using porous and nonporous anode shrouds. Journal of Nuclear Materials 2014;**444**(1-3):261-269

79. Hébant P, Picard GS. Electrochemical investigations of the liquid lithium/(LiCl–KCl eutectic melt) interface. Chronopotentiometric and electrochemical impedance spectroscopy measurements. Electrochimica Acta 1998;**43**(14-15):2071-2081

80. Veličković S, Djustebek J, Veljković F, Radak B, Veljković M. Formation and ionization energies of small chlorine - doped lithium clusters by thermal ionization mass spectrometry. Rapid Communications in Mass Spectrometry 2012;**26**(4):443-448

81. Watanabe N, Nakanishi K, Nakajima T. The dissolution of lithium in molten lithium chloride. Nippon Kagaku Kaishi 1974;**1974**:401-404

82. Nakajima T, Minami R, Nakanishi K, Watanabe N. Miscibility of Lithium with Lithium Chloride and Lithium Chloride–Potassium Chloride Eutectic Mixture. Bulletin of the Chemical Society of Japan 1974;**47**(8):2071-2072

83. Nakajima T, Nakanishi K, Watanabe N. The dispersion of metallic lithium in various molten salts. Nippon Kagaku Kaishi 1975;**1975**(4):617-621

84. Nakajima T, Nakanishi K, Watanabe N. Study of Emulsions in Molten Salts. III. The Concentration, Stability and Particle-Size Distribution of Dispersed Lithium in Molten Lithium Chloride. Bulletin of the Chemical Society of Japan 1976;**49**(4):994-997

85. Xu J, Chen L, Choi H, Konish H, Li X. Assembly of metals and nanoparticles into novel nanocomposite superstructures. Scientific Reports 2013;**3**:1730

86. Merwin A, Phillips WC, Williamson MA, Willit JL, Motsegood PN, Chidambaram D. Presence of Li clusters in molten LiCl-Li. Scientific Reports 2016;**6**:25435

87. Benmore C. A review of high-energy X-ray diffraction from glasses and liquids. ISRN Materials Science 2012;**2012**

88. Liu J, Poignet J-C. Measurement of the activity of lithium in dilute solutions in molten lithium chloride between 650 C and 800 C. Journal of Applied Electrochemistry 1990;**20**(5):864-867

89. Liu J, Poignet J-C. Electronic conductivity of salt-rich Li− LiCl melts. Journal of applied electrochemistry 1992;**22**(11):1110-1112

90. Howe M, McGreevy R. A neutron-scattering study of the structure of molten lithium chloride. Philosophical Magazine B 1988;**58**(5):485-495

91. McGreevy R, Howe M. The structure of molten LiCl. Journal of Physics: Condensed Matter 1989;**1**(49):9957

CURRICULUM VITAE